VILNIUS UNIVERSITY

Julius Darginavičius

THREE AND FOUR WAVE PARAMETRIC INTERACTIONS FOR ULTRASHORT PULSE GENERATION IN THE ULTRAVIOLET, NEAR AND MID-INFRARED SPECTRAL RANGE

Doctoral dissertation

Physical sciences, physics (02P)

Vilnius, 2013

The researched was performed in 2009-2013 at Vilnius University

Scientific supervisor:

prof. habil. dr. Audrius Dubietis (Vilnius university, physical sciences, physics - 02P)

Scientific advisor:

dr. Gintaras Tamošauskas (Vilnius university, physical sciences, physics - 02P)

VILNIAUS UNIVERSITETAS

Julius Darginavičius

TRIJŲ IR KETURIŲ BANGŲ PARAMETRINIŲ SĄVEIKŲ TAIKYMAS ULTRATRUMPŲJŲ IMPULSŲ GENERACIJAI ULTRAVIOLETINIAME, ARTIMAJAME IR VIDURINIAJAME INFRARAUDONAJAME SPEKTRO RUOŽE

Daktaro disertacija

Fiziniai mokslai, fizika (02P)

Vilnius, 2013

Disertacija rengta 2009–2013 metais Vilniaus Universitete

Mokslinis vadovas:

prof. habil. dr. Audrius Dubietis (Vilniaus universitetas, fiziniai mokslai, fizika - 02P)

Konsultantas:

dr. Gintaras Tamošauskas (Vilniaus universitetas, fiziniai mokslai, fizika - 02P)

Acknowledgements

This doctoral dissertation would not have been possible without the support of many people.

First and foremost I would like to express sincere gratitude to my supervisor, Professor A. Dubietis, for his guidance, useful critiques and overall support during the planning and development of this research work.

I would like to thank my advisor, Dr. G. Tamošauskas, without whose knowledge, assistance and useful discussions this study would not have been successful.

I am grateful to Professor G. Valiulis, who provided a theoretical background for many nonlinear optics phenomena described in this thesis.

Special thanks to L. Mikalauskienė and Dr. D. Kaškelytė for handling all the paperwork.

I would like also to thank the present head of the Quantum Electronics Department, Professor Valdas Sirutkaitis, as well as the former, Professor Algis Petras Piskarskas, for providing the necessary environment to do the research.

Julius Darginavičius
Vilnius 2013

Contents

List of the abbreviations

TWM	three-wave mixing
FWM	four-wave mixing
SH	second harmonic
TH	third harmonic
SHG	second harmonic generation
SFG	sum frequency generation
DFG	difference frequency generation
OPA	optical parametric amplification
FWOPA	four-wave optical parametric amplification
NOPA	noncollinear optical parametric amplifier
OPCPA	optical parametric chirped pulse amplification
SPM	self phase modulation
XPM	cross phase modulation
GVM	group velocity mismatch
GVD	group velocity dispersion
IR	infrared
NIR	near infrared
MIR	mid-infrared
UV	ultraviolet
DUV	deep ultraviolet
VUV	vacuum ultraviolet
CEP	carrier-envelope phase
HHG	high-harmonic generation
SC	supercontinuum
FWHM	full width at half maximum
FTSI	Fourier transform spectral interferometry
rms	root-mean-square
FROG	frequency-resolved optic gating
BBO	β-barium borate (β-BaB_2O_4)

Introduction

Many processes in chemistry and biology proceed on an ultrafast time scale (sometimes with a decay time of just a few tens of femtoseconds). The direct investigation of such rapid processes rely on the pump-probe time-resolved spectroscopy [1, 2], where the achieved temporal resolution is limited by the length of the light pulse. In addition, many pump-probe experiments require optical pulses with short duration as well as broad frequency tunability [3]. Optical parametric amplifiers based on three-wave interaction in $\chi^{(2)}$ crystals nowadays is a well established technique, used for producing powerful ultrashort light pulses tunable across visible and infrared (IR) spectral range [4–6]. Their efficiency, however, drops significantly in the ultraviolet (UV) due to high group velocity mismatch (GVM) and increased linear and nonlinear absorption of the pump wave [7, 8]. Extending the spectral range of the parametric amplification into the UV, on the other hand, is crucial for studying ultrafast chemical processes, where many molecules have characteristic absorption bands [9]. A standard route to expand the tuning range of the ultrashort light pulses to UV relies on frequency up-conversion (second-harmonic and/or sum-frequency generation (SHG, SFG)), which becomes technically complicated approaching pulse lengths of 10 fs [10]. An alternative way is proposed by the use of four-wave mixing (FWM), which allows direct amplification of the ultrashort UV light pulses in transparent isotropic media with cubic nonlinearity. Noble gases and air, having high transparency and low dispersion in the ultraviolet, might readily serve as the amplifying media [11]. Small intrinsic third-order nonlinearity of the gaseous media is compensated by providing sufficiently long interaction length by means of self-guided propagation of the pump beam in the gas-filled capillary waveguides [12] or in the filamentation regime [13]. Applying these techniques, tunable 30 fs pulses across the deep ultraviolet (DUV) (200-300 nm) spectral range were demonstrated [14], while the shortest pulses in the DUV and even vacuum ultraviolet (VUV) with dura-

tion of $\sim$ 10 fs were generated via 3-rd, 4-th and 5-th harmonic generation of the Ti:sapphire laser [15–17].

As compared to gases, condensed bulk media exhibit much higher third-order nonlinearity. Nevertheless, due to high material dispersion, non-degenerate four-wave parametric interactions in condensed media could be phase-matched only noncollinearly. Moreover, high intensity of the applied laser field gives rise to a number of competing nonlinear effects: self- and cross-phase modulation (SPM, XPM), self-focusing, beam break-up and filamentation, and eventually optical breakdown, which occur almost at the same intensity threshold [18]. So far, typical achieved pulse energy via four-wave optical parametric amplification (FWOPA) in bulk solids were $\sim$ 1 µJ in the visible spectral range [19] and few hundreds of nJ in the IR [20] spectral range. In the second Chapter of this thesis we demonstrate that frequency conversion setups based on FWM in bulk solid-state media can safely and efficiently operates under millijoule pumping and has broad amplification bandwidth in the ultraviolet spectral range. The latter is achieved employing cylindrical focusing geometry, which allows to fulfill the noncollinear phase matching condition without reducing the interaction length.

Generation of tunable, few-cycle light pulses in the near infrared (NIR, 0.8-2 µm) and mid-infrared (MIR, 2-20 µm) spectral range are required for diverse studies. Recent advances in time-resolved MIR spectroscopy enabled to probe molecular structure and dynamics on the femtosecond time scale [21]. The generation of intense few-cycle IR pulses is also motivated by strong field physics, in particular, long wavelength-driven high-harmonic generation (HHG) [22], attosecond pulse generation [23] and above-threshold ionization [24]. The latter applications also require the control of the pulse carrier-envelope phase (CEP). In nonlinear optics few-cycle IR pulse sources serve to study femtosecond pulse propagation and supercontinuum (SC) generation in the anomalous group velocity dispersion (GVD) regime, which is poorly explored up to date [25]. In view of the above mentioned applications, the generation of tunable few-optical cycle IR pulses is one of the major challenges of ultrafast optics. In the pursuit of this goal, various strategies have been proposed. In particular, difference frequency generation (DFG) and optical parametric amplification (OPA) processes have been largely employed to down-convert visible or NIR light sources using $\chi^{(2)}$ materials [26, 27]. Recent advances in generation of few-

cycle IR pulses now challenge extreme pulse durations of 10.5 fs (1.5 optical cycles at 2.1 µm) with energy up to 1.2 mJ [28]. The existing alternatives for ultrashort pulse generation in the IR spectral range suggest optical parametric amplification in gases by means of four-wave parametric processes in the filamentation [29] and guided-wave propagation regimes [30]. The latter guarantees broad amplification bandwidth, that is able of supporting IR pulses close to a single optical cycle [31]. Another approach considers MIR pulse generation in wide bandgap solids, such as CaF_2 and BaF_2 [20, 32], which possess much higher third-order nonlinearity than gases.

A considerable progress in widely tunable femtosecond pulse generation is closely related to the development of commercial amplified femtosecond Ti:sapphire laser systems, which nowadays provide stable and high energy pulses with 30-150 fs duration at 800 nm. Moreover, Ti:sapphire laser pumped noncollinear optical parametric amplifiers (NOPAs) serve as indispensable tool for generation of ultrashort visible pulses with duration < 30 fs [33]. In the third Chapter of the thesis we experimentally demonstrate two methods, that extends the tuning range of a commercial Ti:sapphire laser-NOPA system in the $1.1 - 2.8$ µm wavelength range maintaining sub 30 fs pulse duration. The first approach relies on four-wave optical parametric amplification in fused silica sample, while the second is based on difference frequency generation and subsequent optical parametric amplification in type I β-barium borate (BBO) crystals.

This work aims at practical investigation and development of three- and four-wave interaction-based frequency conversion methods for sub-30 fs pulse generation in the ultraviolet and near-to-mid infrared spectral range for various applications in laser material processing, ultrafast spectroscopy and nonlinear optics, and for studies in the emerging field of mid-infrared nonlinear optics in particular.

The thesis is organized as follows:

- In **Chapter 1** a general introduction to nonlinear polarization, three and four-wave optical parametric amplification is made. The principles of NOPA, passive CEP stabilization method and CEP jitter measurement are explained.
- In **Chapter 2** we demonstrate: (i) generation of 1-ps pulses at the

3rd, 5th, and 6th harmonics of the Nd:glass laser through four-wave difference-frequency mixing in fused silica, CaF_2 and MgF_2 crystals; (ii) broadband FWOPA around 330 nm in fused silica and CaF_2; (iii) generation of ∼30 fs UV pulses by means of four-wave optical parametric chirped pulse amplification (OPCPA) in fused silica.

- In **Chapter 3** we present two methods for ultrashort pulse parametric visible-to-infrared frequency conversion. The first method is based on broadband noncollinear four-wave optical parametric amplification in fused silica, and the second is based on three-wave difference frequency generation and subsequent optical parametric amplification in type I BBO crystals.

- In **Chapter 4** we demonstrate the generation of ultrabroadband SC in fused silica, sapphire, CaF_2 and yttrium aluminum garnet (YAG), using 20 fs, CEP-stable pulses at 2 µm. Prior to spectral superbroadening, we observe third harmonic (TH) generation, which occurs in the condition of large phase and GVM and consists of *free* and *driven* components.

The main tasks of the thesis

1. To demonstrate efficient frequency conversion from near infrared and visible to UV spectral range employing phase-matched FWM in bulk wide-bandgap isotropic media.

2. To adapt the concept of OPCPA to broadband four-wave optical parametric amplifiers operating in the ultraviolet spectral range.

3. To elaborate visible-to-infrared frequency conversion methods for generation of widely tunable, sub 30 fs pulses in the NIR and MIR spectral ranges.

4. To investigate ultrabroadband supercontinuum generation in the anomalous group velocity dispersion regime in wide bandgap solid state media using few optical cycle stable CEP pulses.

Practical novelty

1. Efficient generation of third, fifth and sixth harmonics of the Nd:glass laser using phase-matched noncollinear four-wave frequency mixing in wide-bandgap solid-state isotropic media with cubic nonlinearity is demonstrated.

2. Broadband four-wave optical parametric chirped pulse amplifier based on fused silica is demonstrated. The amplifier delivers 10 µJ, 30-fs pulses at 310 nm.

3. Noncollinear four-wave optical parametric amplifier based on fused silica, which provides sub-30 fs pulses tunable in the near infrared ($1.1 - 1.5$ µm) spectral range is demonstrated.

4. Collinear BBO-crystal based visible-to-infrared frequency converter, which employs broadband difference frequency generation and subsequent optical parametric amplification and provides $1.2 - 2.4$ µm tunable sub-30 fs pulses, is demonstrated. It is shown, that the proposed technique could be easily adopted for generation of few-optical cycle pulses in the $3 - 5.5$ µm spectral range.

5. Noncollinear 800 nm pumped BBO crystal based optical parametric amplifier, which provides 15 µJ, $1.6 - 2.8$ µm central wavelength two optical cycle pulses with stable CEP, is demonstrated.

6. Filamentation of few optical cycle CEP stable pulses at 2 µm in wide-bandgap solid state media in the regime of anomalous group velocity dispersion yields ultrabradband CEP stable supercontinuum spanning from 450 nm to more than 2.5 µm.

Scientific novelty

1. Four wave interactions in bulk transparent solids could be made efficient by fulfilling noncollinear phase matching condition and using cylindrical beam focusing geometry.

2. Parametric gain bandwidth broadening in FWOPA is resulted by self- and cross-phase modulation effects imposed by the intense pump wave.

3. Optical parametric chirped pulse amplification concept is adopted to four wave optical parametric amplifier, which operates in the ultraviolet and which is capable to amplify pulses as short as 30 fs.

4. The group velocities of the signal and idler pulses could be matched in 800 nm-pumped noncollinear type I BBO crystal-based optical parametric amplifier seeded in the $1.6-2.8$ µm spectral range. In this configuration BBO OPA provides broad amplification bandwidth, which supports broadly tunable two optical cycle pulses.

5. Intrinsic third harmonic generation, which accompanies supercontinuum generation in transparent dielectric media, can be used for f-3f interferometric measurements of the CEP.

Statements of defend

1. Combination of cylindrical focusing and noncollinear interaction geometry allows to achieve efficient four-wave optical parametric amplification of ultrashort pulses in bulk, transparent solids.

2. Efficient difference frequency generation and optical parametric amplification processes can occur at the same time in a single type I BBO crystal if simultaneously pumped at 800 nm and visible (570–630 nm) spectral range.

3. Group velocity matching between signal and idler waves can be achieved in a 800 nm pumped type I BBO crystal-based NOPA if seeded in the 1.6–2.8 µm wavelength range.

4. Simultaneous third harmonic and supercontinuum generation in transparent dielectric media can be readily used for f-3f interferometric measurements of the carrier-envelope phase fluctuations.

Approbation

Scientific papers related to the topic of this thesis

[**A1**] A. Dubietis, H. Valtna, G. Tamošauskas, **J. Darginavičius**, and A. Piskarskas, Efficient ultrafast four-wave optical parametric amplification in condensed bulk media, Springer Series in Chemical Physics,

Ultrafast phenomena, **16**, 792–794, proceedings of the 16$^{\text{th}}$ international conference, Italy (2009).

[**A2**] **J. Darginavičius**, G. Tamošauskas, G. Valiulis, and A. Dubietis, Broadband optical parametric amplification in bulk isotropic media in the ultraviolet, Opt. Commun., **282**, 2995–2999 (2009).

[**A3**] **J. Darginavičius**, D. Majus, G. Tamošauskas, and A. Dubietis, Highly efficient third harmonic generation by means of four-wave difference-frequency mixing in fused silica, Lithuanian J. Phys. **49**, 171–174 (2009).

[**A4**] A. Dubietis, **J. Darginavičius**, G. Tamošauskas, G. Valiulis, and A. Piskarskas, Generation and amplification of ultrashort UV pulses via parametric four-wave interactions in transparent solid-state media, Lithuanian J. Phys. **49**, 421–431 (2009).

[**A5**] **J. Darginavičius**, G. Tamošauskas, G. Valiulis, and A. Dubietis, Generation and amplification of ultraviolet light pulses by means of parametric four-wave interactions in transparent solid-state media, AIP Conf. Proc, **1228**, 351–358 (2010).

[**A6**] **J. Darginavičius**, G. Tamošauskas, A. Piskarskas, and A. Dubietis, Generation of 30-fs ultraviolet pulses by four-wave optical parametric chirped pulse amplification, Opt. Express, **18**, 16096–16101 (2010).

[**A7**] E. Rubino, **J. Darginavičius**, D. Faccio, P. Di Trapani, A. Piskarskas, and A. Dubietis, Generation of broadly tunable sub-30-fs infrared pulses by four-wave optical parametric amplification, Opt. Lett, **36**, 382–384 (2011).

[**A8**] **J. Darginavičius**, G. Tamošauskas, G. Valiulis, A. Piskarskas, and A. Dubietis, Generation of sub-30 fs tunable infrared pulses by parametric visible-to-infrared frequency conversion, AIP Conf. Proc, **1462**, 92–95 (2012).

[**A9**] **J. Darginavičius**, E. Rubino, G. Tamošauskas, D. Faccio, G. Valiulis, P. Di Trapani, A. Piskarskas, and A. Dubietis, Generation of tunable infrared femtosecond pulses via parametric visible-to-infrared frequency conversion, Lithuanian J. Phys. **51**, 221–229 (2011).

[**A10**] **J. Darginavičius**, G. Tamošauskas, A. Piskarskas, G. Valiulis, and A. Dubietis, Generation of tunable few optical-cycle pulses by visible-to-infrared frequency conversion, Appl. Phys. B. **108**, 1–7 (2012).

[**A11**] **J. Darginavičius**, N. Garejev, and A. Dubietis, Generation of carrier-envelope phase-stable two optical-cycle pulses at 2 µm from a noncollinear BBO optical parametric amplifier, Opt. Lett, **37**, 4805–4807 (2012).

[**A12**] **J. Darginavičius**, D. Majus, V. Jukna, N. Garejev, G. Valiulis, A. Couairon, and A. Dubietis, Ultrabroadband supercontinuum and third-harmonic generation in bulk solids with two optical-cycle carrier envelope phase-stable pulses at 2 µm, Opt. Express, submitted (2013).

Other scientific papers

[**A13**] D. Faccio, G. Tamošauskas, E. Rubino, **J. Darginavičius**, D. G. Papazoglou, S. Tzortzakis, A. Couairon, and A. Dubietis, Cavitation dynamics and directional microbubble ejection induced by intense femtosecond laser pulses in liquids, Phys. Rev. E. **86**, 036304 (2012).

Conference presentations

Presented by Julius Darginavičius:

[**C1**] **J. Darginavičius**, A. Dubietis, G.Tamošauskas, and G. Valiulis, Generation and amplification of ultraviolet light pulses by means of parametric four-wave interactions in transparent solid-state media, Int. Conf. Light at Extreme Intensities, Brasov, Romania, (2009).

[**C2**] **J. Darginavičius**, G. Tamošauskas, A. Piskarskas, and A. Dubietis, Generation of 30-fs ultraviolet pulses by four-wave optical parametric chirped pulse amplification, Alexander von Humboldt Forum, Vilnius, Lithuania, (2010).

[**C3**] **J. Darginavičius**, G. Tamošauskas, A. Piskarskas, and A. Dubietis, Generation of 30-fs ultraviolet pulses by four-wave optical parametric chirped pulse amplification, 66 International summer school in ultrafast nonlinear optics SUSSP 66, Edinburgh, United Kingdom, (2010).

[**C4**] **J. Darginavičius**, E. Rubino, D. Faccio, P. Di Trapani, A. Piskarskas, and A. Dubietis, Generation of broadly tunable sub-30-fs infrared pulses by four-wave optical parametric amplification, EOS Annual Meeting 2010, Paris, France, (2010).

[**C5**] **J. Darginavičius**, E. Rubino, G. Tamošauskas, D. Faccio, G. Valiulis, P. Di Trapani, A. Piskarskas, and A. Dubietis, Generation of tunable infrared femtosecond pulses via parametric visible-to-infrared frequency conversion, 39$^{\text{th}}$ Lithuanian national physics conference, Vilnius, Lithuania, (2011).

[**C6**] **J. Darginavičius**, G. Tamošauskas, G. Valiulis, A. Piskarskas, and A. Dubietis, Generation of sub-30 fs tunable infrared pulses by parametric visible-to-infrared frequency conversion, Int. Conf. Light at Extreme Intensities, Szeged, Hungary, (2011).

[**C7**] **J. Darginavičius**, G. Tamošauskas, G. Valiulis, A. Piskarskas and A. Dubietis, Generation of tunable infrared femtosecond pulses via parametric visible-to-infrared frequency conversion, Advanced Solid-State Photonics (ASSP) Topical meeting, San Diego, United States, (2012).

[**C8**] **J. Darginavičius**, D. Majus, V. Jukna, N. Garejev, T. Vasiliauskas, and A. Dubietis, Ultrabroadband supercontinuum generation in bulk solids with few-optical-cycle CEP-stable pulses at 2 μm, Int. Conf. Northern optics, Snekkersten, Denmark, (2012).

Co-author of the presentation:

[**C9**] A. Dubietis, **J. Darginavičius**, G. Tamošauskas, G. Valiulis, and A. Piskarskas, Generation and amplification of ultraviolet light pulses by means of parametric four-wave interactions in transparent solid-state media, 38$^{\text{th}}$ Lithuanian national physics conference, Vilnius, Lithuania (2009).

[**C10**] A. Dubietis, **J. Darginavičius**, G. Tamošauskas, G. Valiulis, and A. Piskarskas, Phase-matched frequency conversion through parametric four-wave interactions in transparent isotropic solid-state media, Int. Conf. Northern optics, Vilnius, Lithuania, (2009).

[**C11**] A. Dubietis, **J. Darginavičius**, D. Majus, N. Garejev, V. Jukna, and G. Valiulis, Supercontinuum generation in wide bandgap dielectrics with two optical-cycle infrared pulses, 40^{th} Lithuanian national physics conference, Vilnius, Lithuania (2013).

Co-authors contribution

All the experiments described in this thesis were performed in Vilnius University, Department of Quantum Electronics during the period 2009–2013 by the author himself, however it is important to specify the significant contribution of these co-authors:

- prof. habil. dr. **A. Dubietis**[1] formulated the general tasks. He initiated the four-wave mixing experiments, the development of a few optical cycle, CEP-stable IR source and supercontinuum generation in the anomalous GVD regime. He helped to interpret the results and present them to scientific community;
- dr. **G. Tamošauskas**[1] together performed the broadband four-wave optical parametric amplification experiment; assisted during some experiments of UV harmonics generation. He should be credited for invaluable advices, ideas and discussions related to experimental laser physics;
- prof. habil. dr. **G. Valiulis**[1] formulated a theoretical description of the four-wave optical parametric amplification with intense pump beams, explained the temporal evolution of the generated TH pulse, provided a theoretical basis for many nonlinear optics phenomena;
- Ph.D. student **D. Majus**[1] performed supercontinuum generation in the anomalous GVD regime measurements;
- dr. **D. Faccio**[2] initiated the four-wave mixing experiment, helped to interpret and publish the results;
- dr. **E. Rubino**[2] together performed the four-wave optical parametric amplification in the IR spectral range experiment, processed the SHG-FROG (second harmonic generation frequency-resolved optic gating) data;

- student **N. Garejev**[1] helped to process the THG-FROG (third harmonic generation frequency-resolved optic gating) data.

[1]Department of Quantum Electronics, Vilnius University, Saulėtekio Avenue 9, Building 3, LT-10222 Vilnius, Lithuania.

[2]School of Engineering and Physical Sciences, SUPA, Heriot-Watt University, Edinburgh EH14 4AS, Scotland, United Kingdom.

Chapter 1

General introduction

1.1 Nonlinear polarization

At low light intensities, typical of non-laser sources, material properties (i.e. absorption coefficient, index of refraction) remain independent on the strength of the applied optical field. The polarization $P(t)$ induced in an atom or a molecule by an external field in this case depends linearly on the electric field strength $E(t)$:

$$P(t) = \epsilon_0 \chi^{(1)} E(t), \tag{1.1}$$

where $\chi^{(1)}$ is known as the linear susceptibility and ϵ_0 is the permittivity of free space. Laser sources, on the other hand, can provide sufficiently high light intensities to modify the optical properties of material. In the regime of weak fields the polarization $P(t)$ as a function of $E(t)$ can be expanded into a Taylor series of E [34]:

$$\begin{aligned} P(t) &= \epsilon_0[\chi^{(1)}E(t) + \chi^{(2)}E^2(t) + \chi^{(3)}E^3(t) + \cdots] \\ &= P^{(1)}(t) + P^{(2)}(t) + P^{(3)}(t) + \cdots = P^{(1)}(t) + P^{\mathrm{NL}}(t). \end{aligned} \tag{1.2}$$

Here, the quantities $\chi^{(2)}$ and $\chi^{(3)}$ are known as the second- and third-order nonlinear optical susceptibilities, respectively, while $P^{(2)}(t)$ and $P^{(3)}(t)$ – second- and third-order nonlinear polarization. The second-order polarization gives rise to three-wave mixing (TWM) processes such as SHG, SFG, DFG, OPA. Second-order interactions can occur only in noncentrosymmetric crystals (crystals that do not display inversion symmetry). Since liquids, gases, amorphous solids (such as glass), and even many crystals display inversion symmetry, $\chi^{(2)}$ vanishes for such media, and consequently such materials cannot produce second-order interactions. The third-order

nonlinear polarization is responsible for FWM, Kerr-effect related phenomena (self and cross phase modulation (SPM), (XPM), self-focusing), optical phase conjugation. Third-order interactions (i.e., those described by a $\chi^{(3)}$ susceptibility) can occur for both centrosymmetric and noncentrosymmetric media.

1.2 Three wave optical parametric amplification

Optical parametric amplification is a phenomenon where a weak input wave (referred to as the signal), is amplified in the process of a nonlinear interaction with a powerful pump wave. In addition a third wave (the idler) is generated. The OPA can be realized via three-wave, four-wave or in general via n-wave mixing processes. In the present section we consider parametric amplification based on a $\chi^{(2)}$ nonlinearity, that is TWM, while four-wave mixing is discussed in the following section.

Nonlinear optical effects are usually described within the general framework of Maxwell equations. For the nonlinear media, that contains no free charges, no free currents and is nonmagnetic, the wave equation governing the propagation of light can be expressed as [34]:

$$\nabla^2 E - \frac{n^2}{c^2}\frac{\partial^2 E}{\partial t^2} = \frac{1}{\epsilon_0 c^2}\frac{\partial^2 P^{\mathrm{NL}}}{\partial t^2}, \tag{1.3}$$

where n is material refraction index and c is the speed of light in vacuum. In particular, for the three-wave interaction the wave Eq. 1.3 must hold for each frequency component of the field. Within the slowly varying amplitude approximation, involving monochromatic, plane waves we can derive the following coupled amplitude equations for the three waves propagating along z direction [34]:

$$\frac{\partial A_s}{\partial z} = -i\sigma_s A_p A_i^* e^{-i\Delta k z}, \tag{1.4a}$$

$$\frac{\partial A_i}{\partial z} = -i\sigma_i A_p A_s^* e^{-i\Delta k z}, \tag{1.4b}$$

$$\frac{\partial A_p}{\partial z} = -i\sigma_p A_s A_i e^{i\Delta k z}, \tag{1.4c}$$

where A_j $(j = s, i, p)$ are the complex amplitudes of the signal, idler and pump waves, respectively, $\Delta k = \mathbf{\Delta k l_z}$ is the longitudinal phase mismatch, $\mathbf{l_z}$ is the unit vector along z axis, $\mathbf{\Delta k} = \mathbf{k_p} - \mathbf{k_s} - \mathbf{k_i}$, $|\mathbf{k}| = n(\omega)\omega/c$ is the

wave number, $n(\omega)$ is refractive index, $\sigma_j = \frac{\omega_j}{2n(\omega_j)c}\chi^{(2)}_{\text{eff}}$ is the wave coupling coefficient, where $\chi^{(2)}_{\text{eff}}$ is the second-order susceptibility. If we neglect pump depletion (A_p =const.) the solution to Eqs. 1.4 is readily found to be:

$$A_s(z) = \left[A_s(0)\left(\cosh gz - \frac{i\Delta k}{2g}\sinh gz\right) + \frac{\alpha_s}{g}A_i^*(0)\sinh gz\right]e^{i\Delta kz/2}, \tag{1.5a}$$

$$A_i(z) = \left[A_i(0)\left(\cosh gz - \frac{i\Delta k}{2g}\sinh gz\right) + \frac{\alpha_i}{g}A_s^*(0)\sinh gz\right]e^{i\Delta kz/2}, \tag{1.5b}$$

where the coefficient g is given by

$$g = \left[\Gamma^2 - \left(\frac{\Delta k}{2}\right)^2\right]^{1/2}, \tag{1.6}$$

with $\Gamma = (\alpha_s\alpha_i^*)^{1/2}$ and $\alpha_j = \sigma_j A_p$. For the case of perfect phase matching ($\Delta k = 0$, $g = \Gamma$) and in the large gain approximation Eqs. 1.5 simplify to

$$I_s(z) \cong \frac{1}{4}I_{s0}\exp(2\Gamma z), \tag{1.7a}$$

$$I_i(z) \cong \frac{\omega_i n_s}{4\omega_s n_i}I_{s0}\exp(2\Gamma z). \tag{1.7b}$$

Here pump, signal, and idler intensities I_j ($j = p, s, i$) are related to the field strengths A_j by

$$I_j = \frac{n_j\epsilon_0 c_0}{2}\left|A_j\right|^2. \tag{1.8}$$

The gain of an OPA in this case can be expressed as:

$$G = \frac{I_s(z)}{I_{s0}} = \frac{1}{4}\exp(2\Gamma z). \tag{1.9}$$

It is clear from Eqs. 1.5 that the perfect phase matching ($\Delta k = 0$) is the key requirement for efficient energy transfer between pump and signal/idler beams. The condition $\Delta k = 0$, however is often difficult to achieve, because in the transparency range materials have a positive dispersion: the refractive index is an increasing function of frequency. As a result, the condition for perfect phase matching with collinear beams,

$$\frac{n_s\omega_s}{c} + \frac{n_i\omega_i}{c} = \frac{n_p\omega_p}{c}, \tag{1.10}$$

cannot be satisfied. Typically, three-wave mixing is done in a birefringent crystalline material, where refraction index $n(\omega)$ depends on the polarization and propagation direction of light [35]. For the case of an uniaxial

crystal (e.g. BBO) there are two choices for the polarizations of the lower-frequency waves. If the polarizations of the signal and idler waves are the same, the wave mixing is said to be type I, if they are orthogonal, it is said to be type II. Light polarized perpendicular to the plane containing the propagation vector **k** and the optic axis is called the ordinary polarization (light experiences a refractive index n_o). Light polarized in the plane containing **k** and the optic axis is called the extraordinary polarization and experiences a refractive index $n_e(\theta)$ that depends on the angle θ between the optic axis and **k** according to the relation:

$$\frac{1}{n_e(\theta)^2} = \frac{\sin^2\theta}{n_e^2} + \frac{\cos^2\theta}{n_o^2}. \tag{1.11}$$

Phase matching is achieved by precisely adjusting the angle θ to obtain the $n_e(\theta)$, for which the condition $\Delta k = 0$ is satisfied. The latter method is called *angle tuning*. The other method suggests *temperature tuning*. In this case it is possible to phase-match the wave mixing process by holding θ fixed at 90° and varying the temperature of the crystal [36]. Other technique, that enables efficient three-wave mixing suggests quasi-phase matching in periodically-poled nonlinear crystals [37].

The signal and idler frequencies in principle can vary broadly in ranges $\omega_p > \omega_s \geq \omega_p/2$ and $0 < \omega_i \leq \omega_p/2$, where the lowest achievable frequency is limited by the absorption of the nonlinear crystal. The OPA process thus provides an easy way of tuning signal/idler over a broad spectral range, which is very hard to access directly with lasers due to the lack of suitable gain media.

1.3 Four wave optical parametric amplification

In the four-wave mixing interaction, the cubic nonlinearity couples together four frequency components ω_{p1}, ω_{p2}, ω_s and ω_i (here indexes p, s, i stand for pump, signal, and idler waves) through the induced nonlinear polarization. For simplicity, lets assume that the two pump waves are identical ($\omega_{p1} = \omega_{p2} = \omega_p$), then the evolution of the complex amplitude A_j ($j = s, i, p$) is

governed by a set of three coupled equations that can be written as [18]

$$\frac{\partial A_s}{\partial z} = -i\sigma_s A_p^2 A_i^* e^{-i\Delta k z}, \tag{1.12a}$$

$$\frac{\partial A_i}{\partial z} = -i\sigma_i A_p^2 A_s^* e^{-i\Delta k z}, \tag{1.12b}$$

$$\frac{\partial A_p}{\partial z} = -i2\sigma_p A_s A_i A_p^* e^{i\Delta k z}. \tag{1.12c}$$

$\Delta k = \mathbf{\Delta k l_z}$ is the longitudinal phase mismatch, $\mathbf{\Delta k} = 2\mathbf{k_p} - \mathbf{k_s} - \mathbf{k_i}$, and σ_j are the wave coupling coefficients, expressed as:

$$\sigma_j = \frac{3}{8}\frac{\omega_j}{n_0(\omega_j)c}\chi^{(3)}_{\text{eff}}, \tag{1.13}$$

where $\chi^{(3)}_{\text{eff}}$ is the third-order susceptibility related to the nonlinear refractive index n_2

$$n_2 = \frac{3\chi^{(3)}_{\text{eff}}}{4n_0^2 c\epsilon_0}. \tag{1.14}$$

The solution to the Eqs. 1.12, neglecting pump depletion (A_p =const.) and assuming no idler wave at the input ($A_i(0) = 0$):

$$A_s(z) = A_s(0)\left(\cosh gz - \frac{i\Delta k}{2g}\sinh gz\right)e^{i\Delta k z/2}, \tag{1.15a}$$

$$A_i(z) = A_s^*(0)\left(\frac{\alpha_i}{g}\sinh gz\right)e^{i\Delta k z/2}, \tag{1.15b}$$

with $\alpha_j = \sigma_j A_p^2$ and g:

$$g = \left[\Gamma^2 - \left(\frac{\Delta k}{2}\right)^2\right]^{1/2}, \tag{1.16}$$

where $\Gamma = (\alpha_s \alpha_i^*)^{1/2}$. In the case of phase-matched interaction the signal and idler intensities reduce to

$$I_s(z) \cong \frac{1}{4} I_{s0}\exp(2\Gamma z), \tag{1.17a}$$

$$I_i(z) \cong \frac{\omega_i n_s}{4\omega_s n_i} I_{s0}\exp(2\Gamma z), \tag{1.17b}$$

and the gain:

$$G = \frac{I_s(z)}{I_{s0}} = \frac{1}{4}\exp(2\Gamma z). \tag{1.18}$$

The expressions of the gain in the case of three- and four-wave OPAs are virtually the same (Eqs. 1.18 and 1.9), however in the three-wave mixing $G_{TWM} \sim \exp(\sqrt{I_p}z)$ and in the four-wave mixing $G_{FWM} \sim \exp(I_p z)$.

The efficiency of the FWM crucially depends on the phase mismatch Δk of the interacting waves. Assuming positive material dispersion, in collinear configuration $k_p + k_p$ is always smaller than $k_s + k_i$, therefore the condition of perfect phase matching $\Delta k = 0$ in isotropic materials is achievable in noncollinear geometry only. The wave-vector matching diagram for the four-wave parametric amplification is depicted in Fig. 1.1. It considers a pump beam, represented by the sum of two collinear wave-vectors $\mathbf{k}_p$, signal ($\mathbf{k}_s$), and idler ($\mathbf{k}_i$) beams propagating at some angles θ and ϕ with respect to the pump beam propagation axis. After simple algebra, one finds the phase matching angles θ and ϕ between the pump and signal/idler beams:

$$\theta = \arccos \frac{4k_p^2 + k_s^2 - k_i^2}{4k_s k_p}, \tag{1.19}$$

$$\phi = \arccos \frac{4k_p^2 + k_i^2 - k_s^2}{4k_i k_p}. \tag{1.20}$$

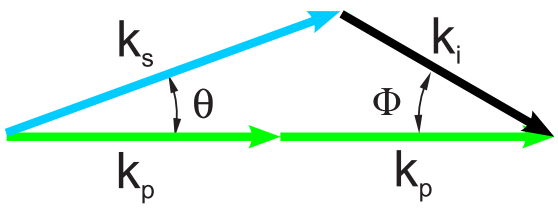

Figure 1.1: Wave-vector diagram describing the noncollinear four-wave parametric amplification.

The signal and idler frequencies in principle can be tuned in ranges $2\omega_p > \omega_s \geq \omega_p$ and $0 < \omega_i \leq \omega_p$. The four-wave parametric interaction, therefore enables to amplify and/or generate pulses with wavelength shorter that the pump. The latter is not possible with conventional three-wave OPAs, where wavelengths of both signal and idler waves are longer than the pump. The lowest achievable frequency in four-wave OPAs is limited by the absorption of the nonlinear medium.

1.4 Noncollinear optical parametric amplification

So far we have studied the parametric interaction of monochromatic waves. In the case of short pulses propagating in the nonlinear crystal with different group velocities $v_g = d\omega/dk$ and neglecting pulse lengthening due to second

or higher order dispersion the equation system 1.4 changes to [38]:

$$\frac{\partial A_s}{\partial z} + \frac{1}{v_{gs}}\frac{\partial A_s}{\partial t} = -i\sigma_s A_p A_i^* e^{-i\Delta k z}, \tag{1.21a}$$

$$\frac{\partial A_i}{\partial z} + \frac{1}{v_{gi}}\frac{\partial A_i}{\partial t} = -i\sigma_i A_p A_s^* e^{-i\Delta k z}, \tag{1.21b}$$

$$\frac{\partial A_p}{\partial z} + \frac{1}{v_{gp}}\frac{\partial A_p}{\partial t} = -i\sigma_p A_s A_i e^{i\Delta k z}, \tag{1.21c}$$

Eqs. 1.21 capture the main issues of three wave parametric amplification with ultrashort pulses, that are related to GVM between the interacting pulses. In particular, GVM between the pump and the signal/idler pulses limits the interaction length over which parametric amplification takes place, while GVM between the signal and the idler pulses limits the phase matching bandwidth.

In order to achieve broadband amplification, the phase mismatch Δk has to be as small as possible over a large frequency bandwidth. In the collinear geometry the wave vector mismatch can be approximated to the first order of Taylor expansion around signal central frequency ω_{s0} as:

$$\Delta k \cong -\frac{\partial k_s}{\partial \omega_s}\Delta\omega + \frac{\partial k_i}{\partial \omega_i}\Delta\omega = \left(\frac{1}{v_{gi}} - \frac{1}{v_{gs}}\right)\Delta\omega. \tag{1.22}$$

Here $\Delta\omega = \omega_s - \omega_{s0}$. The full width at half maximum (FWHM) phase matching bandwidth within the large gain approximation can be calculated from Eq. 1.9

$$\Delta\nu = \frac{2(\ln 2)^{1/2}}{\pi}\left(\frac{\Gamma}{L}\right)^{1/2}\frac{1}{\left|\frac{1}{v_{gs}} - \frac{1}{v_{gi}}\right|}. \tag{1.23}$$

where L is the crystal length. Equation 1.23 shows that the gain bandwidth is inversely proportional to the GVM between signal and idler pulses (defined as $\left|\frac{1}{v_{gs}} - \frac{1}{v_{gi}}\right|$). For a collinear geometry (see Fig. 1.3(a)), signal and idler pulses move with different group velocities and quickly separates, giving rise to pulse lengthening and bandwidth reduction. The large GVM coefficient, in other words, dramatically decreases the phase matching bandwidth.

The broadband amplification, on the other hand, can be achieved if a noncollinear geometry is used. The method was first suggested by Gale [39] and is schematically depicted in Fig. 1.2. In this case, pump and signal beams are crossed at an angle α, which is independent of signal wavelength. The idler is emitted at an angle Ω, which adjusts itself to satisfy the phase

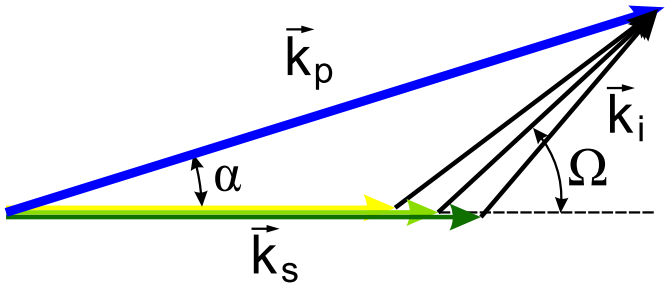

Figure 1.2: Wave-vector diagram describing the noncollinear three-wave parametric interaction.

matching condition. It can be shown, that broadband phase matching can be achieved for a signal-idler angle Ω such, that the signal group velocity equals the projection of the idler group velocity along the signal direction, that is $v_{gs} = v_{gi} \cos\Omega$ [33], as depicted in Fig. 1.3(b). The latter condition can be satisfied only if the idler has higher group velocity than the signal. From a practical point of view, it is more convenient to know the pump-signal angle α, which is given by

$$\alpha = \arcsin\left(\frac{1 - v_{gs}^2/v_{gi}^2}{1 + 2v_{gs}n_s\lambda_i/v_{gi}n_i\lambda_s + n_s^2\lambda_i^2/n_i^2\lambda_s^2}\right)^{1/2} \tag{1.24}$$

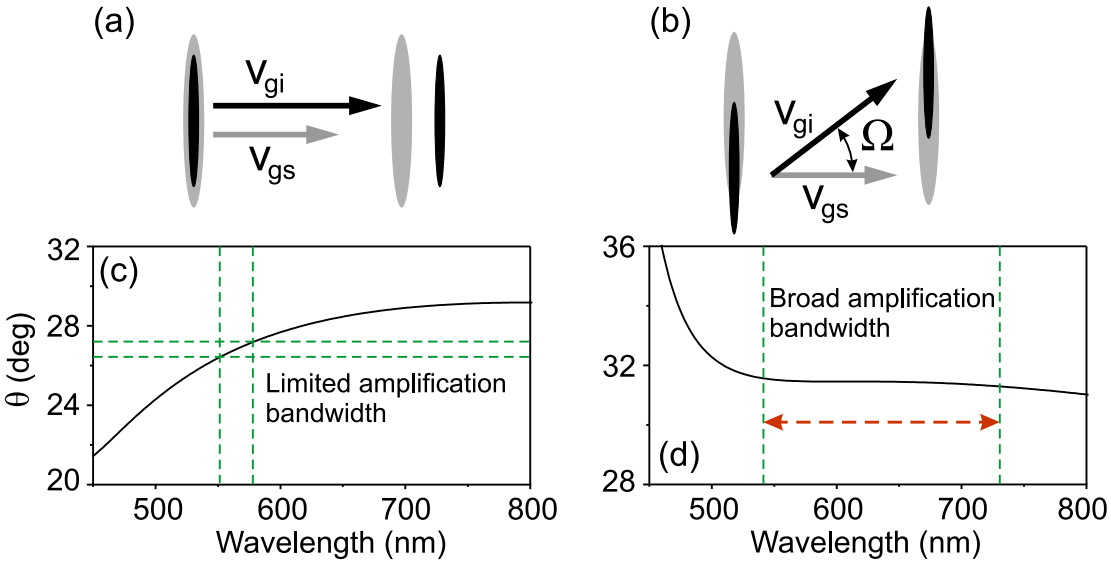

Figure 1.3: Representation of signal and idler pulses in the case of collinear interaction (a) and noncollinear interaction (b). Phase-matching curves *vs* signal wavelength for a type I BBO OPA pumped at 400 nm in (c) collinear ($\alpha = 0°$) and (d) noncollinear ($\alpha = 3.7°$) geometry.

As an example Fig. 1.3(c) and (d) shows the phase matching angle *vs* signal wavelength for two different pump-signal angle α values. The presented OPA is based on a type I BBO crystal and is pumped at 400 nm

(Ti:sapphire laser second harmonic). In a collinear configuration the phase matching angle strongly depends on the signal wavelength, as shown in Fig. 1.3(c), consequently the amplification bandwidth is narrow. By increasing the angle up to $\alpha \approx 3.7°$, simultaneous phase matching over an ultrabroad bandwidth is achieved (Fig. 1.3(d)). The latter configuration is realized in a blue-pumped supercontinuum seeded NOPA, which was used in our experiments (see Appendix I for more details).

1.5 Carrier-envelope phase and passive phase stabilization

Mathematically, a linearly polarized electric field of a pulse can be expressed as:

$$E(t) = A(t)\cos(\omega t + \phi), \tag{1.25}$$

where $A(t)$ is the electric field envelope, ω is the carrier frequency and ϕ is called the CEP also known as the absolute phase. It corresponds to the phase between the envelope and the carrier as depicted in Fig. 1.4. While

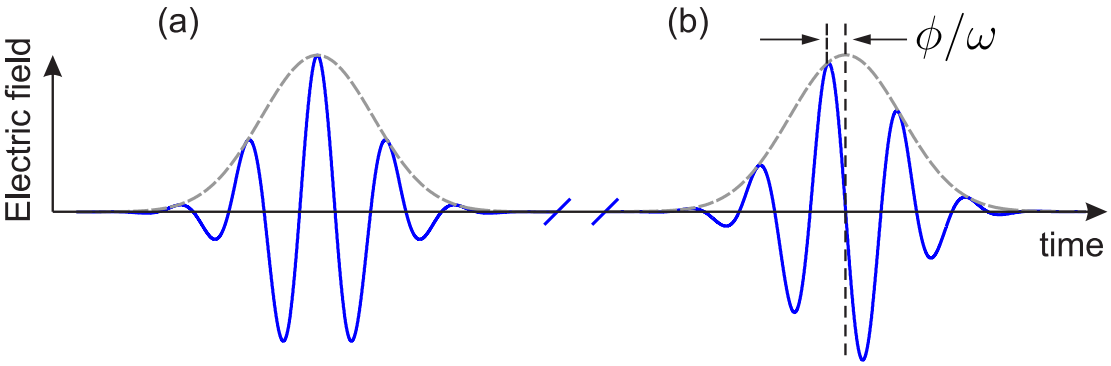

Figure 1.4: Few-cycle pulse envelope and electric field with a CEP value of: (a) $\phi = 0$ and (b) $\phi = \pi/2$.

CEP variation has a negligible effect in the case of a long pulse, it is particularly relevant for few-cycle pulses, where the pulse duration is a small multiple of an optical cycle defined as $T = 2\pi/\omega$. A change in the CEP makes a physically measurable difference only if the nonlinear interaction result is sensitive to the electric field rather than the pulse intensity. For example HHG [22], attosecond pulse generation [23], above-threshold ionization [24], multiphoton absorption [40] are very much CEP-dependent. Control of the CEP, therefore, is a prerequisite for light-matter interactions using few optical cycle pulses.

CEP can be stabilized using active method [41], or, as in the case of this thesis, a passive method suggested by Baltuška [42] can be used. In the three-wave parametric interaction, the simplified frequency and phase equations for the interacting pump, signal and idler waves can be given as

$$\omega_i = \omega_p - \omega_s, \tag{1.26a}$$

$$\phi_i = \phi_p - \phi_s - \pi/2. \tag{1.26b}$$

If pump and signal pulses are derived from the same source and have the same phase (i.e. $\phi_p = \phi_s = \phi$), then ϕ_i = const. and pulse-to-pulse fluctuations of ϕ_p (or ϕ_s) are canceled in a passive way as shown in Fig. 1.5. The latter holds also for the DFG process, where the generated difference-

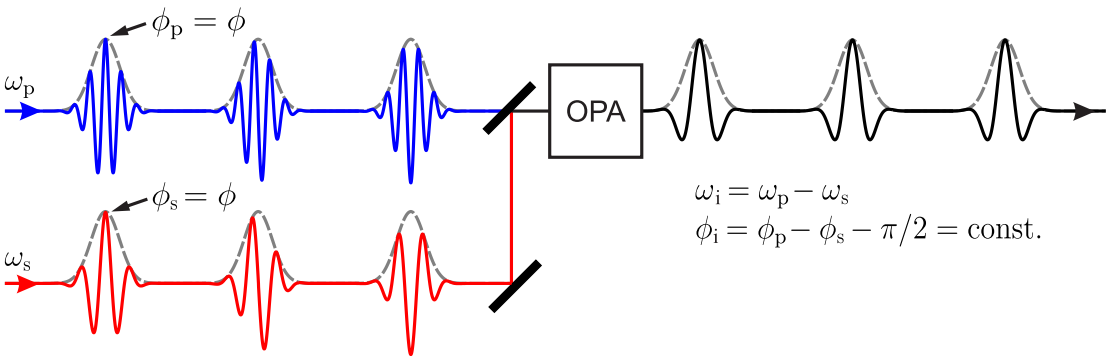

Figure 1.5: Schematic representation of a passive (all-optical) CEP stabilization via OPA.

frequency pulses emerge with a stable CEP [43, 44].

1.6 f-2f measurements of CEP jitter

Next, we explain the f-2f spectral interferometry approach for amplified pulse shot-to-shot CEP drift measurement, experimentally demonstrated by Kakehata et al. [45]. Figure 1.6 shows a typical f-2f nonlinear interfer-

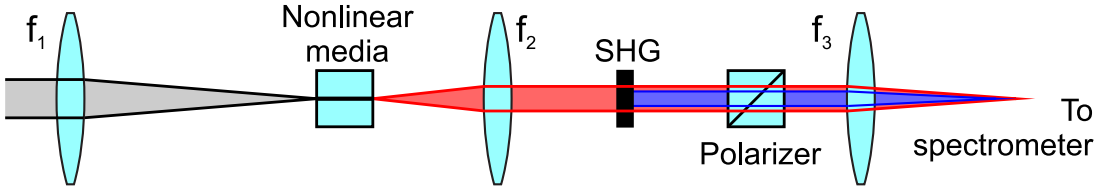

Figure 1.6: f-2f interferometer for measuring CEP drift. f_1, f_2 and f_3 are focusing and restoring lenses, SHG is the second harmonic generator.

ometer. A pulse with a CEP ϕ is first focused into a slab of a nonlinear

media (sapphire, YAG, CaF_2, etc.) to generate a supercontinuum. The spectral broadening during SC generation can be regarded as a special case of four-wave mixing, in which a new frequency ω_{SC} is generated starting from three frequencies ω_1, ω_2 and ω_3, all belonging to the pulse spectrum. The frequencies and phases of these waves are linked by the relationship

$$\omega_{SC} = \omega_1 - \omega_2 + \omega_3, \tag{1.27a}$$

$$\phi_{SC} = \phi_1 - \phi_2 + \phi_3 - \pi/2. \tag{1.27b}$$

If we consider that the mixing pulses share the same phases ($\phi_1 = \phi_2 = \phi_3 = \phi$), then the SC pulse will have the CEP:

$$\phi_{SC} = \phi - \pi/2. \tag{1.28}$$

It is important to notice, that a SC pulse retains the same value of ϕ as that of the input pulse. After generating a sufficiently broadband supercontinuum, the pulse is sent to the SHG crystal. The CEP of the resulting pulse is

$$\phi_{SH} = 2\phi_{SC} - \pi/2. \tag{1.29}$$

The spatially overlapped supercontinuum and its second harmonic (SH) are directed to a polarizer and the transmitted spectral components are sent to a spectrometer. In the frequency domain the interference between the SC and SH pulses can be expressed as

$$\begin{aligned} S(\omega) &= S_{SC}(\omega) + S_{SH}(\omega) + 2\sqrt{S_{SC}(\omega)S_{SH}(\omega)}\cos(\phi_{SH} - \phi_{SC} + \omega\tau_d) \\ &= S_{SC}(\omega) + S_{SH}(\omega) + 2\sqrt{S_{SC}(\omega)S_{SH}(\omega)}\cos(\phi - \pi + \omega\tau_d), \end{aligned} \tag{1.30}$$

where τ_d is the relative delay between SC blue part and the SH pulse, $S_{SH}(\omega)$, $S_{SC}(\omega)$ are the spectra and ϕ_{SH}, ϕ_{SC} are the CEPs of the SH and SC pulses respectively. Figure 1.7(a) shows two spectrograms generated by two successive pulses j and k with CEPs ϕ_j and ϕ_k. The fast modulation is clearly visible around 2ω, where the SH and SC spectra overlap. If the pulse CEP is not stable, the interference fringes in Fig. 1.7(a) will move from shot to shot and will vanish upon averaging. The phase drift ϕ can be evaluated employing the standard algorithm of Fourier transform spectral interferometry (FTSI) [46]. The method relies on (i) an inverse Fourier transform of the interfering part around 2ω in Fig. 1.7(a), (ii) a selection of a finite time window around τ_d (shaded area in Fig. 1.7(c)) so as to keep only the interfering product between the two fields, (iii) a Fourier transform back

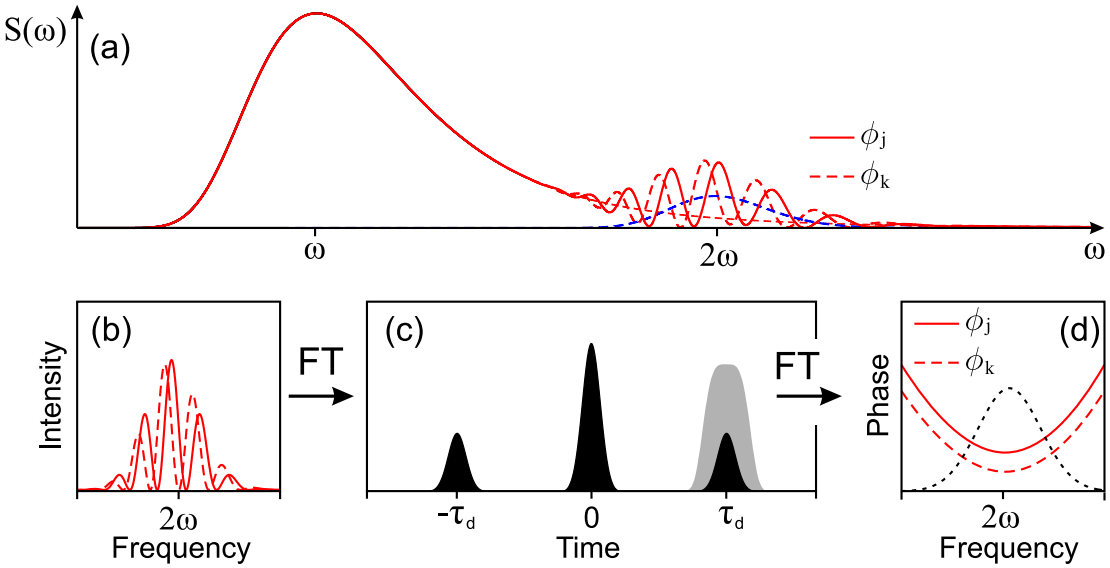

Figure 1.7: (a) f-2f spectral interferogram, (b) interfering part around 2ω, (c) its inverse Fourier transform (absolute value), (d) retrieved phase difference $\phi_{SH} - \phi_{SC}$.

into the frequency domain then allows the retrieval of the ϕ (Fig. 1.7(d)). The CEP jitter between pulses j and k is found as $\Delta\phi_{CEP} = \phi_j - \phi_k$.

The theoretical background of the f-2f nonlinear interferometry can be easily adopted to an f-3f approach, where the spectral overlap between the supercontinuum and the third harmonic pulses is measured. In this case the phase of the third harmonic pulse is

$$\phi_{TH} = 3\phi_{SC} - \pi/2, \tag{1.31}$$

while the phase difference between TH and SC pulses measured by an f-3f interferometer: $\phi_{TH} - \phi_{SC} \propto 2\phi$. It is clear, that the phase shift of an spectral interference fringe is affected by the CEP jitter two times more for the f-3f interferometry than for the f-2f approach. The retrieved f-3f phase jitter value, thus has to be divided by a factor of 2.

Chapter 2

Generation and optical parametric amplification of ultrashort UV pulses

Material related to this chapter was published in [A1 – A6]

2.1 Motivation

Generation and applications of the ultrashort light pulses in the ultraviolet attract much scientific and technological interest since the inception of nonlinear optics. Femtosecond ultraviolet laser pulses are on demand for many spectroscopic applications studying ultrafast processes in photochemistry and photobiology [47]. Many challenging applications in material processing, such as laser processing via surface ablation [48], micro-printing of biomaterials [49], long-period fiber grating fabrication [50], in-depth modification of transparent solids [51], laser micro-structuring [52], to mention a few, require ultrashort laser pulses with energy of tens of microjoules.

Among variety of nonlinear optical techniques to generate ultrashort light pulses in the ultraviolet, four-photon interactions in transparent isotropic media attract steadily growing interest. In particular, four-wave mixing in noble gases and air allows direct generation and/or amplification of the ultrashort ultraviolet light pulses and became a convenient technique to produce microjoule ultraviolet pulses with duration of few tens of femtoseconds [11, 12, 14–17, 53]. Recent advances in generation of few-cycle ultraviolet pulses in gases now challenge extreme pulse durations of $\sim$ 1-fs [54, 55]. These techniques combine all the essential prerequisites for efficient four-wave parametric amplification to take place - phase-matching,

long interaction length maintaining high pump intensity, and broadband amplification supported by low dispersion of the gaseous media, and typically deliver pulses of $\sim$ 10 µJ energy with pumping at the mJ energy level.

Experimental studies of the four-wave interactions in transparent solids, however, were limited mostly to generation and amplification of the ultrashort light pulses in the visible and infrared spectral range, using tightly focused laser beams [19, 20, 32, 56, 57], with quite a few studies devoted to ultraviolet pulse generation. In particular, third-harmonic generation was experimentally demonstrated, applying different interaction schemes, with [58] or without [59] assistance of the second-order nonlinearity in UV-transparent birefringent crystals, difference-frequency generation [60] and direct frequency tripling [61] in liquids. Despite the fact that condensed media possess much larger third-order susceptibility as compared to gases, severe limitations are imposed by high material dispersion. That is, non-degenerate four-wave interactions could be phase-matched only noncollinearly, which impose substantial reduction of the interaction length in tight focusing geometry. Moreover, high intensity of the applied laser field gives rise to a series of competing nonlinear effects – self- and cross-phase modulation, self-focusing, beam break-up and filamentation, and eventually optical breakdown, which occur almost at the same intensity threshold [18]. So far, typical energy of the pulses amplified via parametric four-wave processes in bulk solid state media were in the order of $\sim$ 1 µJ in the visible [19] and few hundreds of nJ in the MIR [20] spectral range.

Recently, a new route in practical implementation of efficient four-wave optical parametric amplification in condensed bulk media was suggested making use of cylindrical focusing geometry [62, 63], which allows to fulfill the noncollinear phase-matching condition without reducing the interaction length as explained in the following section.

2.2 Harmonic generation via four-wave difference frequency mixing

The most straightforward way to convert the radiation emitted by solid-state lasers into the ultraviolet spectral range is the TH generation. In a medium with $\chi^{(3)}$ nonlinearity there are two four-wave mixing configurations, which may lead to third harmonic generation. The first approach

considers direct frequency tripling, that is $3\omega = \omega + \omega + \omega$. The phase matching condition could be fulfilled only in media with negative dispersion, e.g. metal vapors [64], however the overall process is inefficient due to high absorption. On the other hand, in transparent media with positive dispersion, the phase-mismatch could be greatly reduced by means of tight focusing [65]. In this case, however, energy conversion process is limited by low intrinsic nonlinearity of gaseous media and short interaction length. The efficiency of TH generation could be improved by use of guided wave propagation in the filamentation regime [11], but still it does not exceed 1%. In condensed media, TH generation efficiency in the filamentation regime still remains remarkably low (10^{-6}) due to severe phase-matching limitations [61]. The second approach is based on four-wave difference-frequency mixing ($3\omega = 2\omega + 2\omega - \omega$) and allows the phase matching condition to be perfectly fulfilled in any transparent medium. More importantly, the four-wave difference-frequency mixing method could be easily extended to any other higher laser harmonic generation by choosing appropriate frequencies of the input radiation. In what follows, we present experimental results on efficient generation of 1-ps pulses at third (Sect. 2.2.1), fifth (Sect. 2.2.2), and sixth (Sect. 2.2.3) harmonics of the Nd:glass laser by phase matched four-wave difference-frequency mixing using cylindrical beam focusing geometry. The complete geometrical arrangement of FWOPA is illustrated in Fig. 2.1, providing top and side views of the interaction. The focus-

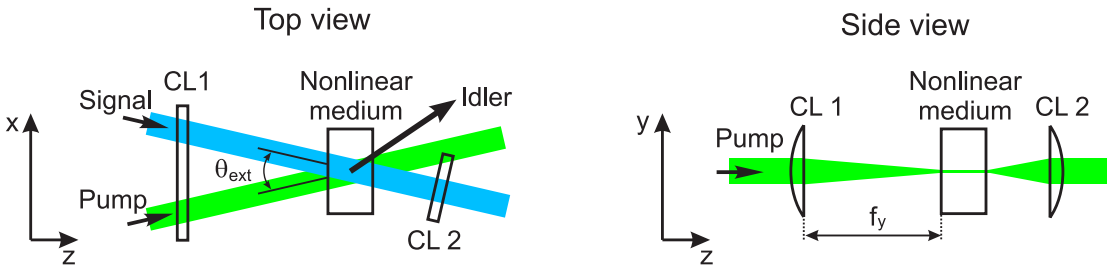

Figure 2.1: Geometrical beam arrangement in the FWOPA. CL1 and CL2 are cylindrical lenses for beam focusing and restoring, respectively. θ_{ext} is the external phase matching angle, $\theta_{\text{ext}} \approx n(\omega_s)\theta$.

ing is performed in the vertical (y) plane, while the beams are crossed in the horizontal (x) plane, thus ensuring a good spatial overlap along entire sample length. It is important to note that in this configuration, catastrophic self-focusing and break-up of high-intensity elliptical pump beam into multiple filaments is quenched due to strong four-wave coupling. As a result, the pump, signal and idler beams simultaneously reshape into stable

1-dimensional spatial solitons [62, 63]. Under these settings, the four-wave parametric amplification could be performed with high energy (milijoule) pump pulses, at the same time keeping the laser beam intensity reasonably below the optical damage threshold of the nonlinear medium.

2.2.1 Third harmonic generation in fused silica

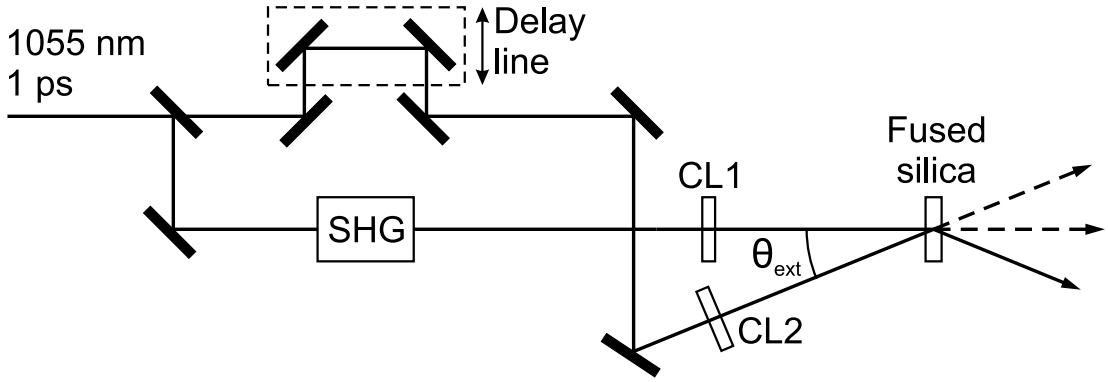

Figure 2.2: Experimental setup. SHG is the second harmonic generator, CL1 and CL2 are the cylindrical focusing lenses, θ_{ext} denotes the external phase matching angle, $\theta_{\text{ext}} \approx n(\omega)\theta_{\text{pm}}$.

The experiment was performed using a commercial Nd:glass laser system (Twinkle, Light Conversion Ltd.), which delivered 1-picosecond pulses at 1055 nm with energy up to 6 mJ at 10 Hz repetition rate. The laser output was split into two parts. The first portion of the laser radiation was frequency doubled in a 11-mm-thick KDP crystal (yielding photons at 527 nm) and then recombined with a fresh fundamental harmonic (1055 nm) so as to produce TH at 351 nm through the four-wave difference frequency mixing process, i.e. $3\omega = 2\omega + 2\omega - \omega$ (see Fig. 2.2). Intense fundamental and second-harmonic laser beams were focused into the UV-grade (type KU-1), 3-mm-long fused silica sample using cylindrical lenses CL1 ($f_x = \infty$, $f_y = +750$ mm) and CL2 ($f_x = \infty$, $f_y = +500$ mm) respectively. The FWHM size of both elliptical pump beams was measured as 5 mm $\times$50 µm. The beams were crossed at $\theta_{\text{pm}} = 11^\circ$ angle, which was found from the phase matching condition (Eq. 1.19). The energy ratio of the fundamental and second-harmonic beams was adjusted as $E_\omega : E_{2\omega} = 1 : 4$, according to Manley-Rowe relation in order to ensure optimal photon yield. The energy of the overall pump $E_p = E_\omega + E_{2\omega}$ was varied up to 1.55 mJ, being limited by the optical damage of the fused silica sample.

Geometrically, at large beam crossing angle ($\theta_{\text{pm}} = 11^\circ$), the physical

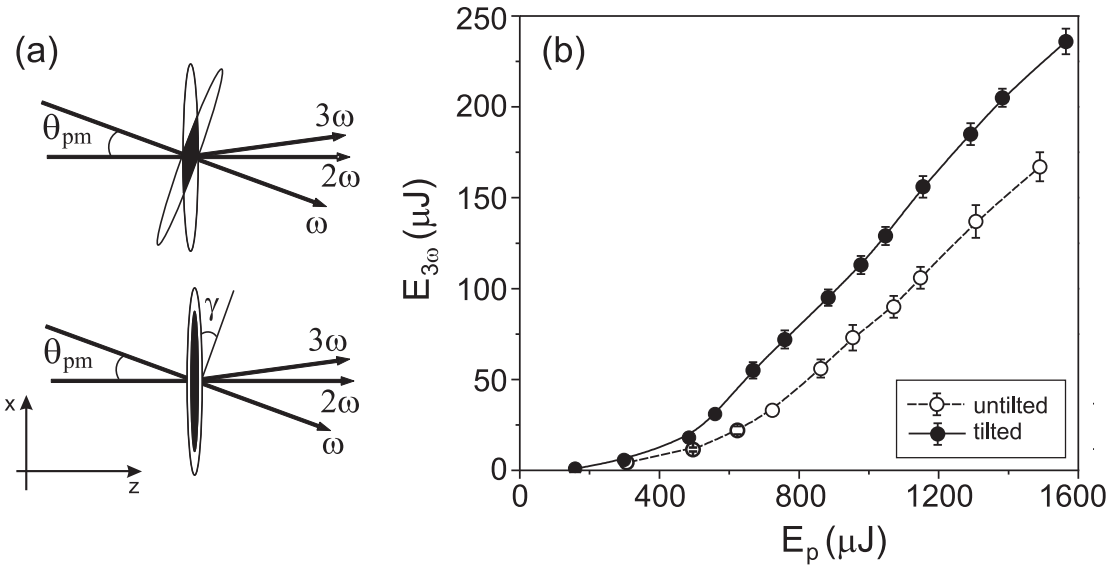

Figure 2.3: (a) Schematic representation of pulse/beam overlap (indicated by black area) in the phase matching plane with untilted (upper illustration) and tilted (lower illustration) pulses. (b) Experimentally measured third-harmonic pulse energy $E_{3\omega}$ versus pump energy with untilted (dashed curve and open circles) and tilted (solid curve and full circles) pulses.

beam/pulse overlap area within the nonlinear medium becomes greatly reduced, as illustrated in the upper picture of Fig. 2.3(a). Note, that the cylindrically focused laser beam has a width of 5 mm FWHM along its long (x) axis in the phase matching plane, whereas the physical length of 1 ps pulses inside the sample is just ~ 0.2 mm. Therefore noncollinearly propagating pump beams overlap only partially, yielding a narrow third-harmonic beam and, as a consequence, less efficient energy conversion. The overlap geometry was improved by introducing the pulse front tilt on the fundamental harmonic pulse, as schematically illustrated in the lower picture of Fig. 2.3(a). The pulse-front tilt angle $\gamma = 8.6^\circ$ was produced by means of accomplishing four passes through the TF5 glass prism with an apex angle of 60° at the minimum deviation geometry. Figure 2.3(b) compares the results of third-harmonic generation with untilted and tilted pulses by plotting third-harmonic pulse energy $E_{3\omega}$ as a function of the pump energy. Indeed, pulse-front tilting of the fundamental frequency pulse has led to an increase of the third-harmonic pulse energy by $25 - 30\%$, with the highest value of $E_{3\omega} = 230$ μJ as measured at maximum pump energy of $E_p = 1.55$ mJ. This result suggests the energy conversion efficiency as high as 15% (or $\approx 10\%$ from fundamental frequency to TH), which is the highest number to our knowledge achieved in the third-harmonic generation via pure cubic

nonlinearity reported up to date. The obtained efficiency, however is still lower as compared to frequency conversion schemes based on sum-frequency mixing $3\omega = 2\omega + \omega$ in $\chi^{(2)}$ materials, where $\approx 30\%$ energy conversion is routinely achieved.

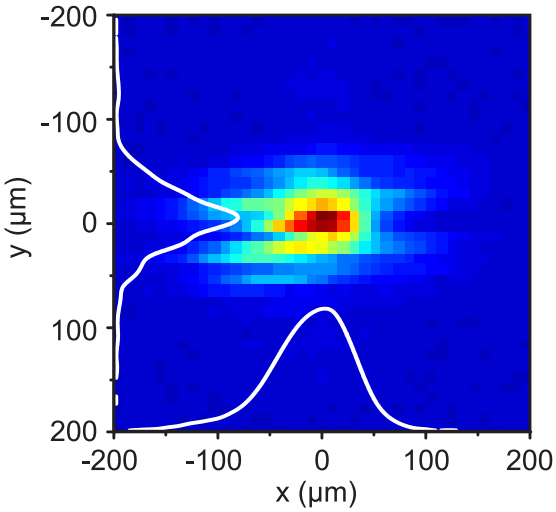

Figure 2.4: Intensity distribution of the third harmonic beam and it's central cross-sections along the principal axes at the focal plane of an $f = +1$ m spherical lens.

And finally, the focusability of the TH beam was measured. For many practical applications the beams with circular symmetry are required, therefore the circular symmetry of the elliptical TH beam was restored using $f_y = +100$ mm cylindrical lens. Figure 2.4 shows the measured TH beam intensity profile and its relevant cross-sections at the focal plane of $f = +1$ m spherical lens. The focused TH beam exhibits good focusability and the estimated beam quality is ≈ 1.5 times of the diffraction limited Gaussian beam.

2.2.2 Fifth harmonic generation in CaF_2 and MgF_2

The four-wave difference-frequency generation method in solids was further extended to even shorter wavelengths in the DUV, by demonstrating efficient fifth-harmonic generation in CaF_2 and MgF_2 samples. The phase matched fifth-harmonic generation was achieved by mixing third and fourth-harmonic pulses of the Nd:glass laser (whose wavelengths are 351 nm and 264 nm, respectively), producing the radiation at 211 nm through the difference-frequency mixing process $5\omega = 4\omega + 4\omega - 3\omega$. The fourth harmonic was obtained by frequency doubling in 11-mm and 4-mm-thick

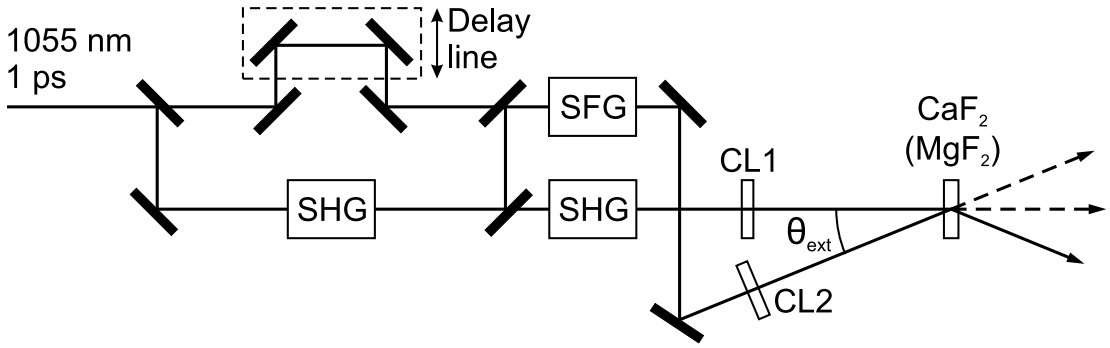

Figure 2.5: Experimental setup. SHG is the second harmonic generator, SFG is the sum-frequency generator, CL1 and CL2 are the cylindrical focusing lenses, θ_{ext} denotes the external phase matching angle, $\theta_{\text{ext}} \approx n(3\omega)\theta_{\text{pm}}$.

KDP crystals (SHG in Fig. 2.5), while the third harmonic was generated by mixing fundamental and second harmonic in a 4-mm-thick KDP crystal (SFG in Fig. 2.5). The beam focusing and interaction geometry was essentially identical to the one described in the previous section, with the phase matching angles of $\theta_{\text{pm}} = 8.3°$ and $\theta_{\text{pm}} = 7.2°$ calculated for CaF_2 and MgF_2, respectively, and the input beam dimensions of 2.9 mm ×30 µm at the input face of the nonlinear medium. Since MgF_2 crystal is birefringent, its optical axis was aligned at 0° to normal incidence. The length of crystal samples was chosen as $l = 4$ mm, as a compromise of the group velocity mismatch lengths between the fourth-harmonic and fifth-harmonic pulses of 3.2 mm in CaF_2 and 4.1 mm in MgF_2. The linear and nonlinear

Crystal	E_g, eV	T, µm	n_2, cm^2/W	θ_{pm}, deg	L_{GVM}, mm	β_{264}, cm/W
CaF_2	10.0	0.13 – 9.4	4.2×10^{-16}	8.3	3.2	7.3×10^{-12}
MgF_2	11.8	0.13 – 7.4	1.5×10^{-16}	7.2	4.1	1.9×10^{-12}

Table 2.1: Relevant linear and nonlinear properties of CaF_2 and MgF_2 crystals for fifth-harmonic generation. E_g is the bandgap, T is transmission range at 1 cm^{-1} level [66], n_2 is the nonlinear refractive index [66], θ_{pm} is the phase matching angle calculated from the Sellemier equation [67], L_{GVM} is the group velocity mismatch length, calculated for 1-ps pulses, β_{264} is the two-photon absorption coefficient, measured in this work.

parameters of CaF_2 and MgF_2, relevant to the present experiment are listed in Table 2.1. Both crystals possess very similar threshold damage fluence as measured in the visible and near infrared [68], and considering that it scales inversely with frequency, the expected values are in the order of ~ 0.5 J/cm^2 for 1-ps pulses at 264 nm. The input energy ratio between the pump

waves was set as $E_{4\omega} : E_{3\omega} = 8 : 3 = 2.6$, according to interacting photon energy. The overall pump energy was defined as $E_p = E_{4\omega} + E_{3\omega}$ and was varied up to ~ 0.5 mJ.

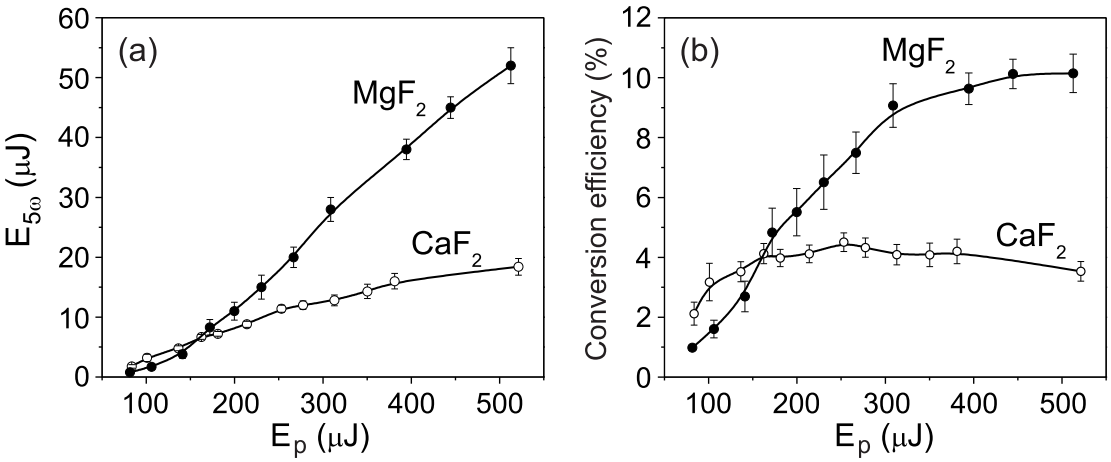

Figure 2.6: (a) Experimentally measured fifth-harmonic energy $E_{5\omega}$ *vs* pump energy in CaF_2 (open circles) and MgF_2 (full circles) crystals. (b) Energy conversion efficiency of the fifth-harmonic generation process.

Figure 2.6 summarizes the main experimental results measured in CaF_2 and MgF_2 crystals. Fifth-harmonic pulse energy $E_{5\omega}$ versus pump energy is depicted in Fig. 2.6(a), while Fig. 2.6(b) shows energy conversion efficiency calculated as $E_{5\omega}/(E_{4\omega} + E_{3\omega})$ and demonstrates that the interaction regime in both media is driven into saturation. In CaF_2, the highest energy conversion of 4.5% was measured at $E_p = 250$ µJ, yielding the fifth-harmonic pulses with energy of $E_{5\omega} = 13$ µJ. Since the energy conversion saturates, further increase of the fifth-harmonic pulse energy, measured at higher pump energies is small ($E_{5\omega} = 18$ µJ at $E_p = 520$ µJ). Significantly better results were achieved in MgF_2 sample, where fifth-harmonic pulse energy as high as $E_{5\omega} = 52$ µJ at $E_p = 500$ µJ was measured, that equates to $\sim 10\%$ energy conversion efficiency (or $\approx 2.5\%$ from fundamental frequency to fifth-harmonic). In $\chi^{(2)}$ materials the fifth-harmonic is usually generated via $5\omega = 4\omega + \omega$ interaction, with $\approx 10\%$ fundamental-to-fifth harmonic conversion efficiency.

It is important to note that the shorter and the most intense pump wave, i.e. the fourth-harmonic pulse, is the subject to two-photon absorption. To verify this, the nonlinear transmission measurements were accomplished in our samples with fourth-harmonic pulse alone, since exact values of the two-photon absorption coefficients for CaF_2 and MgF_2 crystals are not provided in the literature. The nonlinear transmission measurement methodology

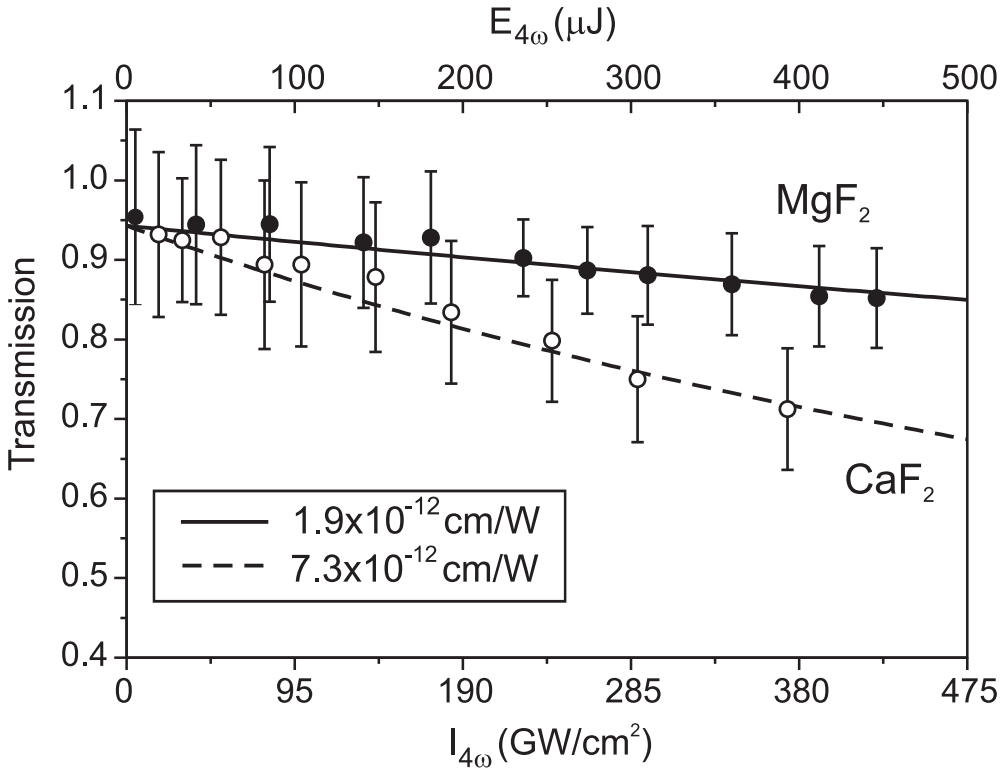

Figure 2.7: Nonlinear transmission of 4-mm-long CaF_2 (open circles) and MgF_2 (full circles) samples versus fourth-harmonic pulse intensity. Dashed and solid curves show the best fit yielding two-photon absorption coefficients $\beta_{264} = 7.3 \times 10^{-12}$ cm/W and $\beta_{264} = 1.9 \times 10^{-12}$ cm/W, respectively.

and the two-photon absorption coefficient retrieval algorithm was essentially similar to that described in [69]. In the present experiment we have just ascertained that the dimensions of the input beam had not changed during the propagation in the sample. Indeed, the estimated Rayleigh range for the 30 μm (FWHM) input beam is in the order of $\sim$ 15 mm, and thus ensures that the intensity change associated with diffraction spread of the input beam was negligible during its propagation in the 4-mm-long sample. Figure 2.7 shows the results of the nonlinear transmission measurements in 4-mm-long CaF_2 and MgF_2 samples, along with the best-fit yielding two-photon absorption coefficients of $\beta_{264} = 7.3 \times 10^{-12}$ cm/W and $\beta_{264} = 1.9 \times 10^{-12}$ cm/W for CaF_2 and MgF_2, respectively.

Taking into consideration the nonlinear parameters of both media, the marked differences in fifth-harmonic generation results obtained in CaF_2 and MgF_2 crystals (see Fig. 2.6) can be explained. First of all, larger nonlinearity of CaF_2 (that is in fact proportional to the nonlinear refractive index n_2) makes the fifth-harmonic generation process more efficient as compared to MgF_2 in the input pump energy range of $80 - 150$ μJ. Conversely, in the

high pump energy limit, energy losses due to two-photon absorption of one of the pump waves (i.e. fourth-harmonic) in CaF_2 are considerably larger that those in MgF_2, so further pump intensity increase has just very small effect on the fifth-harmonic pulse energy. On the other hand, the four-wave difference-frequency generation process in MgF_2 saturates at higher pump intensity owing to its smaller nonlinearity, which combined with small two-photon absorption for the fourth-harmonic wave, allows much higher fifth-harmonic pulse energy to be achieved. It is worth mentioning that the nonlinear losses experienced by the fifth-harmonic pulse in MgF_2 are also expected to be considerably lower than those in CaF_2. And finally, for the repetition rate of 10 Hz of our laser, permanent color center formation due to intense ultraviolet irradiation has not been observed in none of the used crystal samples.

It is important to note that the fifth-harmonic can also be generated via $5\omega = 3\omega + 3\omega - \omega$ difference-frequency mixing. The latter configuration is more quantum efficient, since no fourth-harmonic is required to generate separately. The $5\omega = 4\omega + 4\omega - 3\omega$ approach, on the other hand, allowed us to estimate the nonlinear losses, experienced by the intense fourth-harmonic, and to choose the best material for the next experiment, i.e. sixth-harmonic generation via $6\omega = 4\omega + 4\omega - 2\omega$ mixing process.

2.2.3 Sixth harmonic generation in MgF_2

Generation of the ultrashort light pulses in the VUV in the solid state media is a formidable task because of high group velocity mismatch between the interacting pulses, high linear and nonlinear absorption and phase matching constraints in the crystals with quadratic nonlinearity. To date, the shortest wavelengths generated via quadratic phase-matched interactions are reported in LBO (172.7 nm) [70], $CsLiB_6O_{10}$ (175 nm) [71], $KB_5O_8 \times 4H_2O$ (166 nm) [72] crystals. Typical generated pulse energy ranges from tens to hundreds of nanojoules in the femtosecond regime.

In this section a high potential of wide-bandgap MgF_2 crystal for the generation of VUV radiation by four-wave difference-frequency mixing is demonstrated. Specifically, the sixth-harmonic of the Nd:glass laser (176 nm) is generated by mixing 1-ps fourth-harmonic (264 nm, obtained by frequency doubling in 11-mm and 4-mm-thick KDP crystals) and second-harmonic (527 nm) pulses in 2-mm-long MgF_2 sample through four-wave

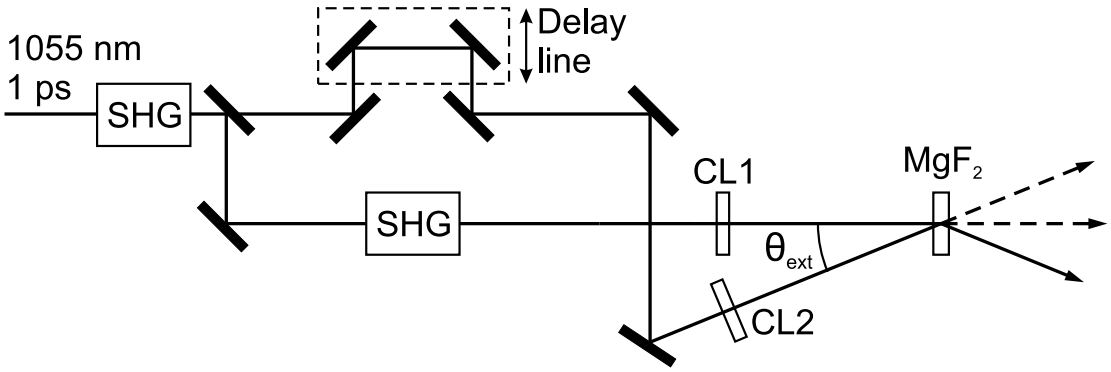

Figure 2.8: Experimental setup. SHG is the second harmonic generator, CL1 and CL2 are the cylindrical focusing lenses, θ_{ext} denotes the external phase matching angle, $\theta_{\text{ext}} \approx n(2\omega)\theta_{\text{pm}}$.

difference-frequency mixing, $6\omega = 4\omega + 4\omega - 2\omega$, as schematically depicted in Fig. 2.8. The particular details of the experiment are as follows. The beam focusing conditions were identical as those in the fifth-harmonic generation case. The fourth-harmonic and second-harmonic beams were crossed at the phase matching angle of $\theta_{\text{pm}} = 20°$. In order to optimize the pulse/beam overlap area, the second-harmonic pulse-front was tilted by $\gamma = 23°$ using a diffraction grating with 600 lines/mm at 43° incidence and second diffraction order. The length of MgF_2 crystal ($l = 2$ mm) was chosen to be close to the group velocity mismatch length calculated for 1-ps pulses ($L_{\text{GVM}} = 1.7$ mm). The energy of the sixth-harmonic pulse was measured using pyroelectric energy meter Ophir Nova II with pyroelectric detector head PE9-SH. The crystal and detector head were placed in a container with continuously refilled pure nitrogen atmosphere, so as to avoid strong absorption by the oxygen molecules. The energy ratio of the input beams was chosen as $E_{4\omega} : E_{2\omega} = 8 : 2 = 4$, and the overall pump energy was varied from 0.1 to 0.95 mJ.

The sixth-harmonic pulse energy $E_{6\omega}$ and energy conversion efficiency versus pump energy is plotted in Fig 2.9. The highest sixth-harmonic pulse energy of $E_{6\omega} = 10$ µJ was measured at $E_p = 0.9$ mJ, that is the highest energy to our knowledge in the near VUV spectral range obtained with 1-ps pulses. The energy conversion curve exhibits a broad plateau for the input pump energy in the range of $0.5 - 0.9$ mJ, with almost constant energy conversion efficiency of $\sim 1.1\%$, indicating that the conversion process is driven into saturation. It is important to note that at even high UV and VUV irradiation fluence MgF_2 crystal shows no photo-induced darkening (color center formation).

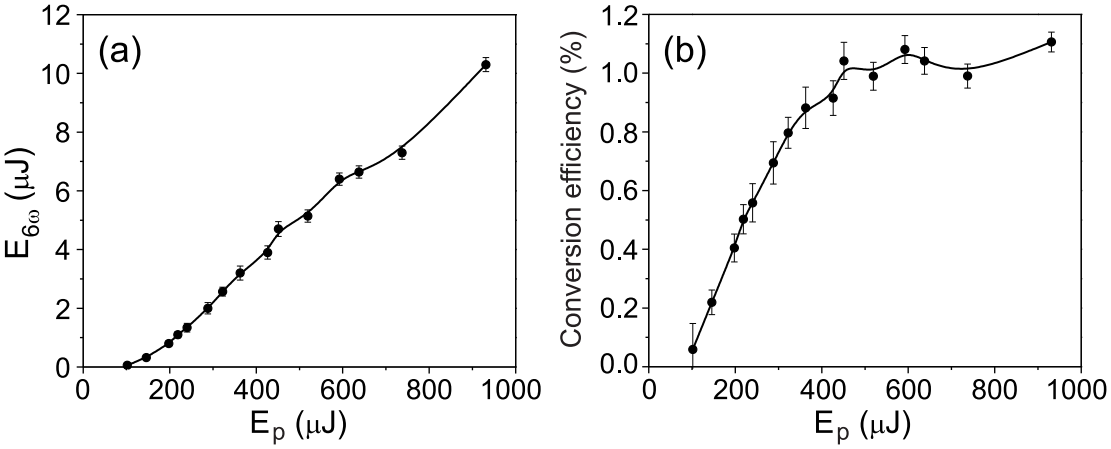

Figure 2.9: (a) Sixth-harmonic pulse energy $E_{6\omega}$ and energy conversion efficiency (b) versus pump energy in 2-mm-long MgF_2 crystal. Curves serve as guides for the eye.

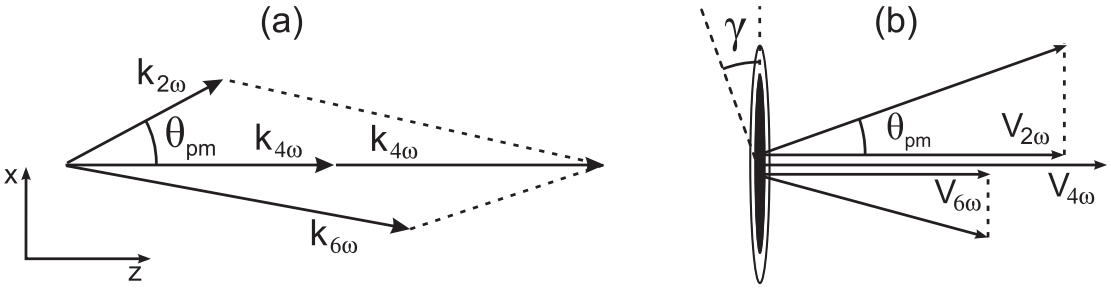

Figure 2.10: (a) Wave vector diagram for the sixth-harmonic generation. Optical axis of MgF_2 crystal is adjusted for normal incidence of the fourth-harmonic beam. (b) Schematic representation of the interacting beam/pulse overlap and pulse group velocities and their projections along the propagation axis.

And finally, the sixth-harmonic pulse width was estimated considering that the duration of the sixth-harmonic pulse equals to the time separation between the fastest (fourth-harmonic) and the slowest (sixth-harmonic) pulses over the crystal length. The calculated projections of the group velocities are $v_{2\omega} = 0.67925c$, $v_{4\omega} = 0.68591c$ and $v_{6\omega} = 0.61191c$ along the propagation axis (z) direction, as illustrated in Fig. 2.10(b), with account for noncollinear propagation and pulse-front tilt of the second harmonic pulse. A simple estimation yields $\tau_{6\omega} = l(1/v_{6\omega} - 1/v_{4\omega}) \approx 1.2$ ps, provided that the two-photon absorption for the sixth-harmonic radiation is small.

In conclusion, efficient ultraviolet harmonics generation of the Nd:glass laser by means of phase-matched four-wave difference frequency generation in UV-transparent solids was demonstrated. Specifically, generation of third-harmonics at 351 nm in fused silica (with 15% energy conversion efficiency)

and fifth-harmonics at 211 nm in CaF_2 and MgF_2 crystals (with 10% energy conversion efficiency) was experimentally demonstrated. It was shown, that the pulse/beam physical overlap area and therefore the overall efficiency of the four-wave difference frequency generation process in the noncollinear interaction is greatly improved by pulse front tilting. Complimentary measurement of the nonlinear transmission at 264 nm (that is wavelength of the shortest pump pulse) has yielded two-photon absorption coefficients of CaF_2 and MgF_2, indicating that the latter crystal possess the lower two-photon absorption ($\beta_{264} = 1.9 \times 10^{-12}$ cm/W). Taking this advantage, for the first time to our knowledge generation of VUV radiation by means of four-wave difference-frequency mixing in MgF_2 was demonstrated. Ultrashort light pulses with energy as high as $\sim$ 10 µJ at 176 nm (e.g. sixth harmonic of the Nd:glass laser) were generated with reasonably high energy conversion efficiency (>1%).

2.3 Four-wave optical parametric amplification

Efficient generation of tunable < 50 fs ultraviolet pulses is a non-trivial task. Optical parametric amplifiers based on non-centrosymmetric media with quadratic nonlinearity efficiently operate in the visible and mid-infrared spectral range, however, their efficiency drops significantly in the ultraviolet due to high group velocity mismatch, and increased linear and nonlinear (mainly two-photon) absorption of the pump wave [7, 8]. Therefore, the most straightforward way for tunable femtosecond UV pulse generation relies on the frequency doubling or sum-frequency conversion of the ultrashort pulses provided by the OPAs operating in the visible and NIR [73, 74]. However, the frequency conversion efficiency in most cases does not exceed 20% and drops down notably, when the pulse duration approaches 10 fs. Therefore typical energy of tunable femtosecond UV pulses of around several µJ is routinely achieved. The frequency conversion process is difficult to optimize because of large group velocity mismatch and group velocity dispersion, which in turn restrict achieving broadband phase matching over wide frequency band. Various modifications of the achromatic phase-matching technique, such as pulse front tilting and pulse chirping, help to solve broadband phase-matching issues, but on the other hand, require complex experimental setups [10, 75–77]. The UV pulse energy might be improved using frequency doubling of high-energy NOPA [78], however, commercial devices

routinely deliver much lower energy output [79].

There are several alternatives for ultraviolet pulse generation. The first considers non-resonant four-wave parametric interactions in gases, either in the guided wave [12, 14], or in the filamentation regime [16], where many issues related to high material dispersion and nonlinear absorption could be circumvented. These methods offer a wide choice of achievable wavelengths, and more recently, generation of sub-50-fs VUV pulses in argon has been demonstrated [80]. The second alternative suggests the use of four-wave parametric interactions in transparent isotropic solid-state media, which have larger dispersion, but also have much greater cubic nonlinearity.

In the following sections we show that solid-state media based FWOPA is capable of supporting broadband amplification. Specifically, in Sect. 2.3.1 broadband four-wave optical parametric amplification around 330 nm is investigated theoretically and experimentally, while Sect. 2.3.2 demonstrates a simple and efficient method for frequency up-conversion of 35 fs visible pulses into ultraviolet via four-wave optical parametric chirped pulse amplification.

2.3.1 Four-wave optical parametric amplification of broadband ultraviolet pulses

Experimental setup

The experiment was performed using a commercial Nd:glass laser system, which delivered 1-picosecond pulses. After the frequency doubling in a 11-mm-thick KDP crystal (SHG in Fig. 2.11) we had 1-ps, 3-mJ energy pulses at 527 nm. The beam was then split into two parts. The smaller portion of the laser radiation (1 mJ) was made variable in energy by means of the attenuator ($\lambda/2$ plate and thin film polarizer) and served as a pump for the FWOPA. The larger portion of the laser radiation (2 mJ) was used to pump the optical parametric generator/amplifier system (Topas, Light Conversion Ltd.), which delivered $\sim$1 ps pulses in 750–1200 nm spectral range. After a frequency up-conversion stage (e.g. sum-frequency mixing with fresh 527 nm radiation in 3-mm-thick KDP crystal) tunable ultraviolet pulses in the range of 310–365 nm were generated. These pulses, with energy of 10 µJ, further served as a seed signal for the FWOPA. The temporal delay between co-polarized pump and seed signal pulses was adjusted using a motorized delay line. The pump and seed signal beams were focused using

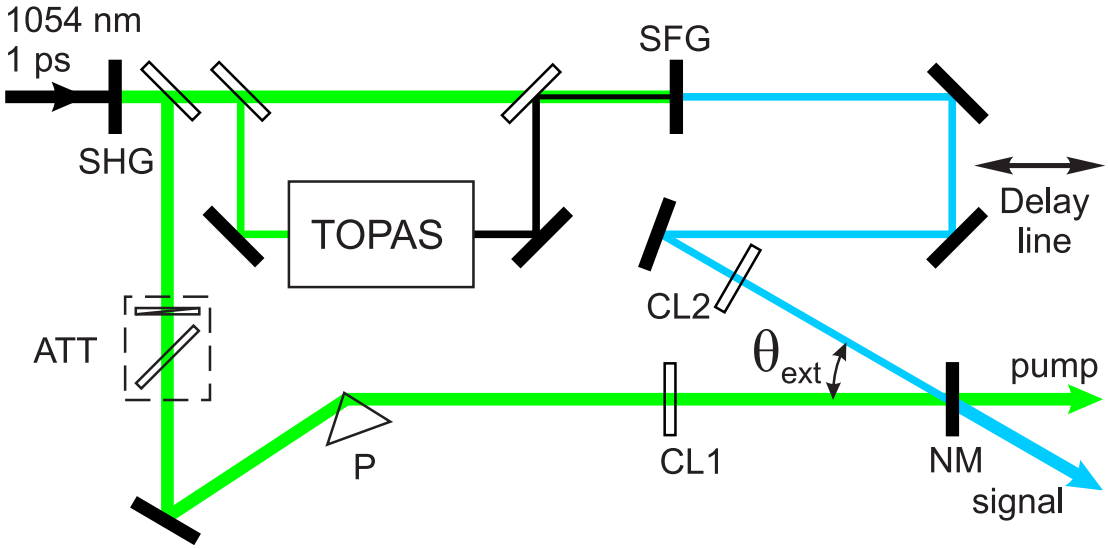

Figure 2.11: Experimental setup. TOPAS is the optical parametric amplifier, SHG is the second harmonic generator, SFG is the sum frequency generator, ATT is the attenuator, CL1 and CL2 are the cylindrical focusing lenses. P is the pulse-front tilting prism, NM is the nonlinear medium, θ_{ext} denotes the external phase matching angle, $\theta_{\text{ext}} \approx n(\omega_s)\theta_{\text{pm}}$.

cylindrical lenses CL1 (f_y=+750 mm; f_x=∞) and CL2 (f_y=+500 mm; f_x = ∞), respectively, so as to ensure mode matching at the input face of the nonlinear medium. Cylindrical focusing yielded respective FWHM dimensions of the pump and seed signal beams of 4.7 mm×55 µm and 3 mm×50 µm. The geometrical beam arrangement is depicted in detail in Fig. 2.1. As an amplifying medium we have chosen fused silica and CaF_2 crystals, which possess wide transparency range, high optical damage threshold and low nonlinear absorption for the wavelengths of interest. The relevant optical properties of fused silica and CaF_2 are listed in the Table 2.2.

Crystal	E_g, eV	$\Delta\lambda$, µm	n_2, $\times 10^{-16}$ cm^2/W	F_{th}, J/cm^2
Fused silica	7.8	0.17-3.4	2.2	1.3
CaF_2	10	0.13-9.4	3.3	1

Table 2.2: Optical properties of fused silica and CaF_2. E_g is the band gap, $\Delta\lambda$ is the transparency range at α=1 cm^{-1} level, n_2 is the nonlinear refractive index at 532 nm [66] and F_{th} is the optical damage threshold for 1-ps pulses [68].

The diagram of interacting wave vectors is depicted in the inset of Fig. 2.12. The phase matching angle θ_{pm} was found from Eq. 1.19 while the dispersion relations for linear refractive indexes $n_0(\omega)$ were calculated using Sellmeier formulas from Ref.[66].

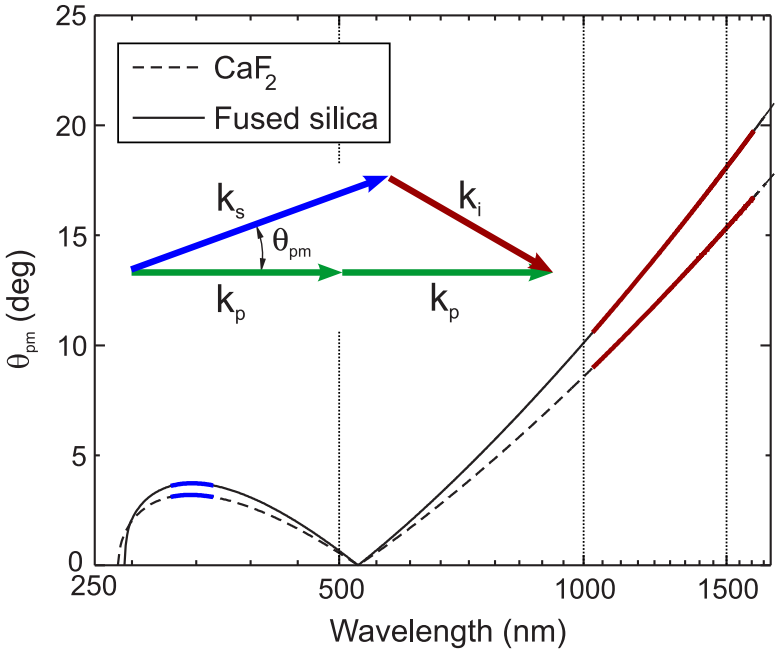

Figure 2.12: Phase-matching curves for the four-wave parametric amplification in fused silica and CaF_2 pumped with $\lambda_p = 527$ nm pulses. Wavelength range for expected broadband amplification of the signal wave and corresponding idler wave range are highlighted by the bold curves. Inset shows wave vector diagram.

The phase-matching curves for fused silica and CaF_2 are plotted in Fig. 2.12 and show a similar character, which indicates only very slight variation of the phase-matching angle for the signal wavelengths around $\lambda_s = 330$ nm, and therefore suggests that the broadband four-wave parametric amplification could be achieved in this signal wavelength range. For the central wavelength of $\lambda_s = 330$ nm the calculated external phase-matching angles for fused silica and CaF_2 are $\theta_{\mathrm{pm}} = 3.7°$ and $\theta_{\mathrm{pm}} = 3.2°$, respectively, which were kept fixed in the experiment. In order to minimize the group velocity mismatch and to maximize the physical pulse/beam overlap area, the amplitude front of the pump pulse was tilted by 4° by means of BK-7 glass prism with an apex angle of 70°, adjusted at the minimum deviation geometry. The respective lengths of the nonlinear bulk media samples ($l_{\mathrm{FS}} = 5$ mm and $l_{\mathrm{CaF_2}} = 6$ mm) were chosen to be longer than the shortest group-velocity mismatch length between the pump and signal pulses.

Experimental results

To start with, the maximum applicable pump energy and intensity, which remains safely below the optical damage threshold of the nonlinear media, was first considered. Since the intense elliptical pump beam experiences

strong self-focusing, its vertical FWHM dimension shrinks from 55 µm at the input to 25 µm at the output face of the nonlinear medium, while its horizontal dimension keeps approximately the same, as verified from beam profile measurements. Therefore the highest intensity is achieved and the optical damage tends to occur on the back surface of the nonlinear medium. In the experiment we have set the maximum pump energy of $E_p = 1$ mJ that converts to a maximum fluence of $F_p^{\max} = 0.75$ J/cm^2, which is still reasonably below the optical damage threshold fluence F_{th} for fused silica and CaF_2 samples, as listed in Table 2.2. The maximum intensity is then estimated as $I_p = 0.75$ TW/cm^2, assuming Gaussian spatial and temporal intensity distribution of the elliptical pump beam.

The four-wave optical parametric amplification experiment was performed by seeding a FWOPA by a narrow-band (FWHM width $\sim$ 1 nm) signal with an input energy $E_{s0} = 10$ µJ. The wavelength of the seed signal was tuned from 315 to 355 nm in 3 nm step, so as to scan precisely the gain profile of the FWOPA, while the beam crossing angle θ_{pm} and temporal delay between the seed and the pump pulses were kept fixed. The gain factor $G(\lambda)$ for a particular pump intensity and seed signal wavelength was evaluated according to equation:

$$\frac{E_s(\lambda)}{E_{s0}} = 1 + G(\lambda). \tag{2.1}$$

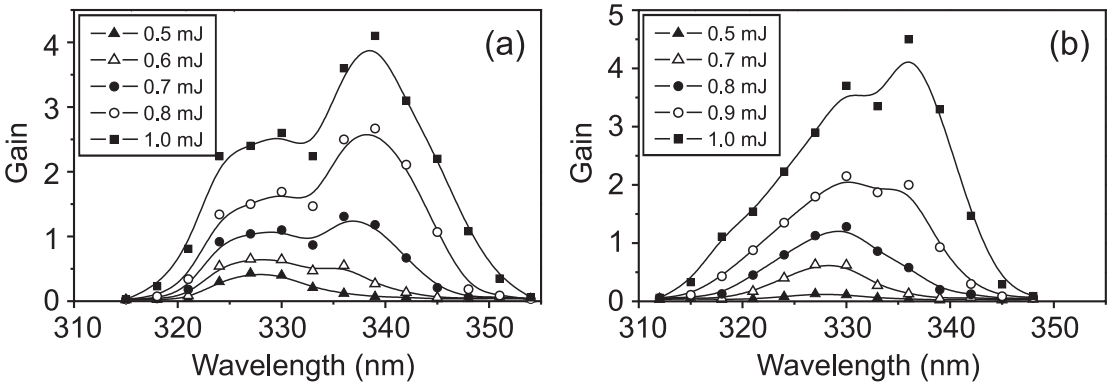

Figure 2.13: Measured four-wave parametric gain profiles *vs* pump energy in: (a) fused silica, (b) CaF_2.

The measured gain values at different wavelengths allowed to reconstruct in detail the four-wave parametric gain profile and its modifications as a function of pump energy (intensity). Figures 2.13(a) and (b) illustrate the four-wave parametric gain profiles measured in fused silica and CaF_2,

respectively, which reveal a number of interesting features. At low pump energy ($E_p = 0.5 - 0.6$ mJ), the four-wave optical parametric amplification in both media is characterized by a low gain ($G(\lambda) < 1$) and symmetric, nearly bell-shaped gain profiles with almost identical FWHM width of $\sim$ 10 nm centered at 327 nm. However, with increasing the pump energy, the gain profiles become notably broader and develop an asymmetric shoulder at longer wavelengths. With the highest applicable pump energy $E_p = 1$ mJ, the FWHM gain bandwidth broadens up to 21 and 17.5 nm in fused silica and CaF_2, respectively. It is important to mention that the measured ~ 20 nm gain bandwidth in the ultraviolet is broad enough to support the four-wave optical parametric amplification of light pulses as short as 7.5 fs (in the transform limit) in a solid state medium. With $E_p = 1$ mJ the highest amplified signal energy of 55 µJ was measured with almost 4% pump-to-signal energy conversion efficiency in the gain saturation regime. It is worth noting that the best amplification occurred at $\lambda_s = 340$ nm and $\lambda_s = 337$ nm in fused silica and CaF_2, respectively, rather than at $\lambda_s = 330$ nm, where the best phase matching according to Eq. (1.19) is expected. In order to analyze experimental findings we develop the analytical model, which extends the theory of the four-wave parametric amplification in condensed media of Penzkofer and Lehmeier [18].

Calculation of the parametric gain profiles

We investigate four-wave parametric amplification in a condensed medium with account for the self- and cross-phase modulation (SPM, XPM) experienced by the intense pump and weak signal and idler waves, respectively, in the plane and monochromatic wave approximation. The use of this approximation was justified according to the geometrical settings of the experiment, where the interacting beams in the phase-matching plane could be regarded as plane waves. The complex amplitude equations describing evolution of coupled waves along the propagation direction z with the account of SPM and XPM have the form:

$$\frac{\partial A_s}{\partial z} = -i\sigma_s A_p^2 A_i^* e^{-i\Delta kz} - i\sigma_s(|A_s|^2 + 2|A_i|^2 + 2|A_p|^2)A_s, \tag{2.2a}$$

$$\frac{\partial A_i}{\partial z} = -i\sigma_i A_p^2 A_s^* e^{-i\Delta kz} - i\sigma_i(2|A_s|^2 + |A_i|^2 + 2|A_p|^2)A_i, \tag{2.2b}$$

$$\frac{\partial A_p}{\partial z} = -i2\sigma_p A_s A_i A_p^* e^{i\Delta kz} - i\sigma_p(2|A_s|^2 + 2|A_i|^2 + |A_p|^2)A_p, \tag{2.2c}$$

where A_j $(j = s, i, p)$ are the complex amplitudes of the signal, idler and pump waves, respectively. We assume that the pump wave is composed of two collinear wave vectors k_p. The first terms on the right hand side of Eqs. 2.2 describe the four-wave parametric amplification (same as in Eqs. 1.12), while the second terms describe the SPM of the intense pump wave and the XPM experienced by weak signal and idler waves. In the undepleted pump approximation ($|A_p| \gg |A_i|, |A_s|$) Eq. (2.2c) reduces to

$$\frac{\partial A_p}{\partial z} = -i\sigma_p |A_p|^2 A_p \tag{2.3}$$

with only SPM term remaining and has a solution

$$A_p = A_{p0} e^{-i\sigma_p |A_{p0}|^2 z}, \tag{2.4}$$

where A_{p0} is the amplitude of the input pump wave. After inserting Eq. (2.4) into Eqs. (2.2a) and (2.2b), we obtain the following equations for the complex amplitudes of the signal and idler waves:

$$\frac{\partial A_s}{\partial z} = \sigma_s A_{p0}^2 e^{-2i\sigma_p |A_{p0}|^2 z - i\Delta k z} A_i^* - 2i\sigma_s |A_{p0}|^2 A_s, \tag{2.5a}$$

$$\frac{\partial A_i}{\partial z} = \sigma_i A_{p0}^2 e^{-2i\sigma_p |A_{p0}|^2 z - i\Delta k z} A_s^* - 2i\sigma_i |A_{p0}|^2 A_i. \tag{2.5b}$$

Further we assume that the nonlinear medium is lossless, hence the amplitude of the pump wave A_{p0} is real. Eqs. (2.5a) and (2.5b) could be further rewritten introducing parameters $\alpha_j = \sigma_j A_{p0}^2$ and $\beta_j = -2\sigma_j A_{p0}^2 = -2\alpha_j$ $(j = s, i, p)$:

$$\frac{\partial A_s}{\partial z} = \alpha_s e^{i(\beta_p - \Delta k)z} A_i^* + i\beta_s A_s, \tag{2.6a}$$

$$\frac{\partial A_i}{\partial z} = \alpha_i e^{i(\beta_p - \Delta k)z} A_s^* + i\beta_i A_i. \tag{2.6b}$$

Here we still distinguish between the coefficients α_j and β_j, since they describe relevant physical effects: four-wave parametric amplification, and self- and cross-phase modulation, respectively. Their impact could be understood as follows: SPM of the intense pump wave causes the occurrence of the phase mismatch ($\beta_p \neq 0$) in the first term on the right hand side, while the XPM introduces an additional phase shift in the second term ($\beta_{s,i} \neq 0$) on the right hand side. With boundary conditions for input wave amplitudes $A_{s0} \neq 0$ and $A_{i0} = 0$, that is only the seed signal wave is present at the amplifier input, the solution of Eqs. 2.6 for the amplified signal amplitude has a form

$$A_s = \Big(A_{s0} \cosh(gz) + \frac{i(\beta_s - \kappa) A_{s0}}{g} \sinh(gz)\Big) e^{i\kappa z} \tag{2.7}$$

where $\kappa = \frac{1}{2}(\beta_s - \beta_i + \beta_p - \Delta k)$ is the nonlinear wave number shift. g is the gain increment expressed as

$$g = \sqrt{[\alpha_s\alpha_i - \beta_s\beta_i + \beta_s(\beta_p - \Delta k)] - \kappa^2}. \tag{2.8}$$

If we neglect SPM and XPM terms by setting $\beta_s = \beta_i = \beta_p = 0$, Eq. (2.8) reduces to the known result obtained by Penzkofer and Lehmeier [18]:

$$g = \sqrt{\alpha_s\alpha_i - \left(\frac{\Delta k}{2}\right)^2}. \tag{2.9}$$

In what follows, using Eqs. (2.7) and (2.8) we calculate the four-wave parametric gain profiles in fused silica. The relevant parameters in the calculation were chosen as follows: the pump intensity and the seed signal wavelength were varied in the range corresponding to that used in the experiment, the nonlinear medium length was set as $z = l_{\mathrm{FS}} = 5$ mm and the pump intensity range in the simulation was set so as to achieve the gain values to be in the order of those measured experimentally. The four-wave parametric gain profiles were calculated using $\Delta k_0 \approx 3$ cm^{-1}, which refers to the central wavelength ($\lambda_s = 330$ nm). The value of Δk_0 was evaluated from the phase matching condition, with the account of wave vector length modification due to nonlinear refractive index:

$$\begin{aligned} k_s &= \frac{\omega_s}{c}(n_0(\omega_s) + 2n_2 I_p), \\ k_i &= \frac{\omega_i}{c}(n_0(\omega_i) + 2n_2 I_p), \\ k_p &= \frac{\omega_p}{c}(n_0(\omega_p) + n_2 I_p), \end{aligned} \tag{2.10}$$

where the pump intensity is defined as $I_p = \frac{cn_0(\omega_p)\epsilon_0}{2}|A_{p0}|^2$.

The results are depicted in Fig. 2.14(a) and qualitatively reproduce the experimental data presented in Fig. 2.14(b). The experimental data is in fair agreement with the calculations, although the range of experimental intensity values (450–750 GW/cm^2) is higher than that used in the calculations (80–160 GW/cm^2). This difference could be in part attributed to the spatial and temporal dynamics of the pump beam during its propagation within the nonlinear medium, and this was not taken into account in the analytical model. For the comparison the gain profile was calculated using Eqs. (2.7) and (2.9), without an account for the effects of SPM and XPM, and which thus represents the four-wave parametric gain profile in the low intensity limit. The marked differences between the calculated gain profiles

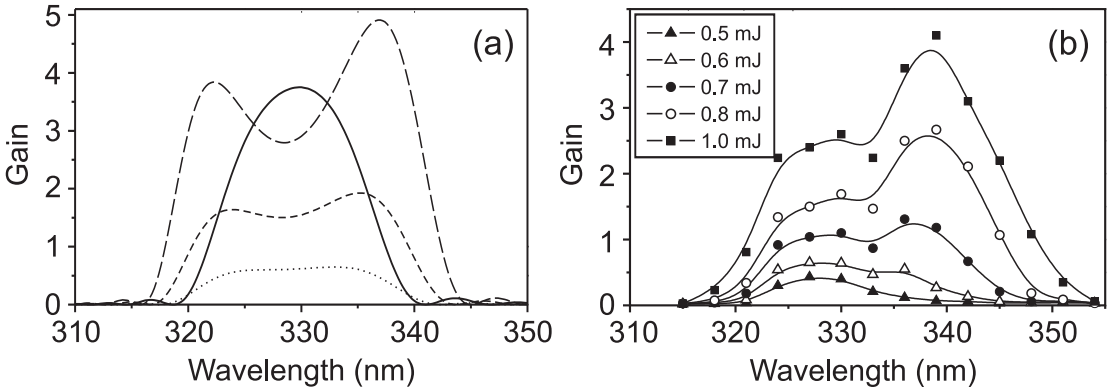

Figure 2.14: (a) Calculated four-wave parametric gain profiles in fused silica for three different pump intensities with $\Delta k_0 = 3$ cm^{-1}: dotted curve – $I_p = 80$ GW/cm^2, short-dash curve – $I_p = 120$ GW/cm^2, long-dash curve – $I_p = 160$ GW/cm^2. The solid curve shows the gain profile calculated without an account for the self- and cross-phase modulation effects. (b) Measured four-wave parametric gain profiles *vs* pump energy in fused silica.

in the low and high intensity limits suggest that the four-wave parametric gain bandwidth broadening is resulted by the SPM and XPM, whose contribution increases with increasing pump intensity. In order to illustrate this dependence in more detail, in Fig. 2.15 the argument gz versus signal wavelength calculated for three different values of the phase mismatch Δk_0 and taking $I_p = 160$ GW/cm^2 is plotted. The plot shows that

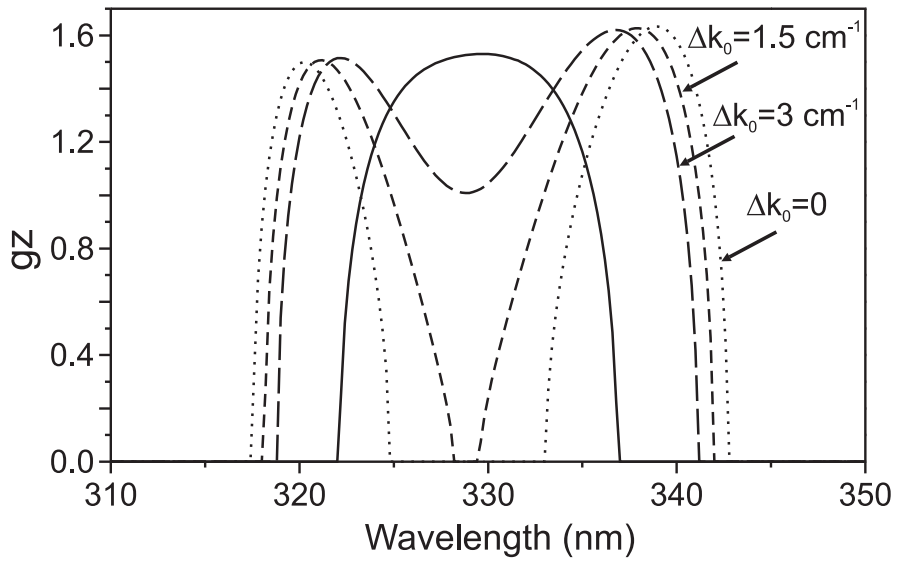

Figure 2.15: Argument gz versus wavelength, calculated in the low-intensity limit at $\Delta k_0 = 0$ (solid curve), and in the high-intensity limit at $I_p = 160$ GW/cm^2 for various values of phase mismatch: $\Delta k_0 = 0$ (dotted curve), $\Delta k_0 = 1.5$ cm^{-1} (short-dash curve) and $\Delta k_0 = 3$ cm^{-1} (long-dash curve).

a better phase-matching and consequently a higher gain is achieved for the

frequency-shifted, rather than for the central frequency components of the signal wave and thus results in a distinct dip in the gain profile. The depth of the dip could be varied by setting a particular Δk_0. The phase mismatch in the experiment could be varied by adjusting the crossing angle between the pump and signal beams. This result suggests that varying the beam crossing angle is an additional parameter that could be used to shape the four-wave parametric gain profile. For the comparison, in the low intensity limit the argument gz peaks exactly at the central wavelength $\lambda_s = 330$ nm (see Fig. 2.15).

In conclusion, a phase-matched four-wave optical parametric amplification of the ultraviolet 1-ps laser pulses in bulk fused silica and CaF_2 was demonstrated. The cylindrical focusing geometry allowed to use pump pulses with energy up to 1-mJ without beam filamentation and optical damage of the nonlinear medium. Under these experimental settings, FWOPA provides the amplified signal energy as high as 55 µJ with almost 4% pump-to-signal energy conversion efficiency for the signal wavelengths around 330 nm. In this wavelength range, FWOPA is able to support a broad amplification bandwidth ($\sim$ 20 nm FWHM), as demonstrated experimentally and verified by calculations in the framework of developed analytical model. In particular, the calculations reveal that two-fold parametric gain bandwidth broadening is resulted by self- and cross-phase-modulation effects imposed by the intense pump wave, and whose contribution increases with increasing pump intensity. This result could be of particular practical interest since it demonstrates a potential to amplify sub-10 fs ultraviolet light pulses in a bulk solid state medium.

2.3.2 Four-wave optical parametric chirped pulse amplification

The idea of the experiment is essentially similar to that of a small-scale OPCPA [81]: the visible pulses delivered by a commercial NOPA are chirped and stretched, and then amplified in transparent isotropic medium by the four-wave mixing (FWM) process: $\omega_p + \omega_p = \omega_s + \omega_i$, where indexes p, s and i denote pump, signal and idler waves, respectively. The idler pulses at frequency ω_i are generated in the UV spectral range: note here, that ω_i is the highest frequency in the FWM process. The idler pulses acquire

an opposite chirp as compared to that of the seed signal, and therefore are compressed by the propagation in a medium with normal group velocity dispersion. The major benefit of the proposed approach is that instead of conventional frequency upconversion of the NOPA output, FWM allows conversion of the visible pulses into the UV and amplification at the same time.

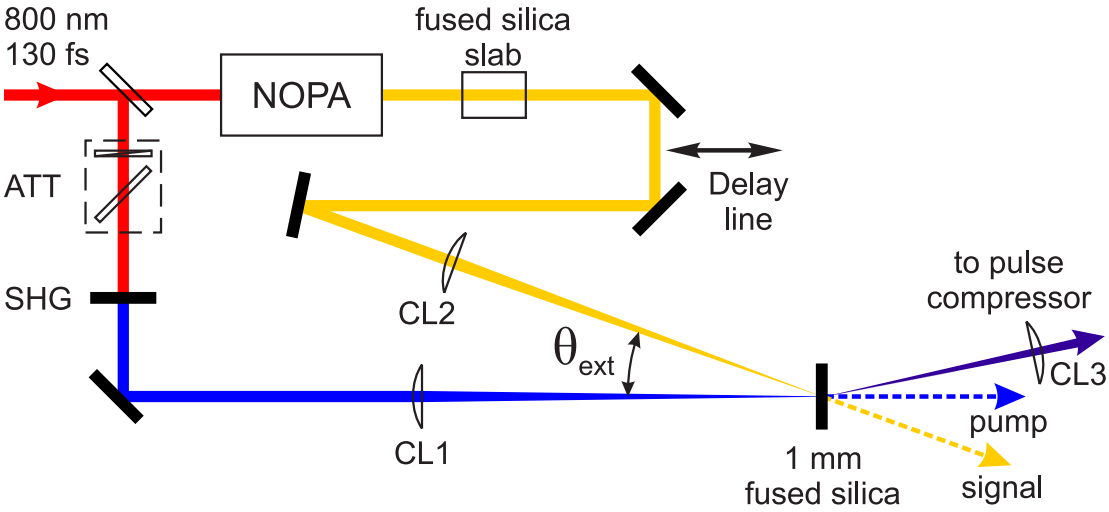

Figure 2.16: Experimental setup. NOPA is the noncollinear optical parametric amplifier, SHG is the second harmonic generator, ATT is the attenuator, CL1, CL2 and CL3 are the cylindrical lenses used for beam manipulation. θ_{ext} denotes the external phase matching angle, $\theta_{\text{ext}} \approx n(\omega_s)\theta_{\text{pm}}$.

The experimental setup is sketched in Fig. 2.16. In the experiment we used a Ti:sapphire laser system consisting of an oscillator (Tsunami, Spectra Physics) and a regenerative amplifier (Spitfire PRO, Spectra Physics). The laser system delivered 130 fs, 3 mJ pulses with central wavelength of 800 nm at 1 kHz repetition rate. The laser output was split into two parts. The first part (0.5 mJ/pulse) was used to pump a commercial three-wave NOPA (Topas White, Light Conversion Ltd., see Appendix I for more details), which was tuned to deliver 35 fs, 5 µJ signal pulses with central wavelength of 560 nm. These pulses were chirped and temporally stretched from 35 fs to 80 fs after propagation in fused silica slab and focusing optics, with total length of 15 mm, and served as a seed for the four-wave optical parametric amplifier. The second part of the laser radiation (2.5 mJ/pulse) was attenuated and made variable in energy by means of the attenuator ($\lambda/2$ plate and thin film polarizer) and, after frequency doubling in 0.2-mm-thick BBO crystal cut for type I phase-matching with 40% energy conversion efficiency, served as a pump pulse for the four-wave optical parametric ampli-

fier. Figure 2.17 shows the third-order autocorrelation traces of the pump and seed signal pulses, as measured by scanning autocorrelator, which used self-diffraction in 0.6 mm thick fused silica sample.

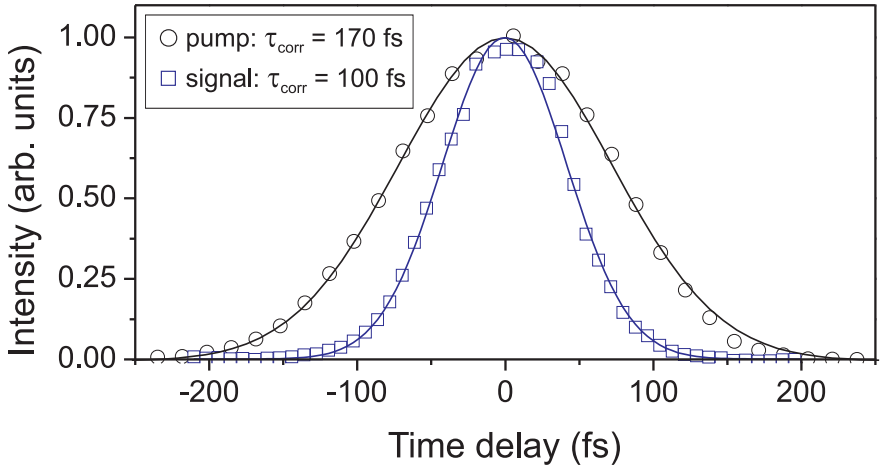

Figure 2.17: Third-order intensity autocorrelation traces of the pump (circles) and seed signal (squares) pulses. The FWHM pulse duration was estimated as $\tau = \tau_{\mathrm{corr}}/1.22$ assuming Gaussian pulse shape, which is indicated by a Gaussian fit (curves).

The temporal delay between co-polarized pump and seed signal pulses was adjusted using a delay line. The pump and seed signal beams were focused using identical cylindrical lenses CL1 and CL2 (f_x=+500 mm; f_y=∞). Cylindrical focusing geometry allowed to perform four-wave parametric amplification reasonably below the optical damage threshold even with millijoule-level pump energies. The spot sizes (defined at FWHM) of the seed signal and the pump beams on the input face of the amplifying medium were measured as 1.5 mm×45 µm and 1.5 mm×60 µm, respectively. As an amplifying medium we used 1-mm-thick fused silica plate. Our choice of the nonlinear medium was dictated by its wide transparency range, high optical damage threshold and low nonlinear absorption for the wavelengths of interest. The plate thickness was set to be slightly shorter than the group velocity mismatch length between the pump and signal pulses ($L_{\mathrm{GVM}} = 1.25$ mm), which was calculated with account for noncollinear interaction geometry.

The phase matching curve for fused silica, calculated for plane and monochromatic waves, is depicted in Fig. 2.18, and the diagram of the interacting wave vectors is shown in the inset. Geometrically, the beams were crossed in the horizontal plane at the phase matching angle $\theta_{\mathrm{pm}} = 6.8°$; at the same plane the cylindrical beam focusing was performed, so as to in-

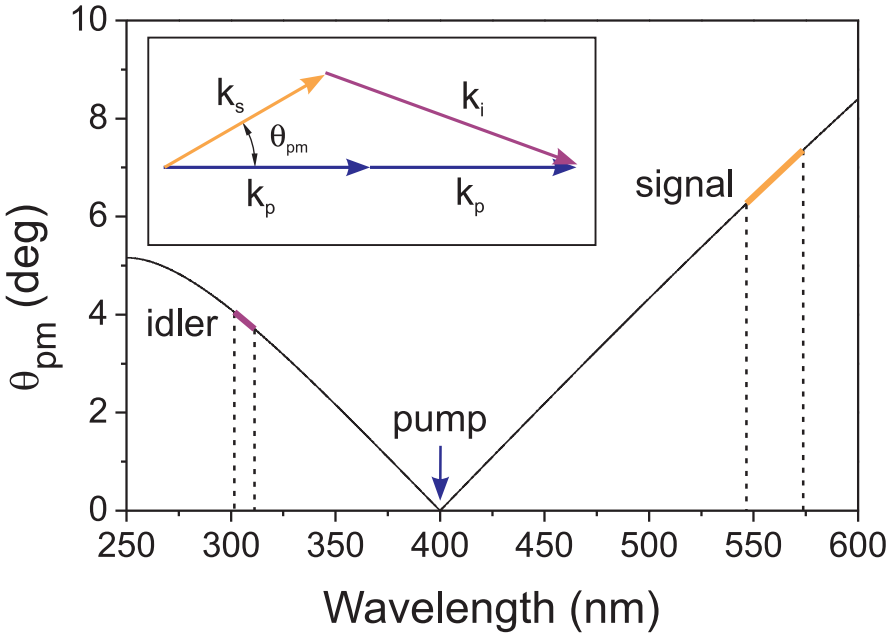

Figure 2.18: Phase matching curve for the four wave optical parametric amplification in fused silica pumped with $\lambda_p = 400$ nm. Wavelength ranges for broadband signal and idler pulses (spectral width at FWHM) are bolded and indicated by dashed lines. The inset shows the wave vector diagram.

crease the angular spread of the interacting beams and therefore to increase the angular acceptance and phase-matching bandwidth.

In the experiment, energy of the pump pulse was varied up to 0.5 mJ, that yielded maximum focused beam intensity of $I_{\max} = 5$ TW/cm^2 and fluence of $F_{\max} = 0.6$ J/cm^2, which was two times below the optical damage threshold of fused silica at 400 nm ($F_{\text{th}} = 1.3$ J/cm^2 [82]). At this condition, the highest generated idler pulse energy of $E_{\text{idler}} = 10$ µJ was measured, suggesting 2% pump-to-idler energy conversion efficiency in the gain saturation regime. The obtained energy conversion is quite typical, as compared to that achieved in non-resonant four-wave mixing processes. In our case it was limited mainly by the self-phase modulation of intense pump pulse (the pump pulse spectrum has broadened from 2.5 nm to 4 nm, as estimated at FWHM), which incurs a time-varying phase mismatch [18]. On the other hand, it is worth mentioning that the energy conversion could still be improved by increasing the seed signal energy and approaching four-wave difference frequency generation regime as described in Sect. 2.2.

Spectra of the seed signal, amplified signal and the generated idler pulses are plotted in Fig. 2.19. During the four-wave amplification process, the seed signal was amplified by a factor of ~ 2, its spectrum has broadened

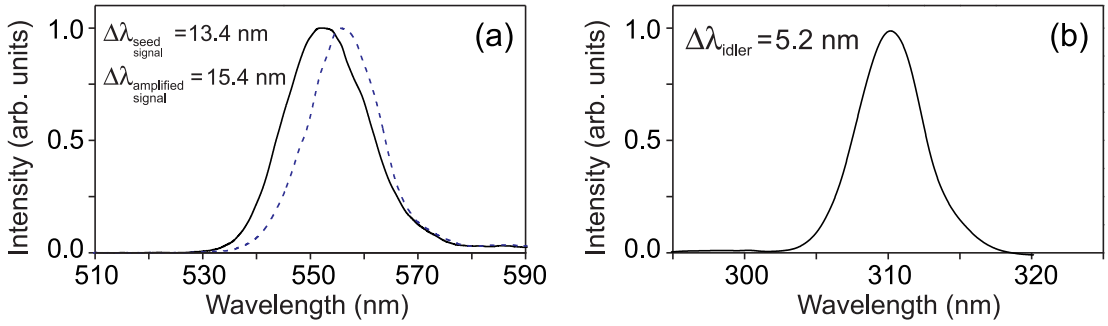

Figure 2.19: Spectra of: (a) seed signal pulse (dashed curve) and amplified signal pulse (solid curve), (b) idler pulse.

from 13.4 nm to 15.4 nm (measured at FWHM), and its central wavelength was slightly shifted towards shorter wavelengths [Fig. 2.19(a)] due to the cross-phase modulation effect induced by the intense pump pulse. Spectrum of the idler pulse at 310 nm is illustrated in Fig. 2.19(b) and has FWHM width of 5.2 nm, which suggests the transform-limited pulse duration of 27 fs.

Assuming that the seed signal pulse has a positive chirp (the red-shifted leading edge and the blue-shifted trailing edge) and the pump pulse is weakly positively chirped as a result of the self-phase modulation, the generated idler pulse has a negative chirp, therefore it could be compressed simply by passing through the medium with normal group velocity dispersion. With GVD coefficient of 146 fs^2/mm for fused silica at 310 nm, we estimate that 3-mm-thick fused silica plate is sufficient to compress the idler pulse. 3 mm is exactly the thickness of the beam-reshaping lens CL3, which restores spherical symmetry of the beam (see Fig. 2.16), hence we expect a fully compressed pulse at the output of our setup. However, the autocorrelator optics (it uses spherical 3-mm-thick fused silica lens for beam focusing) introduces additional amount of the positive dispersion, therefore to optimize the compression of the idler pulse, we used a sequence of two fused silica prisms with 70° apex angle in a double-pass configuration.

Figure 2.20(a) shows the measured idler pulse duration versus the distance between prisms. The curve serves as a guide for the eye. We note that under our experimental settings (with beam focusing in the phase-matching plane, and assuming the spectral width of the pump pulse) the idler pulse-front tilt, which might be deduced from Fig. 2.18, was barely detectable and has not altered the results of the correlation measurements. At the optimal compressor length, the shortest pulse of 33 fs was measured,

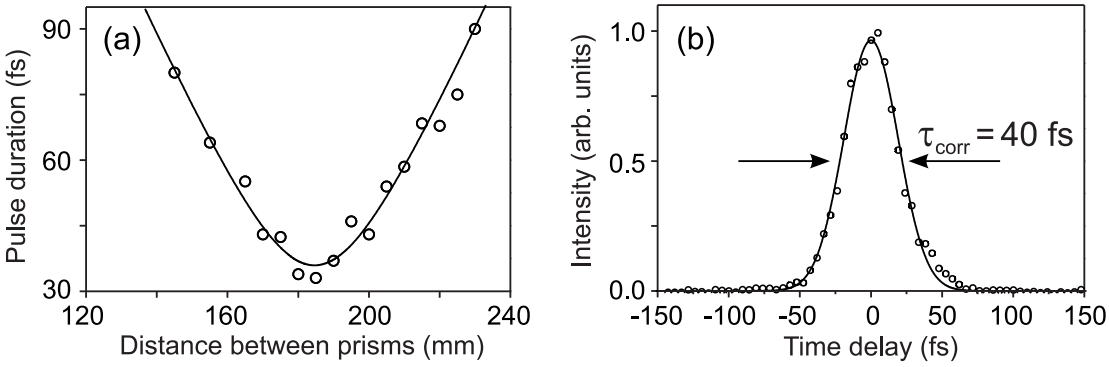

Figure 2.20: (a) FWHM duration of the idler pulse versus distance between the prisms. (b) third-order autocorrelation trace of 33-fs idler pulse, measured at the best compression point. Curve shows a Gaussian fit.

and its third-order autocorrelation trace is presented in Fig. 2.20(b). We note that the compressed idler pulse quality is reasonably high: its temporal profile is smooth, its shape is almost perfectly Gaussian, as indicated by the Gaussian fit, and its width is just ≈ 1.2 times from the transform limit.

In conclusion, we have proposed and demonstrated visible-to-ultraviolet frequency conversion method based on chirped-pulse four-wave optical parametric amplification in fused silica, which produces ~ 30 fs, ~ 10 µJ pulses in the UV spectral range. The advantage of our scheme is reasonable overall energy conversion from the laser output to the UV, and simplicity and compactness of the setup. The proposed approach may be easily extended in the tuning range of 275–320 nm, which is ensured by the tuning range of the NOPA signal (530–720 nm, see Appendix I for more details). Moreover, the phase matching conditions for the four-wave interaction could be fulfilled in the VUV spectral range, using shorter pump wavelength, which might facilitate generation of tunable femtosecond pulses by four-wave difference frequency mixing in transparent wide-bandgap solids, such as MgF_2 as demonstrated in Sect. 2.2.3 with picosecond pulses.

Chapter 3

Few optical cycle pulse generation by visible-to-infrared frequency conversion

Material related to this chapter was published in [A7 – A11]

3.1 Motivation

At present, there is a growing demand for energetic, few-optical cycle pulses in the NIR and MIR in connection with ultrafast spectroscopy [1–3] and rapidly evolving discipline of strong field physics and attosecond science [83]. In the pursuit of this goal, various approaches and strategies enabling efficient generation of ultrashort pulses in the IR spectral range have been proposed. A straightforward route to generate few optical-cycle pulses in the IR is to pump an OPA with extremely short pulses, obtained, e. g. by employing hollow-fiber compression technique [84], which however, imposes severe limitations on the available pump energy. Another approach considers the use of broadband phase matching that is readily achievable in a collinear interaction geometry at the degeneracy, at the cost of wavelength tunability [85]. More flexible methods utilize the noncollinear optical parametric amplification technique in nonlinear crystals, which provide suitable group velocity relations in the IR, see [86] for a review and recent developments in the field. The noncollinear infrared optical parametric amplifiers commonly employ the infrared part of the supercontinuum as a seed signal, whose low spectral energy density imposes certain practical difficulties, such as high level of the amplified parametric superfluorescence. Frequency down-shifting (i.e. difference frequency generation) of already pre-formed

seed pulse proves to be more energetically efficient and is demonstrated in a number of experimental configurations, which use various transparent media with quadratic and cubic nonlinearity [29, 30, 44, 87]. High power and high repetition rate OPCPA technique-based systems, which combine either optical parametric amplification and/or difference frequency generation with nonlinear propagation (hollow-fibre or filamentation) techniques at present yield high energy (tens-of-mJ), high peak-power (sub-100-GW) few-optical cycle pulses whose wavelength is now shifted into the MIR [27, 88–91].

The existing alternatives for ultrashort pulse generation in the IR spectral range suggest optical parametric amplification in gases by means of four-wave parametric processes in the filamentation [29] and guided-wave propagation regimes [30] taking an advantage of intrinsically low group velocity dispersion of gaseous media and small group velocity mismatch between the signal and idler pulses. The latter guarantees broad amplification bandwidth that combined with nonlinear propagation effects is able of supporting generation of IR pulses close to a single optical cycle limit [31]. Another approach considers IR generation in wide bandgap solids, which possess much higher third-order nonlinearity than gases as discussed in Chapter 2.

In this Chapter we experimentally demonstrate visible-to-infrared frequency conversion of the ultrashort light pulses for extension of the tuning range of a commercial Ti:sapphire laser-NOPA system. The first setup presented in Sect. 3.2 relies on four-wave parametric amplification, supporting ultrashort pulses in the NIR ($1-1.5$ µm) spectral range. In Sect. 3.3 a different approach based on three-wave mixing in BBO crystals is presented. The latter method rely on collinear difference frequency generation and subsequent optical parametric amplification.

3.2 Visible-to-infrared frequency conversion via four-wave interactions

The results presented in this section refer to a single-pass four-wave optical parametric amplification in fused silica, pumped at 800 nm and seeded by broadband visible pulses. The experimental setup is depicted in Fig. 3.1. The laser beam at the fundamental frequency was divided by 30% beam splitter BS into two parts: one part (with energy variable up to 1.8 mJ)

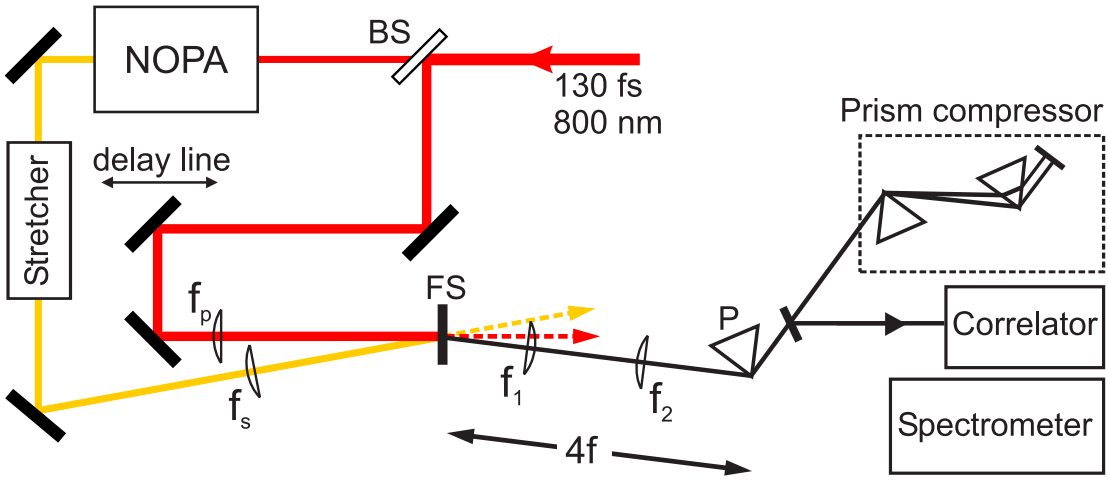

Figure 3.1: Experimental setup for four-wave optical parametric amplification: BS is the beam splitter, FS is the fused silica plate, P is the pulse-front tilt compensating prism, f_p and f_s are the focusing and f_1 and f_2 are the imaging lenses, respectively.

served as a pump for the FWOPA, while the second part (with energy 0.5 mJ) pumped a NOPA device, which provided a broadband seed signal with a duration of 30 fs and which was tuned in the visible wavelength range (550-650 nm). The seed signal pulse was additionally stretched from 30 to 50 fs by passing through 7-mm-long slab of silica glass, denoted as a pulse stretcher in Fig. 3.1, hence acquiring a positive chirp. The pump and seed signal beams of the same linear polarization were noncollinearly overlapped at the phase-matching angle inside the 1-mm-long fused-silica sample (FS). The pump and seed signal beams were focused with spherical lenses, $f_p = 800$ mm and $f_s = 500$ mm, respectively, that yielded respective FWHM beam dimensions of 0.8 and 0.33 mm at the input facet of the fused silica sample, ensuring a good spatial overlap of the interacting waves along the sample length. The phase-matching angle between the pump and signal beams, which supports efficient four-wave parametric interaction ($\omega_p + \omega_p = \omega_s + \omega_i$), was calculated according to Eq. 1.19, while the angle between the pump and emerging idler wave was found from Eq. 1.20.

The phase-matching curve in fused silica is depicted in Fig. 3.2(a), showing that phase-matching angles for a visible seed signal vary between 1.5 and 2.1 degrees, whereas those for the idler (NIR) pulses vary in the range of $2.2 - 5.5°$. Fig. 3.2(b) shows typical spectra of the amplified signal and generated NIR pulses. With a NOPA signal tuning range of 550-650 nm, the generated NIR idler pulses cover wavelength range from 1.0 to 1.5 µm. The NIR pulse spectrum was recorded by a fiber spectrometer (QE65000,

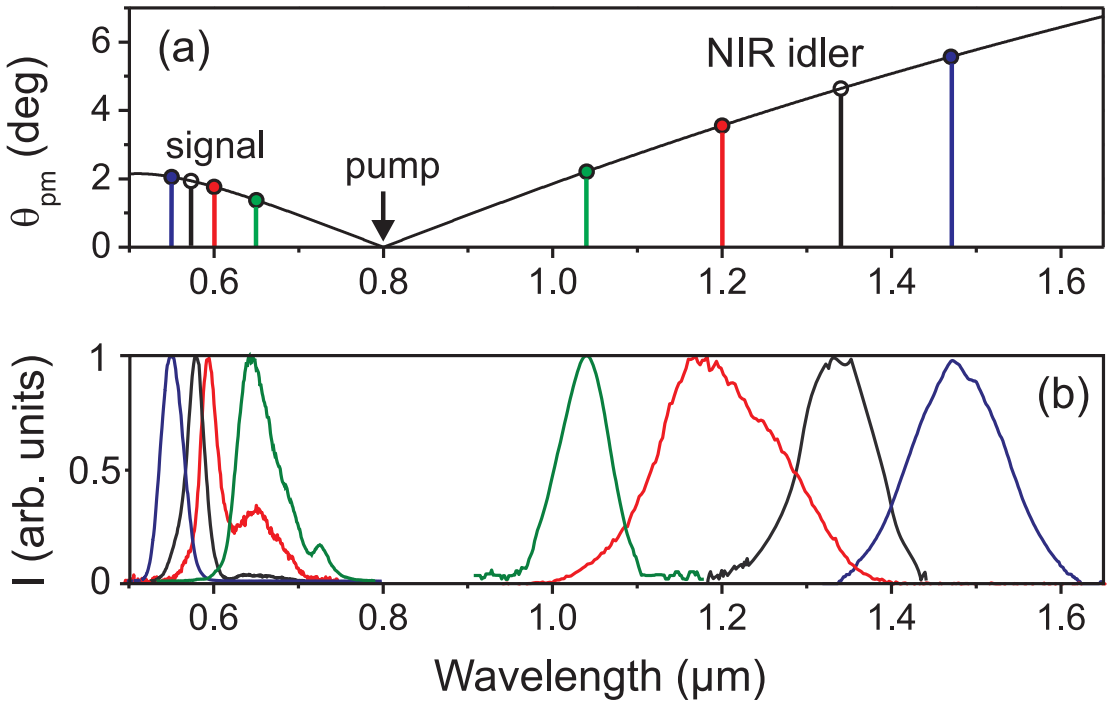

Figure 3.2: (a) Phase-matching curve in fused silica. (b) Spectra of the amplified signal and generated NIR (idler) pulses.

Ocean Optics) after the frequency doubling in thin, 20-μm BBO crystal that ensured broadband frequency conversion from IR to visible so as to fit the detection range of the spectrometer. The measured spectral FWHM width of the NIR pulses varied from 70 to 140 nm, supporting short, sub-30-fs pulse duration throughout the whole tuning range and even sub-20-fs duration for the NIR pulse centered at 1.2 μm, where NOPA provides the broadest spectra.

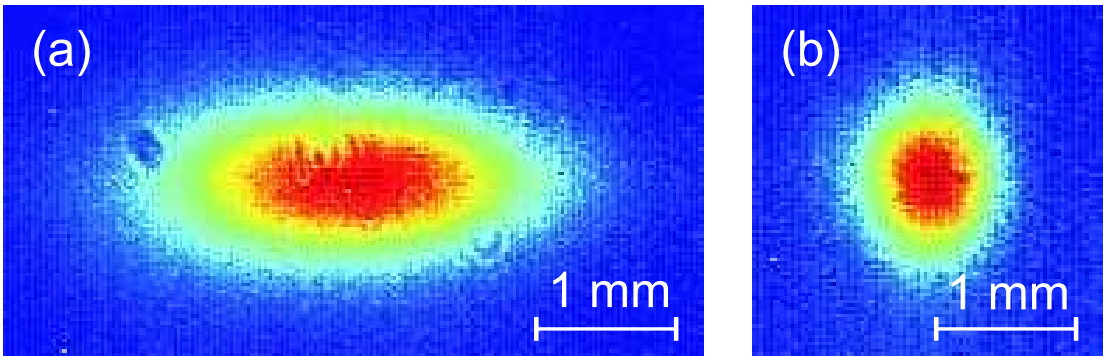

Figure 3.3: Far-field intensity profiles of the NIR beam (at 1.34 μm): (a) before and (b) after pulse-front tilt removal.

Due to noncollinear interaction geometry, the generated broadband NIR pulse possessed a pulse-front tilt, which manifested itself as apparent an-

gular dispersion of the beam in the phase-matching plane, that is clearly visible as elongated far-field intensity profile of the NIR beam, as shown in Fig. 3.3(a). The pulse-front tilt was fairly constant along the whole tuning range as a result of the constant slope of the phase-matching curve. The tilt value was evaluated as $\delta = \arctan(\lambda\ d\theta/d\lambda) \approx 9.9°$. The pulse-front tilt was removed by imaging the NIR pulse with a beam-size magnifying telescope consisting of $f_1 = 125$ mm and $f_2 = 300$ mm lenses, arranged in $4f$ geometry, onto a single TF10 glass prism (P) with a 60° apex angle. Figure 3.3 compares the far-field intensity profiles of the NIR beam before and after tilt removal, as recorded by InGaAs complementary metal oxide semiconductor (CMOS) camera (Xenics, Xeva 202). After the tilt removal, the pulse was compressed in a double-pass prism-pair compressor that consisted of two identical 60° apex angle TF5 glass prisms aligned at the angle of minimum deviation.

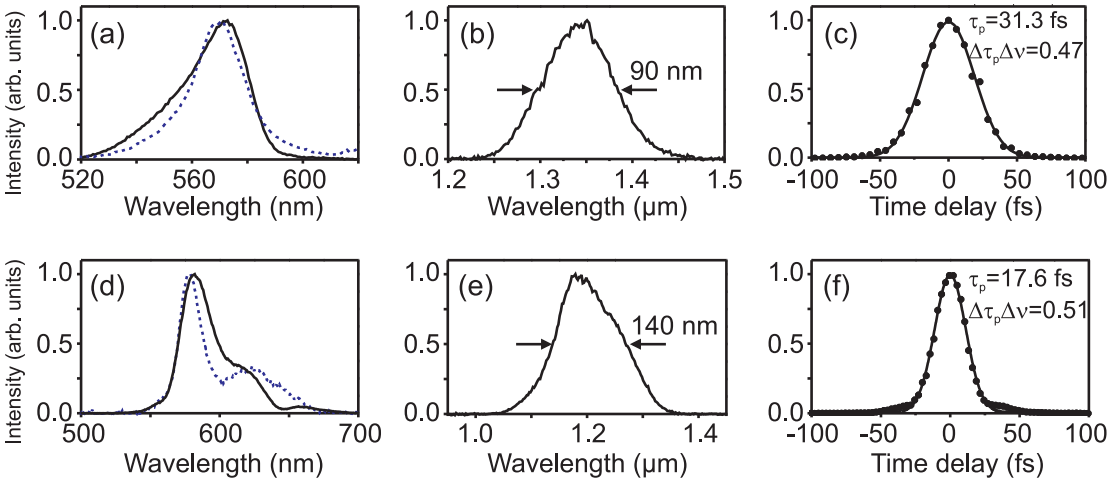

Figure 3.4: Pulse characteristics at the FWOPA output at 1.34 µm and 1.20 µm. (a), (d) spectra of the seed (dashed curves) and amplified signal (solid curves) in the visible; (b), (e) spectra of the NIR pulses; (c), (f) autocorrelation traces of compressed NIR pulses. Here solid curves show the Gaussian fit.

Figure 3.4 illustrates the relevant characteristics of the FWOPA operation at two wavelengths, 1.34 µm and 1.20 µm. The left panel [Fig. 3.4 (a) and (d)] compares spectra of the seed and amplified signal in the visible range. The center panel [Fig. 3.4 (b) and (e)] illustrates spectra of the frequency down-converted NIR pulses at the FWOPA output. The right panel [Fig. 3.4 (c) and (f)] shows the autocorrelation functions of the compressed NIR pulses as measured by a scanning autocorrelator, which uses 20 µm thick type I BBO crystal, with a phase matching bandwidth of 2000 nm

and 4800 nm for 1.2 µm and 1.34 µm wavelengths respectively (calculated as $\delta\lambda_{\mathrm{FWHM}} = \frac{0.44\lambda_0/L}{\left|n'(\lambda_0)-\frac{1}{2}n'(\lambda_0/2)\right|}$, where λ_0 is the pulse central wavelength, L is the crystal length and $n'(\lambda) = \mathrm{d}n/\mathrm{d}\lambda$). The estimated time-bandwidth product $\Delta\tau_p\Delta\nu \approx 0.5$ at both wavelengths indicates that the NIR pulses are well compressible to almost bandwidth limit. In fact, the time-bandwidth product of the NIR pulses was fairly constant across the entire tuning range ($1-1.5$ µm). The shortest NIR pulse of 17.6 fs duration that equates to 4.4 optical cycles, was measured at 1.2 µm, as shown in Fig. 3.4 (f). We note that the broad bandwidth at 1.2 µm and the resulting shorter pulse duration at this particular wavelength are the result of the broader bandwidth seed pulse at 600 nm generated by the NOPA. This therefore shows that the solid-state FWOPA may support very large bandwidths.

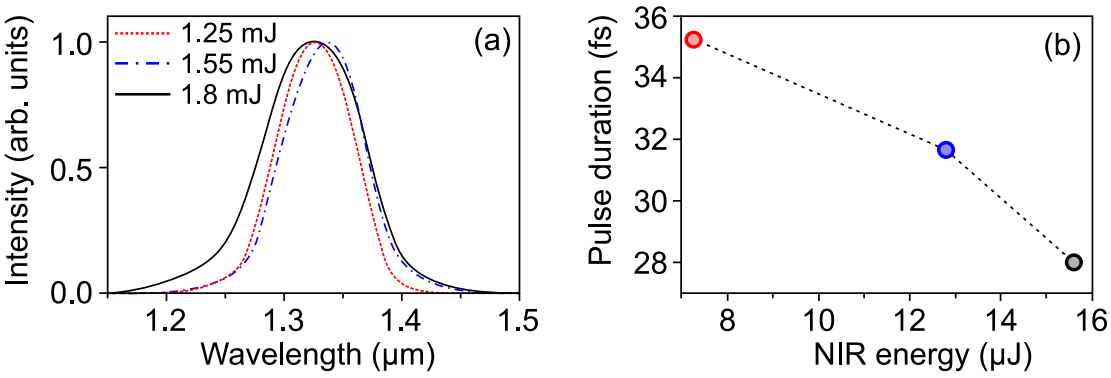

Figure 3.5: NIR pulse spectra (a) and durations *vs* NIR energy at 1.34 µm (b) for three different pump energies, namely, 1.25 (red dashed), 1.55 (blue dash-dotted), and 1.8 mJ (black solid).

We also observed that an increase of the pump energy leads to a spectral broadening of the NIR pulse [Fig. 3.5(a)], as a result of the cross-phase modulation between the pump and seed pulses inside the fused silica sample, as described in Sect. 2.3.1 and noted in similar experiment [92]. We found that the XPM-broadened pulses are still fully compressible, and indeed, the measured pulse durations, after optimization of the pulse compressor, were shorter by $\sim 10-20\%$ (from 35 fs down to 28 fs at 1.25 and 1.8 mJ pump energies respectively [see Fig. 3.5(b)]). An example of the XPM-broadened pulse compression is illustrated in Fig. 3.6 that depicts temporal intensity and phase profiles of the compressed pulse at 1.34 µm generated with 1.8 mJ pump, as retrieved by SHG-FROG technique.

Using a seed signal energy of 4.8 µJ, which was kept fairly constant across the whole visible spectral range, and pump energy of 1.8 mJ, FWOPA

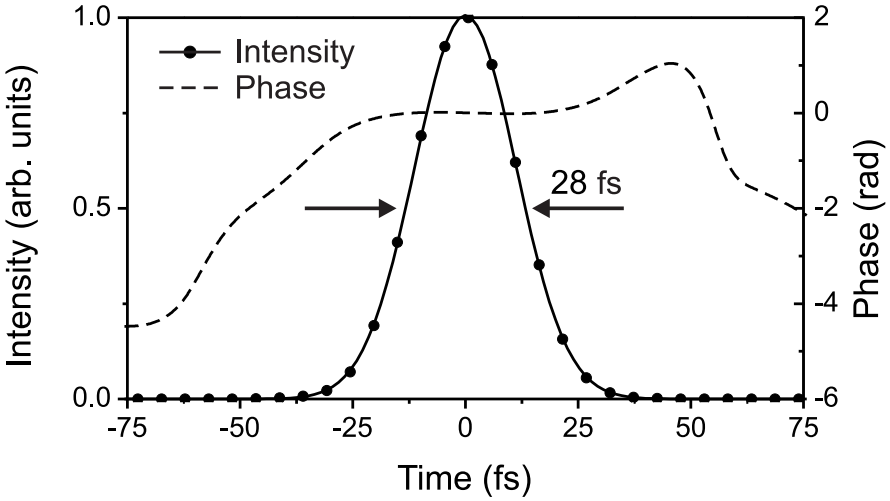

Figure 3.6: SHG-FROG characterization of the NIR pulse at 1.34 µm, showing retrieved temporal intensity (solid curve) and phase (dashed curve) profiles.

delivered sub-30-fs NIR pulses with energy up to 20 µJ across the whole $1-1.5$ µm wavelength range. Under these settings, 1% pump-to-idler conversion efficiency was achieved, which could be further increased by optimizing (increasing) the input seed energy and approaching four-wave difference frequency generation regime as described in Sect. 2.2.

In conclusion, in this section a proof-of-principle method for broadband frequency downconversion with a standard Ti:sapphire pumped visible NOPA was demonstrated, which can achieve up to 20 µJ, sub-30-fs pulses tunable in the 1 to 1.5 µm range. To the best of our knowledge, this is the first scheme based on isotropic solid-state medium (fused silica) that allows visible-to-IR conversion and provides both very large tunability and simultaneous broadband amplification, supporting few-optical-cycle pulses in the NIR ($1-1.5$ µm) spectral range. Moreover, it promises scaling to very high pump energy levels due to the availability of large aperture Kerr media and suitable conditions for frequency downconversion up to 10 µm, using materials with extremely broadband transparency range, such as CaF_2. The proposed FWOPA is competitive to frequency conversion schemes based on gaseous media and, despite lower energy conversion efficiency, provides very similar output characteristics to conventional three-wave parametric amplifiers based on birefringent crystals. The developed IR source might readily serve for diverse applications and might be considered as an energetic seed pulse with high spatial and temporal quality for front-end high-power IR laser systems [93].

3.3 Visible-to-infrared frequency conversion via three-wave interactions

The noncollinear geometry of the four-wave optical parametric amplification might be somewhat less technically attractive if fast wavelength tunability (scanning) is required, since wavelength tuning requires adjustment of the beam intersection angle so as to fulfill the phase matching condition, as seen from Fig. 3.2(a). In the following sections we demonstrate a different approach for generation of broadly tunable ultrashort IR pulses by means of three-wave parametric interactions in type I BBO crystals.

3.3.1 The general idea

In order to achieve few-cycle, high energy near infrared pulses with a three-wave OPA system, (i) a broadband seed and (ii) amplifier, that supports ultrashort pulses, are needed. Various concepts may be applied to meet the first requirement. In a classical single pass infrared OPA, that involve amplification of the IR part of the supercontinuum spectrum, ultrashort pulses can be generated at the degeneracy. Specifically, sub-10 fs pulses at 1.6 µm with $\sim$ 1 µJ energy were demonstrated [85, 86]. The tuning range could be extended up to $1.1 - 1.5$ µm, if a noncollinear geometry in a suitable nonlinear crystal is used [85, 94–97]. Another method suggests spectral broadening technique in a hollow fiber filled with krypton. In this case, few nJ energy pulses with ultrabroadband spectrum spanning from 1.7 µm to 2.6 µm are obtained by intra-pulse DFG between different components of the SC [89] (see also [88, 98, 99] for similar results). The latter approach, however is more energy demanding, the generated spectrum and spectral phase are not smooth, thus programmable pulse shaper is usually required for pulse compression. Other technique suggests DFG between two synchronized NOPAs, where spectrum spanning from 800 nm to 1700 nm can be achieved [44]. Typical pulse energy ranges from tens to hundreds of nanojoules when DFG approach is used and usually does not exceed 1 µJ in a single pass OPA configuration. For many applications, however, a much higher energy is needed, thus pulses are amplified in one or several OPA stages.

So far, OPA in the $1 - 3$ µm spectral range was demonstrated using different nonlinear crystals and interaction geometries. The shortest pulse

duration is usually achieved close to degeneracy, where the group velocities between signal and idler waves can be perfectly matched. In particular, few-cycle pulse amplification was demonstrated around 1.6 µm, when pumped by Ti:sapphire lasers (800 nm) [98]. In this configuration pulses as short as 9 fs [99] with energy up to 1.2 mJ [88] can be achieved. Also, several articles have been reported on the development of few-cycle OPAs operating at 2.1 µm, when pumped by Nd:YLF (1053 nm) [89] and Yb:YAG (1030 nm) [28] lasers. While it is hard to beat the previously mentioned OPAs in terms of pulse duration, their tuning range, however, is rather limited. Broad parametric gain bandwidth and wavelength tunability, on the other hand, can be achieved simultaneously, when OPA is pumped by an ultrashort pulses (e.g. 45 fs from Ti:sapphire regenerative amplifier) [100]. Using this configuration 50 fs pulses tunable in the $1.2 - 2.4$ µm spectral range were demonstrated [101]. In the following sections we focus on a slightly different approach, that allows generation of widely tunable, few-optical cycle pulses in the infrared spectral range.

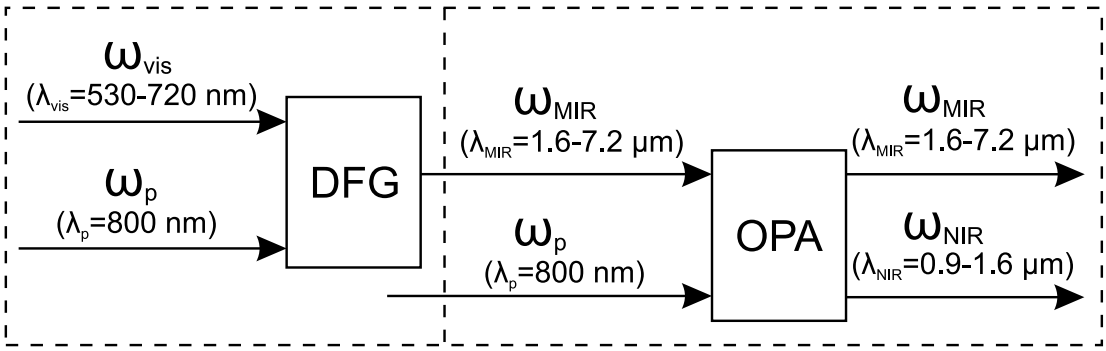

Figure 3.7: Schematic presentation of the visible-to-infrared frequency conversion method.

The general idea of the proposed method is schematically depicted in Fig. 3.7. Tunable IR pulses are obtained by means of two second-order parametric interactions: difference frequency generation and subsequent optical parametric amplification. The first step considers the DFG between broadband visible pulse delivered from NOPA, ω_{vis}, and narrowband Ti:sapphire fundamental harmonics pulse (center wavelength 800 nm, ω_p) thus producing the MIR pulse at $\omega_{\mathrm{MIR}} = \omega_{\mathrm{vis}} - \omega_p$. A big advantage of this concept is that no IR seed must be provided. One can benefit from using already well-established ultrashort visible light pulses, which are of excellent spatial and temporal quality and high energy. Since only a small parametric gain is needed in a DFG stage, a rather thin crystal in a collinear geometry can

be used, without severe limitation of the acceptance bandwidth. The second step is the optical parametric amplification of the difference-frequency (MIR) wave, which serves as a seed signal, and at the same time producing the NIR idler wave according to energy conservation: $\omega_p = \omega_{\mathrm{MIR}} + \omega_{\mathrm{NIR}}$. Note, that the OPA is seeded with a longer wavelength pulse, which is then called a signal pulse throughout the text. Specifically, by tuning wavelength of the visible pulse in the λ_{vis}=530–720 nm range, which is defined by the blue-pumped NOPA operational characteristics (see Appendix I for more details), the tunable MIR and NIR pulses that cover wavelength range of λ_{MIR}=1.6–7.2 µm and λ_{NIR}=0.9–1.6 µm, respectively, could be generated. The actual tuning range, however, will depend on the IR absorption properties of the particular nonlinear crystal used. For instance, using the BBO crystal, the tuning range is limited to wavelengths shorter than 3 µm, being set by the crystal absorption in the IR. Both DFG and OPA processes can occur simultaneously in a single BBO crystal as shown in Sect. 3.3.3, or can be realized in multiple crystals in collinear (Sect. 3.3.2) and noncollinear (Sect. 3.3.4) geometry. The proposed method can be extended to generate few optical cycle pulses in the mid-infrared spectral range (up to 6 µm) using, e.g., lithium iodate ($LiIO_3$) and lithium niobate ($LiNbO_3$) crystals, as demonstrated by the numerical simulations in Sect. 3.3.5.

3.3.2 Collinear BBO crystal-based optical parametric amplifier

In 2009 Zhang et al. [101] proposed a setup for an OPA, tunable in the $1.2-2.4$ µm spectral range. The way of operation is as follows: the white light continuumum is first amplified in a type I BBO crystal based NOPA, alongside the angularly dispersed idler in the $1.2-2.4$ µm range is generated. The hollow fiber is then used to improve the idler beam quality and to overcome the spatial chirp issue. Finally, these pulses are amplified up to $\sim$ 1 mJ in type II BBO crystal. The OPA output pulse duration of 50 fs is determined mainly by the pump pulse width (40 fs). In this section we present a setup with the same tuning range ($1.2-2.4$ µm), however shorter pulse duration (i.e. sub-30 fs) and sub-100 µJ energy.

Numerical simulations

As a starting point, we present the results of the numerical simulations, which illustrate the basic performance characteristics of the DFG and OPA stages. The numerical simulations were carried out by solving the three-wave parametric equations in the framework of plane wave approximation with account for group velocity mismatch, group velocity dispersion and third-order dispersion effects. The relevant parameters of the BBO crystal (nonlinearity, dispersion relation, transparency range, etc.) were taken from [102].

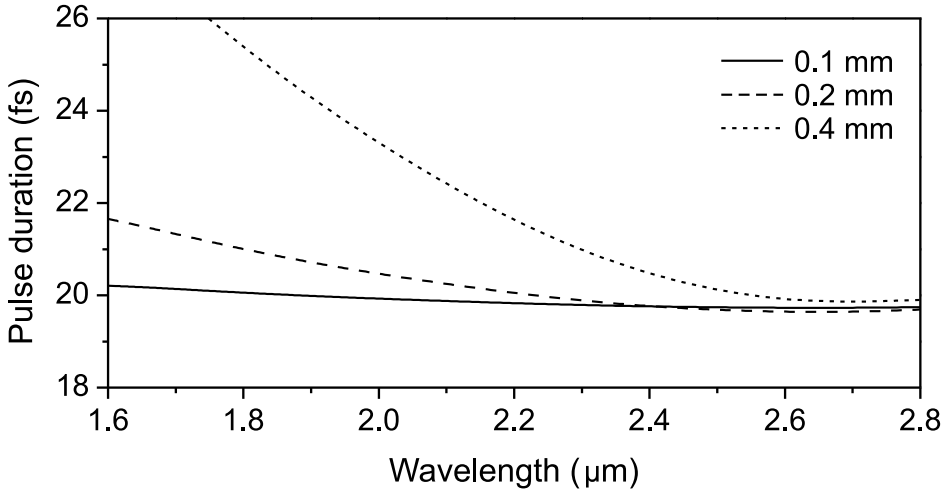

Figure 3.8: Computed FWHM width of the difference-frequency pulse generated in 0.1 mm (solid curve), 0.2 mm (dashed curve) and 0.4 mm (dotted curve) BBO crystals.

The DFG process was simulated using input Gaussian pulses with FWHM widths of $t_{\mathrm{vis}} = 20$ fs and $t_{\mathrm{p}} = 130$ fs, as those used in real experimental settings (see "Experimental results" for details). Note, that both input pulses are considered to be bandwidth limited, i.e. no temporal stretching and pulse chirping is applied. The most favorable conditions for collinear DFG in terms of acceptance bandwidth and conversion efficiency for wavelengths of interest occur in type I phase matching interaction. The FWHM width of the difference-frequency pulse versus wavelength as computed by numerical integration of coupled-wave equations for three different lengths (0.1, 0.2 and 0.4 mm) of the BBO crystal is depicted in Fig 3.8. The intensity of the input pulses ($I_{\mathrm{vis}} \approx I_{\mathrm{p}}$) was set at 150, 50 and 25 GW/cm^2, respectively, so as to obtain $\sim$ 50 % energy depletion of the highest frequency (visible) pulse. Note, that in a difference frequency mixing process, the highest frequency wave is depleted, whereas both lower frequency waves

are amplified. Under the chosen parameters of interaction, BBO crystal of 0.2 mm thickness was found to be optimal, as it provided the best compromise between the energy conversion efficiency [$E_{MIR}/(E_{vis}+E_p) = 2.5$ %] and attainable pulse width (the pulse broadening being less than 10% across the entire tuning range).

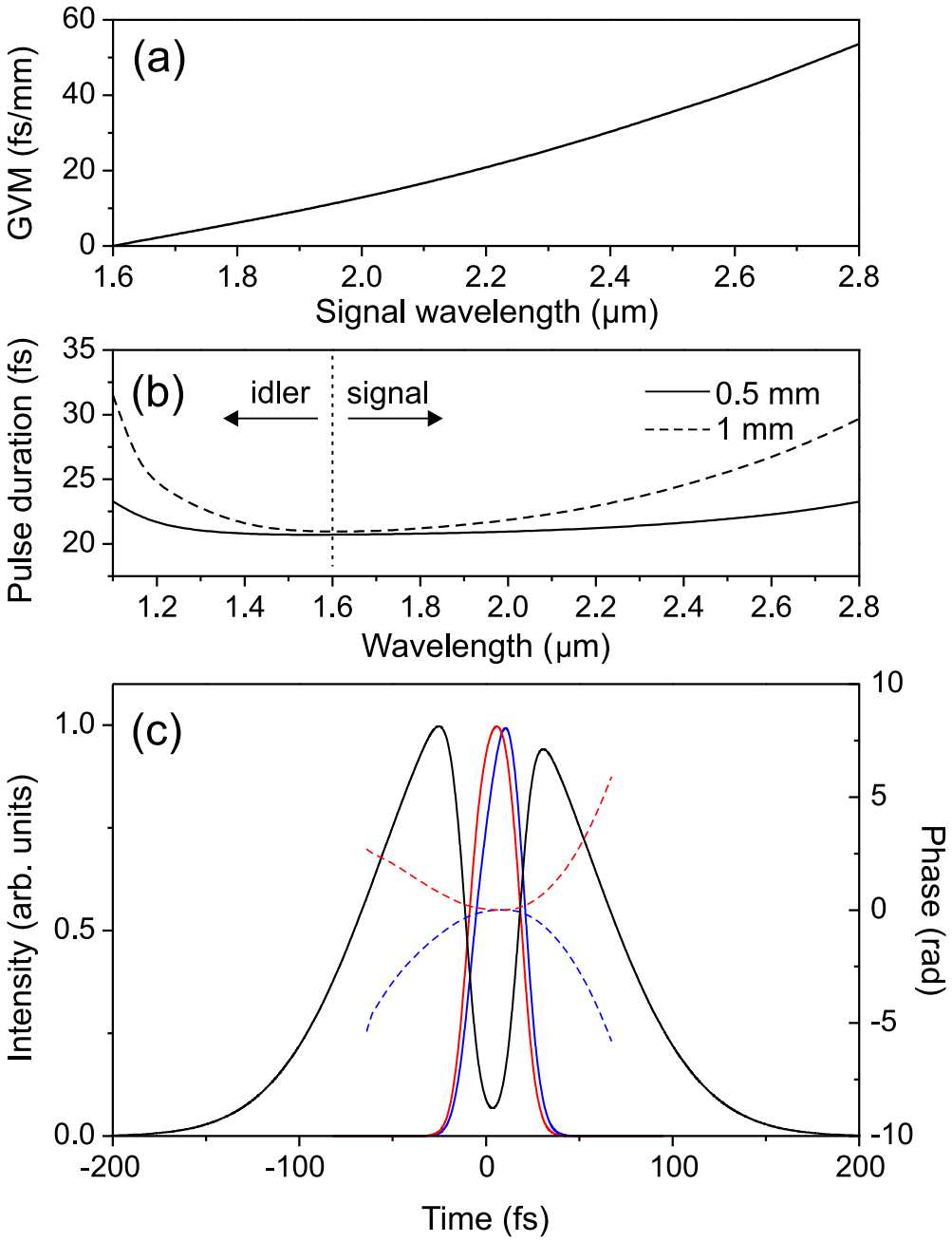

Figure 3.9: (a) Group velocity mismatch between the signal and idler pulses in BBO crystal. (b) computed FWHM pulsewidth as a function of wavelength at the OPA output, which uses 0.5 mm and 1 mm BBO crystals. (c) temporal pulse profiles of the depleted pump (black), amplified signal at 2 μm (blue) and idler at 1.33 μm (red). The dashed curves show phases of the signal and idler pulses, respectively.

Further we simulate the operation of a difference-frequency pulse-seeded collinear OPA, which was pumped by $t_p = 130$ fs fundamental laser pulse. We investigate parametric amplification in BBO crystals of 0.5 mm and 1 mm thickness by choosing a fixed seed pulse intensity of 1 GW/cm^2 and the pump pulse intensities of 350 GW/cm^2 and 100 GW/cm^2 set for shorter and longer crystals, respectively, so as to obtain 15 % pump-to-infrared conversion efficiency with a gain of ~ 100. Fig. 3.9(a) shows the calculated group velocity mismatch, $1/v_s - 1/v_i$, between the signal and idler pulses, which essentially defines the accessible amplification bandwidth. Fig. 3.9(b) summarizes the numerically computed FWHM width of the signal and idler pulses across the entire tuning range. Fig. 3.9(c) shows an example of computed temporal profiles and phases of the interacting pulses ($\lambda_s = 2$ µm, $\lambda_i = 1.33$ µm) at the output of 1-mm-thick BBO crystal. Note, how the pump pulse is almost completely depleted in the area where the pulses overlap; the time separation between the signal and idler pulses at the crystal output is markedly reduced due to strong nonlinear interaction. Moreover, the use of unstretched and unchirped seed pulses in the OPA pays-off with regard of achieved pulse width; note that the amplified pulse lengthening is quite small and does not exceed 30% even at the very edges of the tuning range.

Experimental results

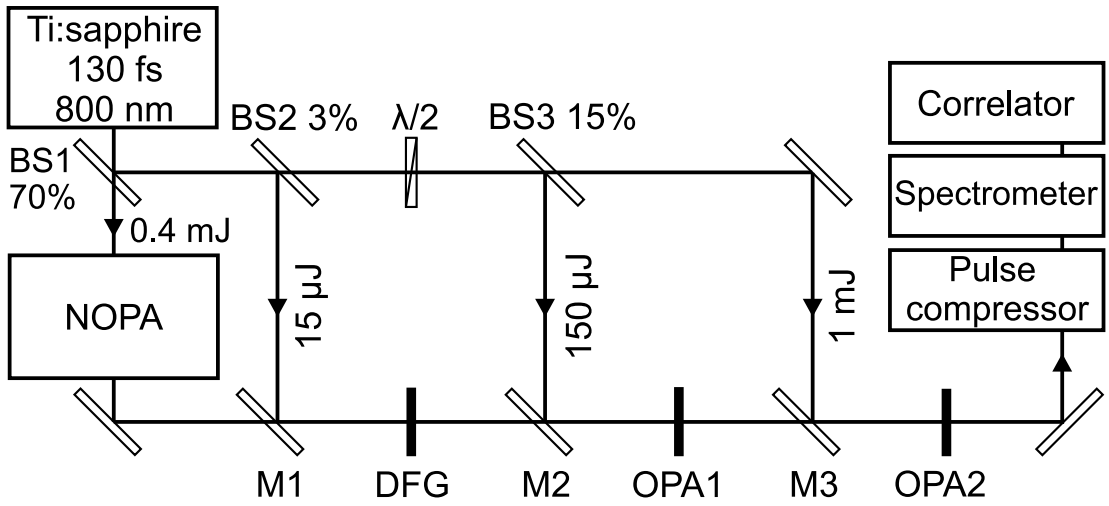

Figure 3.10: Experimental setup: DFG is the difference frequency generator, OPA1 is the preamplifier, OPA2 is the power amplifier, BS1, BS2 and BS3 are the beam splitters, $\lambda/2$ is a half-wave plate, M1 is a dichroic mirror (transparent in the visible and highly reflective at 800 nm), M2 and M3 are the dichroic mirrors transparent in IR and highly reflective at 800 nm.

The validity of the numerical results was verified experimentally. The experimental setup is depicted in Fig. 3.10. The fundamental Ti:sapphire laser beam was divided by the beam splitter BS1 into two parts. The first part, with 0.5 mJ energy, served to pump a NOPA device. The second part of the laser beam was divided into three channels (beam splitters BS2 and BS3) with energy of 15 µJ, 150 µJ and 1 mJ that served to pump the difference-frequency generator (DFG), preamplifier (OPA1) and power amplifier (OPA2), respectively.

The difference frequency generation was performed in a 0.2-mm-thick BBO crystal cut at 29.2° for type I phase matching. The input beams (NOPA output and laser fundamental) were arranged in a collinear geometry using a dichroic mirror M1. The beams were focused to a spot size of $\sim$ 0.5 mm with a spherical $f = +300$ mm lens thus achieving peak intensities of the input pulses of I_{vis}=65 GW/cm^2 and I_{p}=30 GW/cm^2. Under these experimental conditions the difference-frequency pulses with 200–400 nJ energy throughout the whole 1.6–2.4 µm range were generated. These further served to seed the OPA, which consisted of preamplifier and power amplifier, both based on type I phase matching BBO crystals. In order to fulfill type I phase matching condition, the polarization of the pump wave was rotated by 90° using a $\lambda/2$ plate placed in front to the beam splitter BS3.

The preamplifier used a 0.5 mm-thick BBO crystal, which was pumped by loosely focused 150 µJ fundamental pulse. The FWHM beam diameter at the crystal input face was 0.45 mm, yielding the pump pulse intensity of 450 GW/cm^2. The pump and seed beams were arranged in a slightly non-collinear geometry (the crossing angle $< 1°$) so as to easily separate the signal (1.6-2.4 µm) and idler (1.2–1.6 µm) beams of the same polarization. The preamplifier operated with 10% energy conversion efficiency, delivering 2–4 µJ signal pulses. Thereafter these pulses were sent to a power amplifier, which used 1-mm-thick BBO crystal and which was pumped by the rest of the laser energy (1 mJ) in a collimated beam with FWHM diameter of 1.6 mm and intensity of 250 GW/cm^2. The power amplifier delivered a total of 120 µJ energy, which was distributed between the signal and idler waves according to Manely-Rowe relation. For instance, at signal and idler wavelengths of 2.06 µm and 1.31 µm, where pulses were characterized (see below), the measured energy of the signal and idler waves was 45 µJ and 75 µJ, respectively.

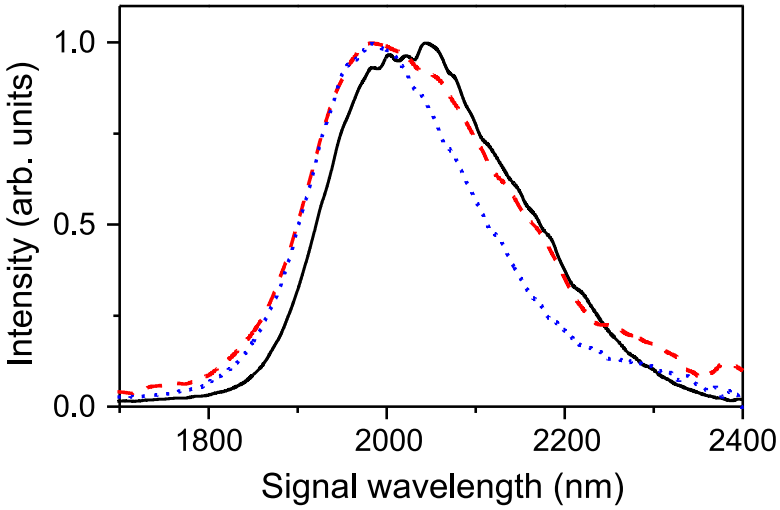

Figure 3.11: Comparison of the pulse spectra after the difference-frequency generator (dotted curve), and at the output of the preamplifier (dashed curve) and power amplifier (solid curve).

The spectral characteristics of the pulse at 2.06 µm at relevant stages of the experiment are depicted in Fig. 3.11, which compares pulse spectra after the difference frequency generation, and at the outputs of the preamplifier and power amplifier, as measured using fiber spectrometer (AvaSpec-NIR256-2.5, Avantes). Note that the modifications of the spectral shape imposed by the optical parametric amplification process are very minor: the observed spectral narrowing was estimated to be less than 10%, in good agreement with the results of numerical simulations. The measured FWHM spectral width at the output of the power amplifier was $\sim$ 250 nm, that corresponded to 24 fs transform-limited pulse duration.

Figures 3.12 and 3.13 summarize the main experimental results. Figure 3.12(a) shows spectra of the visible pulses at 575 nm and the amplified MIR (signal) and NIR (idler) pulses centered at 2.06 µm and 1.31 µm, respectively. Figure 3.12(b) shows the temporal characteristics across the whole tuning range by presenting the measured pulse width of the visible pulses at the NOPA output and the estimated pulse width of the signal (MIR) and idler (NIR) waves as derived from spectral measurements and subsequent Fourier transform. The dashed lines indicate the pulse width, which corresponds to N=3, 4 and 5 optical-cycles. The experimental data are in fair agreement with the results of numerical simulations, presented in Fig 3.9(b).

Figure 3.13 shows the autocorrelation traces of compressed signal and idler pulses as measured by a scanning autocorrelator (described in Sect. 3.2).

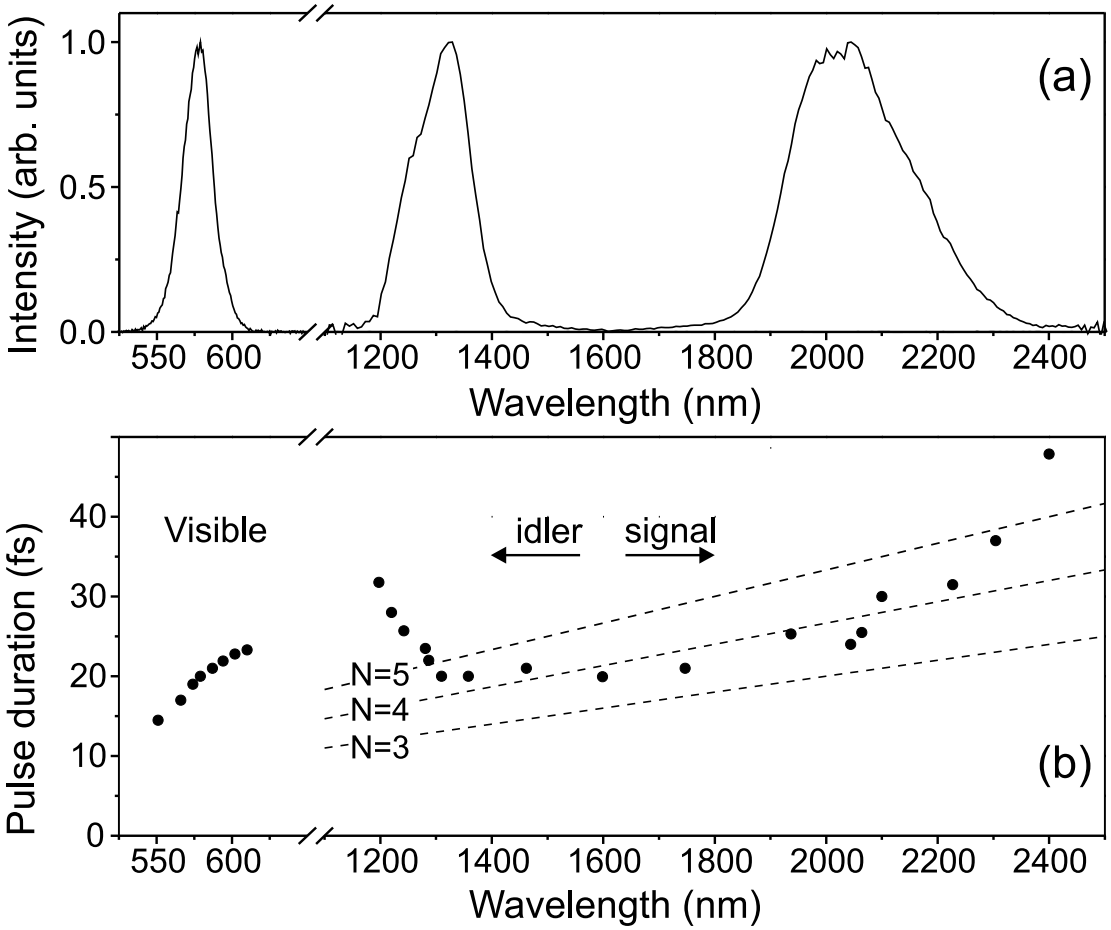

Figure 3.12: (a) spectra of the visible, NIR and MIR pulses centered at 575 nm, 1.31 µm and 2.06 µm, respectively. (b) pulse duration versus wavelength. The dashed lines indicate the pulse duration with N=3, 4 and 5 optical-cycles.

It has to be mentioned that although we consider parametric amplification of unchirped signal pulse, in fact, in the experiment it became negatively chirped (blue-shifted frequencies at the leading front and red-shifted frequencies at the trailing front) due to anomalous material dispersion introduced by the optical elements of the setup (focusing lenses, dichroic mirrors and autocorrelator optics) in the 1.6–2.4 µm wavelength range. Indeed, the measured duration of the signal pulse at 2.06 µm directly at the amplifier output was 110 fs. Therefore the signal pulse was compressed by passing it through a 3-mm-thick ZnSe plate, which possesses normal group velocity dispersion in this spectral range. The autocorrelation trace of compressed signal pulse is plotted in Fig. 3.13(a), which shows a smooth Gaussian profile. The estimated FWHM pulsewidth of 29 fs (4.2 optical-cycles) thus yielded the time-bandwith product of $\Delta\tau\Delta\nu \approx 0.51$. Slightly imperfect pulse chirp compensation (measured pulse width of 29 fs instead 24 fs as

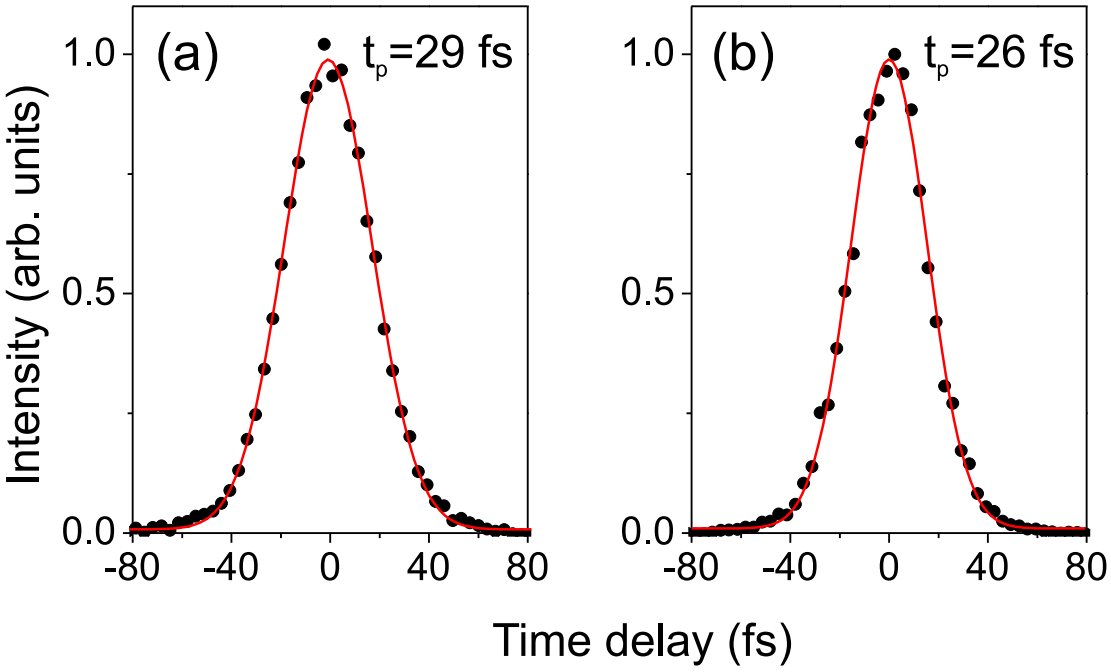

Figure 3.13: Autocorrelation traces of compressed pulses: (a) signal pulse at 2.06 µm, (b) idler pulse at 1.31 µm. Full circles show the experimental data, solid curves show Gaussian fit.

estimated from the spectral width) occurred likely due to higher-order dispersion imposed by ZnSe, as also noted in [91]. The positive chirp of the idler pulse, as attained in the parametric amplification process was compensated in a double-pass TF5 glass prism-pair compressor. The autocorrelation trace of compressed idler pulse at 1.31 µm is shown in Fig. 3.13(b), which again shows a smooth Gaussian profile. The retrieved FWHM pulse width of 26 fs and the time-bandwidth product of $\Delta\tau\Delta\nu \approx 0.46$ attest almost perfect compensation of the idler pulse chirp.

To sum up, a simple method for visible-to-infrared frequency conversion of sub-30 fs pulses by collinear difference frequency generation and subsequent collinear optical parametric amplification was presented in this section. As an experimental proof, the generation of broadly tunable few optical-cycle pulses using BBO crystals in the wavelength range of $1.2 - 2.4$ µm was demonstrated. After two-stage optical parametric amplification, we obtain sub-100 µJ pulses with 10% pump-to-infrared conversion efficiency. The validity of the concept is supported by the results of the numerical simulations.

3.3.3 Simultaneous difference frequency generation and optical parametric amplification in a single BBO crystal

In this section we proceed with the BBO crystal based visible-to-infrared frequency conversion setup described in Sect. 3.3.2. Here, however the DFG and OPA interactions are realized in a single type I BBO crystal.

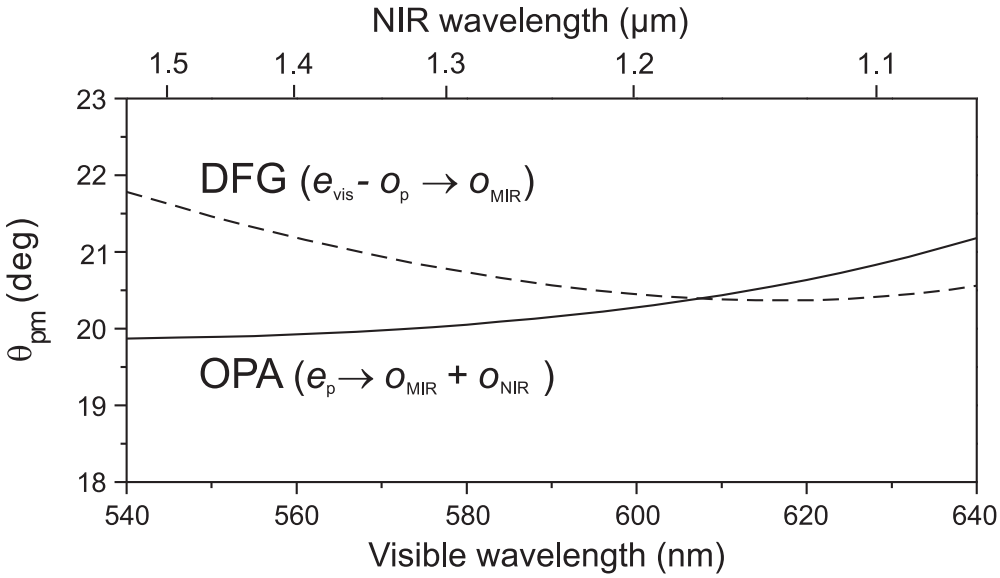

Figure 3.14: Phase matching curves for DFG (dashed line) and OPA (solid line) processes for type I phase matching in BBO crystal.

The method is based on cascaded three-wave parametric interactions (DFG and OPA), that occur simultaneously within a single type I BBO crystal due to its dispersion properties. The phase-matching curves in BBO crystal for both DFG ($e_{\mathrm{vis}} - o_p \rightarrow o_{\mathrm{MIR}}$) and OPA ($e_p \rightarrow o_{\mathrm{MIR}} + o_{\mathrm{NIR}}$) processes are illustrated in Fig. 3.14. Here o and e denote the necessary polarization of the interacting waves so as to fulfill the type I phase matching interaction. Note that this is possible using different polarizations of the pump wave at ω_p. The efficiency of the overall cascading process relies on two conditions: (i) both parametric interactions have to be of the same phase matching type, thus the polarization of the interacting waves should be properly chosen; (ii) only one of the two parametric processes could be perfectly phase matched at fixed crystal orientation (except the point at 607 nm, where the DFG and OPA curves intersect). The optimum operation was achieved when the BBO crystal was aligned so as to fulfill the perfect phase matching condition for the OPA process that is very efficient, whereas a difference frequency

generation was phase-mismatched therefore providing a weak seed, which was nevertheless enough to efficiently seed the amplifier.

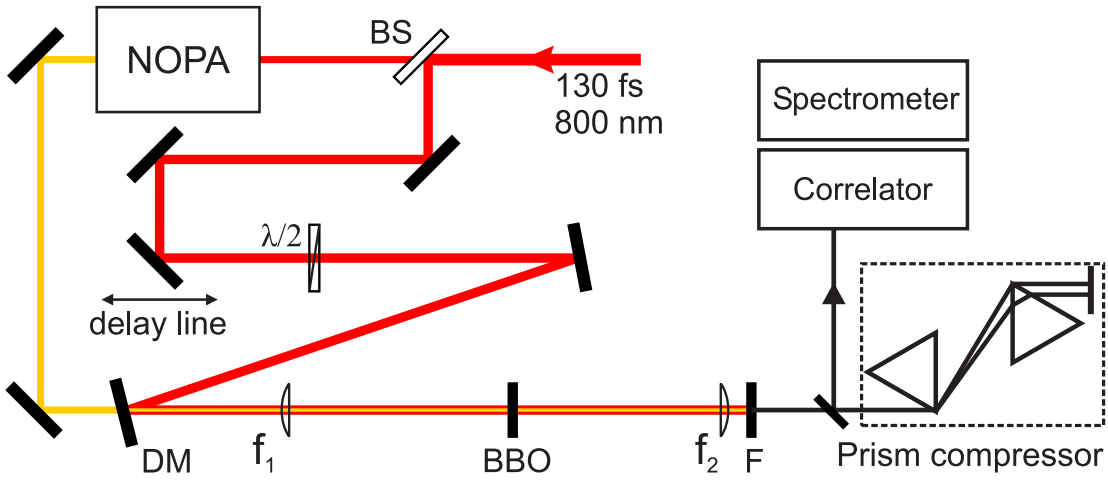

Figure 3.15: Experimental setup for cascaded frequency conversion in BBO crystal: BS is the beamsplitter, $\lambda/2$ is a half-wave plate, DM is a dichroic mirror, f_1 and f_2 are beam focusing and restoring lenses, respectively, F is a bandpass filter.

The experimental setup is depicted in Fig. 3.15. The Ti:sapphire laser-NOPA system was the same as described in Sect. 3.2. A dichroic mirror DM (transparent in the visible and highly reflective at 800 nm) was used for collinear arrangement of the NOPA and pump beams. The two beams were focused with a spherical $f_1 = +800$ mm lens into 1-mm-thick BBO crystal cut at $\theta = 29.2°$. The BBO crystal was placed $\sim$ 20 cm before the focal plane of the lens; the FWHM size of pump and signal beams at the input face of the crystal were measured as 0.77 mm and 0.45 mm, respectively. The generated NIR beam was restored with $f_2 = 500$ mm lens, while the remaining pump and NOPA signal were filtered using bandpass filter F. The proper energy ratio between *o*- and *e*-polarized waves at 800 nm was adjusted with a half-wave plate ($\lambda/2$). The optimum performance was achieved when $\sim 5\%$ fraction of the energy at 800 nm was used to generate the difference-frequency and the rest $\sim 95\%$ served as a pump for OPA. The maximum pump energy of $E_p = 0.4$ mJ in the experiment was used, that converts to a maximum fluence of $F_{\max} = 0.056$ J/cm^2. We note, that no optical damage of the crystal antireflection coatings was observed. The maximum pump intensity was estimated as $I_{\max} = 0.43$ TW/cm^2, assuming Gaussian spatial and temporal intensity distribution of the pump beam.

Figure 3.16(a) shows the energy of the NIR (at 1.24 µm) and MIR (at 2.25 µm) pulses at the BBO crystal output as a function of the pump en-

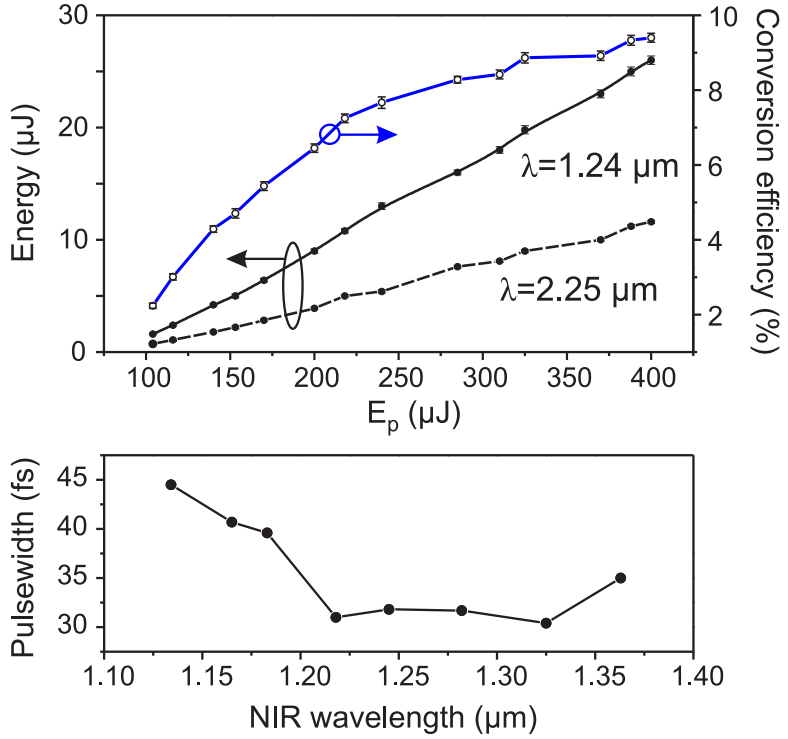

Figure 3.16: (a) Infrared pulse energies at 2.25 µm (dashed curve) and 1.24 µm (solid curve) and pump-to-infrared conversion efficiency versus pump energy. (b) Compressed NIR pulse duration versus wavelength.

ergy. With $E_p = 0.4$ mJ and $E_{\text{vis}} = 7$ µJ the highest infrared pulse energy of $E_{\text{MIR}} = 11.5$ µJ and $E_{\text{NIR}} = 26$ µJ was measured suggesting almost 10% pump-to-infrared conversion efficiency as the frequency conversion process was driven into saturation. Figure 3.16(b) shows the NIR pulse duration versus wavelength after the pulse compression in a double-pass prism-pair compressor (identical to that described in Sect. 3.2) as measured by a scanning autocorrelator (described in Sect. 3.2). For most of the tuning range, pulses as short as 30 fs were obtained, whereas at the shortest wavelengths ($1.1 - 1.2$ µm), the pulse duration increased to 40-45 fs, mainly as a result of reduced gain bandwidth for shortest NIR wavelengths.

Figure 3.17 summarizes the relevant characteristics of the cascaded three-wave parametric frequency converter at 1.36 µm and 1.22 µm. The left panel [Fig. 3.17 (a) and (d)] compares spectra of the visible NOPA seed. The center panel [Fig. 3.17 (b) and (e)] illustrates spectra of the frequency down-converted NIR pulses. The right panel [Fig. 3.17 (c) and (f)] shows the autocorrelation traces of the compressed NIR pulses as measured by a scanning autocorrelator. The estimated time-bandwidth product $\Delta\tau_p\Delta\nu \approx 0.5$ at both wavelengths indicates that the compressed NIR pulses are close to

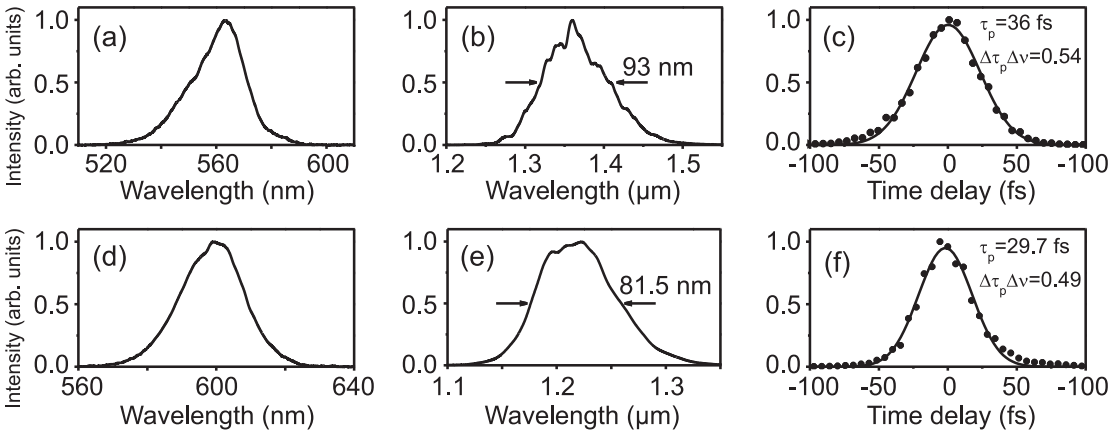

Figure 3.17: Experimentally measured pulse characteristics at 1.36 μm and 1.22 μm. (a), (d) spectra of the visible NOPA seed; (b), (e) spectra of the NIR pulses; (c), (f) autocorrelation traces of compressed NIR pulses. Here solid curves show the Gaussian fit.

transform limit.

The presented second-order cascaded interaction to some extent mimics pure four-wave mixing process: $\omega_p + \omega_p = \omega_{\text{vis}} + \omega_{\text{NIR}}$. However, in the present case the conversion efficiency is markedly higher because of much higher induced second-order nonlinear polarization. Another important outcome of the proposed scheme is that tunable MIR pulses are simultaneously generated via DFG process, and that are not present in pure four-wave mixing process. The NIR and MIR pulses in principle can be tuned in $1.1 - 1.6$ μm and $1.6 - 2.8$ μm spectral ranges respectively. Close to degeneracy (1.6 μm), however, these pulses cannot be distinguished neither in polarization nor in wavelength, since they are generated in type I crystal employing collinear configuration. The MIR pulses were not precisely characterized due to the absence of suitable (MIR sensitive) detection apparatus at the time the experiment was made.

3.3.4 Noncollinear BBO crystal-based optical parametric amplification in the IR spectral range

The three-wave OPAs presented so far delivers tunable ≈ 30 fs IR pulses. Generation and amplification of even shorter (< 30 fs) IR pulses, however, requires broad amplification bandwidth, that is achieved only using noncollinear phase matching geometry as described in general introduction (Sect. 1.4). To this end, the noncollinear optical parametric amplification

with 800 nm pumping has been demonstrated using different nonlinear crystals, which provide suitable group velocity matching for broadband amplification: potassium titanyl phosphate (KTP) [95, 95], lithium iodate [26] and PPSLT [85, 94, 96]; also see [86] for a review and recent developments in the field. BBO crystal, on the other hand, was considered as unsuitable for broadband amplification in the IR using an 800 nm Ti:sapphire laser pump [94].

Stable CEP is often a mandatory requisite for pulses with few-optical-cycle duration. Control of the CEP becomes important for extreme nonlinear optics experiments, which are sensitive to the electric field rather than the pulse intensity, i.e. high-harmonic generation [22], above-threshold ionization [24], multiphoton absorption [40]. In particular, CEP control is important for the generation of reproducible attosecond pulses [23]. CEP can be stabilized using active or passive methods. Active approach relies on measuring the pulse-to-pulse CEP slip $\Delta\phi$ in the oscillator and stabilizing it with active electronic feedback [41]. Then, it is sufficient to pick and amplify pulses with the same phase at a fraction of oscillator repetition rate [22]. The parametric interactions, on the other hand, offer passive CEP stabilization in a quite straightforward way: optical parametric amplification might itself produce CEP-stable idler wave [42] or CEP-stable pulses could be generated by difference-frequency mixing process [43, 44].

To date, a variety of schemes providing CEP-stable few optical-cycle pulses at wavelengths around 2 µm with different energies (ranging from hundreds of nJ to several mJ), at different repetition rates (1-100 kHz), and possessing either broad tunability or operating at fixed wavelength have been developed [26, 27, 89–91, 103–107], with particular output parameters dictated by the range of practical applications.

In this section we demonstrate the generation of few optical-cycle pulses at 2 µm central wavelength. Pulses with stable CEP are obtained by difference frequency mixing then amplified in a noncollinear, 800-nm-pumped optical parametric amplifier based on BBO crystal, which in these conditions is shown to provide broad amplification bandwidth. The experimental setup is depicted in Fig. 3.18. The fundamental laser beam was divided by the beam splitter BS1 into two parts. The first part with 0.3 mJ energy, served to pump NOPA device, schematically shown as a shaded box in Fig. 3.18. The second part of the laser beam was divided into two channels (beam splitter

BS2) with energies of 30 µJ and 1 mJ that were used to pump the difference-frequency generator and the optical parametric amplifier, respectively.

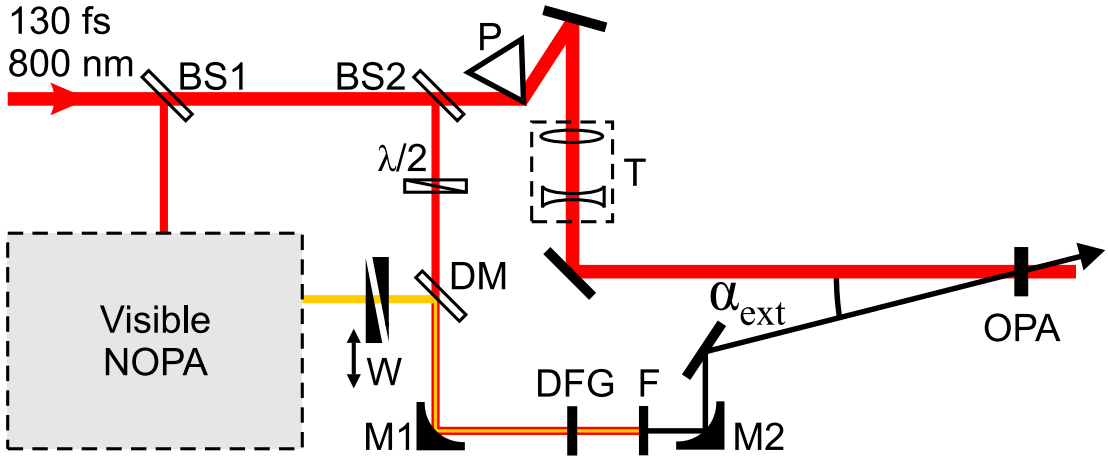

Figure 3.18: Experimental setup. NOPA is the noncollinear optical parametric amplifier, DFG is the difference frequency generator, OPA is the optical parametric amplifier, DM is the dichroic mirror, W is a pair of fused silica wedges, F is the bandpass filter, P is the prism, T is the telescope, BS1 and BS2 are the beam splitters, M1 and M2 – focusing and restoring mirrors.

The DFG scheme was similar to those proposed in Sects. 3.3.3 and 3.3.2: the pulse with central 2 µm wavelength was generated by mixing the *o*-polarized 130-fs pulse at 800 nm from the laser with the *e*-polarized, slightly positively chirped pulse at 575 nm from the NOPA in 0.2-mm-thick BBO crystal cut for type I phase matching. The proper polarization of the 800 nm pulse was set by the $\lambda/2$ plate placed after the beam splitter BS2. The two input beams were arranged collinearly using a dichroic mirror DM and loosely focused by a curved mirror M1 ($f = +300$ mm) onto the crystal. The DFG operated with 50% energy depletion of the visible pulse, delivering *o*-polarized 300 nJ pulse at 2 µm. The residual radiation at 575 and 800 nm was thereafter filtered by a bandpass filter F, isolating the difference frequency pulse, which was then collimated by another curved mirror M2 and sent to the OPA.

The OPA was based on type I phase matching BBO crystal, which due to its dispersive properties is generally considered as unsuitable for non-degenerate amplification of broadband pulses in the infrared [94]. Indeed, with 800 nm pumping, the signal pulse always moves faster than the idler, so broadband phase matching is not achievable neither in collinear nor in noncollinear geometry. The latter is true, when the OPA is seeded in the $1-1.6$ µm spectral range. However, recent findings uncover that the group

velocities of the signal and idler pulses could be matched noncollinearly either by using signal pulses with tilted front as demonstrated in [107] or by seeding the OPA in the $1.6-2.8$ µm range as proposed in present study. In the latter case, there exists a certain pump-seed crossing angle α, which satisfies the condition for broadband phase matching, as illustrated in the inset of Fig. 3.19.

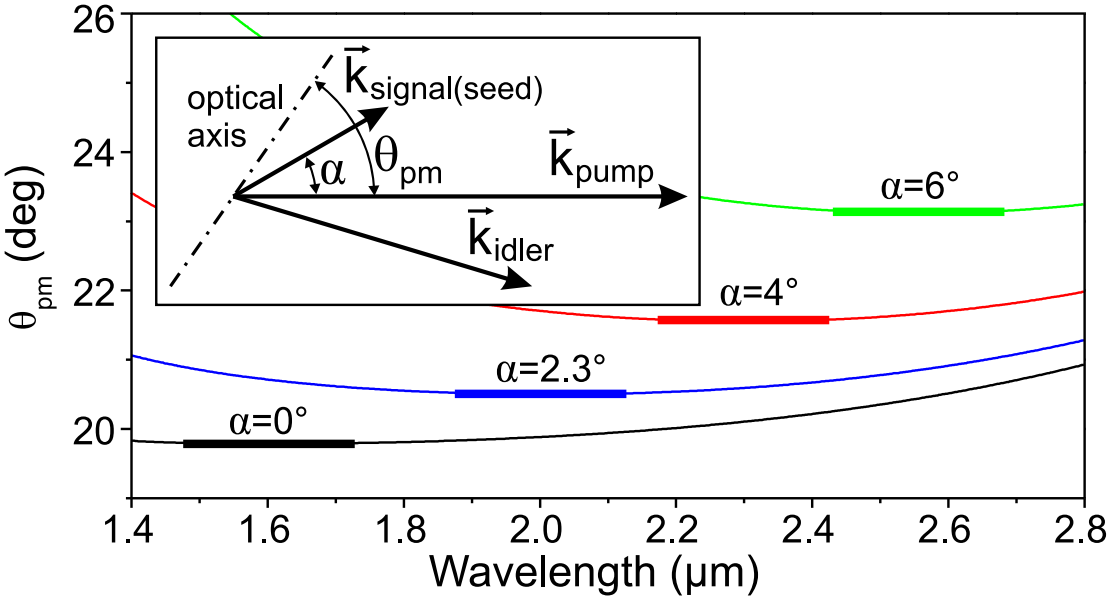

Figure 3.19: Phase matching curves calculated for type I phase matching BBO OPA pumped at 800 nm, varying pump-seed angle α. Inset shows geometry of the interacting beams inside the crystal.

The phase matching curves calculated for several pump-seed crossing angles α in type I phase matching BBO crystal are shown in Fig. 3.19. The phase matching curves for $\alpha \neq 0$ are in fact almost identical to the phase matching curve obtained in the collinear geometry ($\alpha = 0$) at the degeneracy (1.6 µm), with the difference of the position of the broad flat part (indicated by bold and serving as a guide for the eye) that shifts toward longer wavelengths with increasing α. Therefore by varying the pump-seed angle α, it is possible to achieve broadband phase matching anywhere in the seed wavelength range of $1.6-2.8$ µm, at the same time producing an angularly dispersed signal pulse in the range of $1.1-1.6$ µm.

In the experiment, the OPA used a 2 mm-thick BBO crystal, which was pumped by a collimated beam with FWHM diameter of 2.7 mm and 1 mJ energy. The *e*-polarized pump and *o*-polarized seed beams were crossed at $\alpha_{\text{ext}} = 3.8°$ angle (corresponding to $\alpha \approx 2.3°$ inside the crystal) so as to ensure the broadest amplification bandwidth around 2 µm. The noncollinear

geometry generally results in a noticeable reduction of the beam/pulse physical overlap area in the nonlinear crystal and imposes a tilted gain volume, which in turn produces a pulse-front tilt of the amplified pulse. In order to eliminate these drawbacks, the pump beam was transmitted through a fused silica prism P (apex angle of 69°) adjusted at a minimum deviation angle and a telescope T (beam size reduction factor of 2.4), which introduced a ∼2.3° pulse-front tilt inside the crystal, so as to produce untilted pulse and enhance conversion efficiency. At the output of the NOPA a pair of adjustable parallel fused silica wedges (W) were used to introduce a variable amount of material dispersion in the path of the visible pulse. As a result, the visible pulse was slightly positively chirped (red-shifted frequencies at the leading front and blue-shifted frequencies at the trailing front) and so the 2 µm difference-frequency pulse at the DFG output. By precisely controlling wedge position, we achieved that the 2 µm pulse self compresses after passing through 1-mm-thick bandpass filter F and 2-mm-thick OPA crystal, which both posses anomalous group velocity dispersion.

The two OPA configurations were analyzed. First, the phase matching angle of the crystal was set to $\theta_{\mathrm{pm}} = 20.5°$ so as to phase match the spectral components at 2 µm. Under these experimental conditions, pulses at 2 µm with 50 µJ energy and short-term (measured over 10 min interval) energy fluctuations of 2% were generated. Figure 3.20 shows zero-dispersion THG-

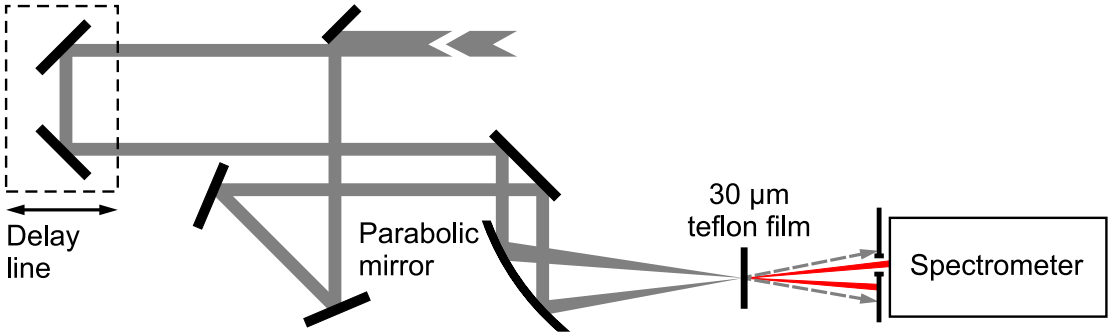

Figure 3.20: Schematic of the zero-dispersion THG FROG apparatus.

FROG apparatus, which was used to characterize the compressed pulses. First, the beam was spatially split into two parts by the edge of the mirror. The two portions were then focused into the 30-µm-thick teflon film with an $f = +100$ mm focal length parabolic mirror. The FROG measurement was performed by changing the time delay between the two correlator arms in 1.79 fs steps and recording the generated TH spectra by a fiber spectrometer (QE65000, Ocean Optics, ≈0.8 nm resolution). The acquired data was

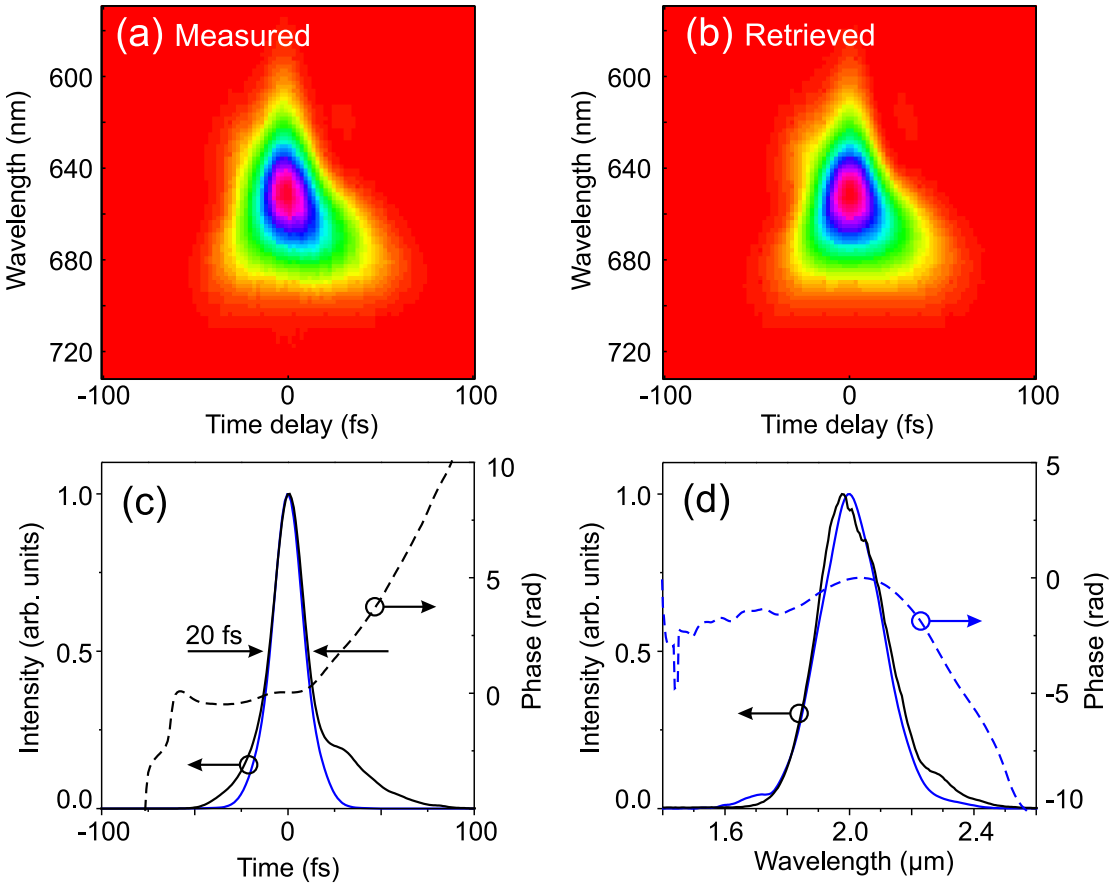

Figure 3.21: THG-FROG results of the amplified pulses. (a) Measured FROG trace, (b) retrieved FROG trace. (c) Reconstructed temporal profile (black curve) and phase (dashed curve), and temporal profile from zero-phase Fourier transform (blue curve). (d) Measured spectrum (black curve), reconstructed spectrum (blue curve) and reconstructed spectral phase (dashed curve).

converted into a 128×128 THG-FROG matrix as depicted in Fig. 3.21(a). Figure 3.21(b) shows the retrieved THG-FROG trace, while retrieved intensity and phase in both temporal and spectral domains are depicted in Fig. 3.21(c) and Fig. 3.21(d). The pulse width of 20 fs that corresponds to 3 optical-cycles was retrieved with a reconstruction error of 0.56%. The bandwidth of the amplified spectrum supports transform-limited pulse duration of 18 fs, as verified by zero-phase Fourier transform.

For the second configuration, the phase matching angle was tuned so as to phase match the marginal spectral components rather than the central ones, thus resulting in a spectral broadening as depicted in Fig. 3.22. The phase matching angle was set to $\theta_{\mathrm{pm}} = 20.9°$ and pulses at 2 μm with 15 μJ energy were generated. The results of THG-FROG are depicted in Fig. 3.23. The bandwidth of the amplified spectrum supports pulse duration of 12 fs, while the pulse width of 15 fs (2.3 optical-cycles) was retrieved

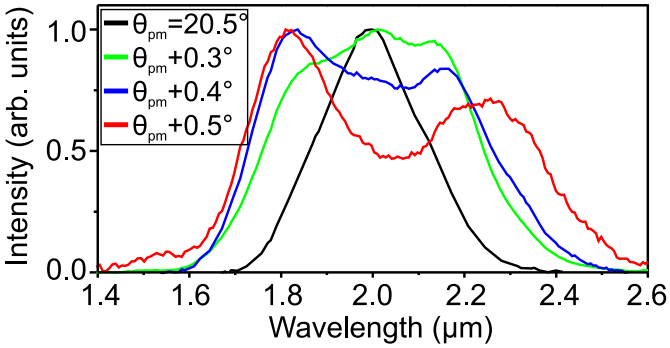

Figure 3.22: Experimentally measured spectra for different phase matching angle θ_{pm} values.

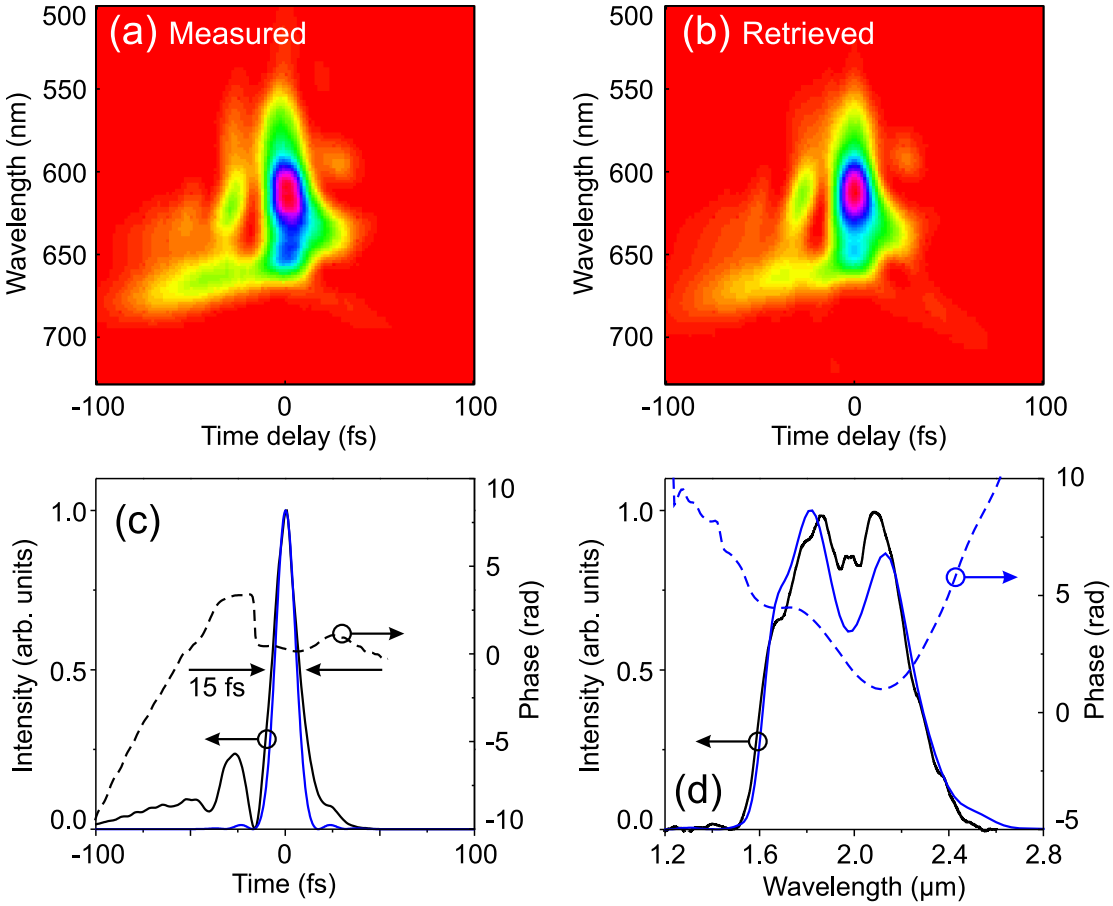

Figure 3.23: THG-FROG results of the amplified pulses. (a) Measured FROG trace, (b) retrieved FROG trace. (c) Reconstructed temporal profile (black curve) and phase (dashed curve), and temporal profile from zero-phase Fourier transform (blue curve). (d) Measured spectrum (black curve), reconstructed spectrum (blue curve) and reconstructed spectral phase (dashed curve).

within grid size of 256 × 256 pixels and a reconstruction error of 0.60%. An extended shoulder at the pulse front is likely due to residual higher-order dispersion, which could be compensated only by careful dispersion management. Rather low conversion efficiency (1.5%) is obtained in part

due to the quantum defect and in part due to different widths of the pump and seed pulses. Even broader spectrum that supports 10 fs pulses can be obtained by setting $\theta_{\mathrm{pm}} = 21°$ (red curve in Fig. 3.22), however due to higher order dispersion the obtained pulses were compressed only down to 18 fs (not shown).

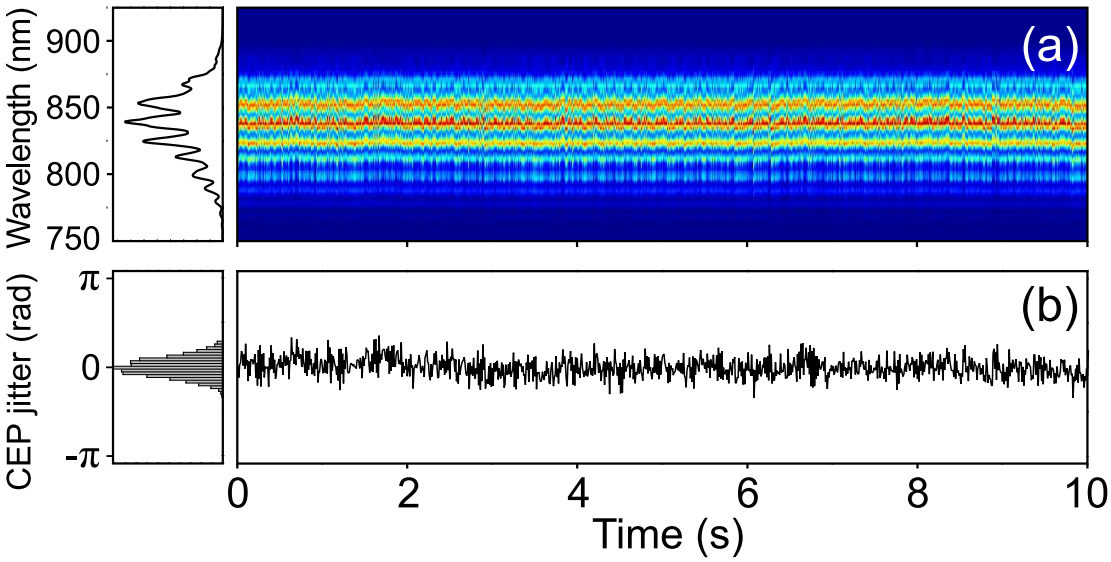

Figure 3.24: Measurement of CEP fluctuations: (a) f-2f interference pattern and its average, (b) variation of the CEP over time and its statistics.

And finally, our scheme produced pulses with self-stabilized carrier-envelope phase: the NOPA signal originates from the supercontinuum generation with 800 nm pulses whose phase fluctuations are transferred to the SC signal and which thereafter are cancelled during difference frequency generation process [43, 44], whereas pump fluctuations and phase mismatch in parametric amplification process do not significantly alter the amplified pulse CEP [108]. The experimental characterization of the CEP was performed with an f-2f interferometer described in Sect. 1.6 by sampling SC (generated in 6 mm thick YAG crystal) and its second harmonic spectra (generated in 1 mm thick BBO crystal) using a fiber spectrometer (QE65000, Ocean Optics). Figure 3.24(a) shows the interference fringe pattern as composed of 1000 single-shot spectral interferograms, which were measured by setting laser repetition rate at 100 Hz. The extracted CEP jitter is plotted in Fig. 3.24(b) indicating a root-mean-square (rms) fluctuations of 0.33 rads.

In conclusion, we have demonstrated a simple and flexible scheme that delivers two optical-cycle, CEP-stable pulses in the infrared. The method is

based on frequency down-conversion of visible pulses via collinear difference frequency generation and subsequent noncollinear optical parametric amplification in the BBO crystal, which is shown to provide broadband phase matching if seeded by ultrashort pulses in the $1.6 - 2.8$ µm wavelength range. As an experimental proof, 15 fs pulses with 15 µJ energy at 2 µm central wavelength, with short-term CEP stability of 330 mrad over 10 s were generated. The pulse width corresponds to 2.3 optical-cycles that is achieved by a simple propagation in the optical elements of the setup and does not require any external pulse compressor. The proposed scheme could be easily optimized for either shortest pulse duration or highest pulse energy by adjusting the phase matching angle of the crystal, and up-scaled to higher output energies. As compared to two previous setups (Sect. 3.3.2 and Sect. 3.3.3), the developed noncollinear OPA is not optimized for NIR pulse generation. Although the idler wave, which lies in the $1.1 - 1.6$ µm spectral range, is simultaneously generated in the amplification process, its use is less attractive because of significant spatial chirp.

3.3.5 Broadband optical parametric amplification in the 3–5.5 µm spectral range

The absorbing properties of the BBO crystal limit the tunability of the IR pulses to wavelengths shorter than 2.8 µm, although the available tuning range of visible NOPA is suitable to do so, as described in Sect. 3.3.1, see also Fig. 3.7. In what follows, we demonstrate a general possibility to extend the proposed concept for generation of few optical-cycle pulses in the MIR. We perform the numerical simulations of difference-frequency pulse-seeded optical parametric amplification in the MIR in $LiIO_3$ and $LiNbO_3$ crystals, whose relevant parameters were taken from [102, 109]. Here we consider an identical situation of the OPA operation as in Sect. 3.3.2: unchirped ~ 20 fs MIR seed pulses are amplified in a collinear type I phase matched OPA pumped by 130 fs pulses at 800 nm.

Figure 3.25 summarizes the results of numerical simulations of parametric amplification in $LiIO_3$ crystal. Figure 3.25(a) shows the GVM between the signal and idler pulses in the signal wavelength range of $1.6-5.5$ µm. Interestingly, apart from the degeneracy, there exists a second group-velocity matching point at 4.2 µm, where conditions for collinear broadband parametric amplification are fulfilled. At longer wavelengths the group velocity

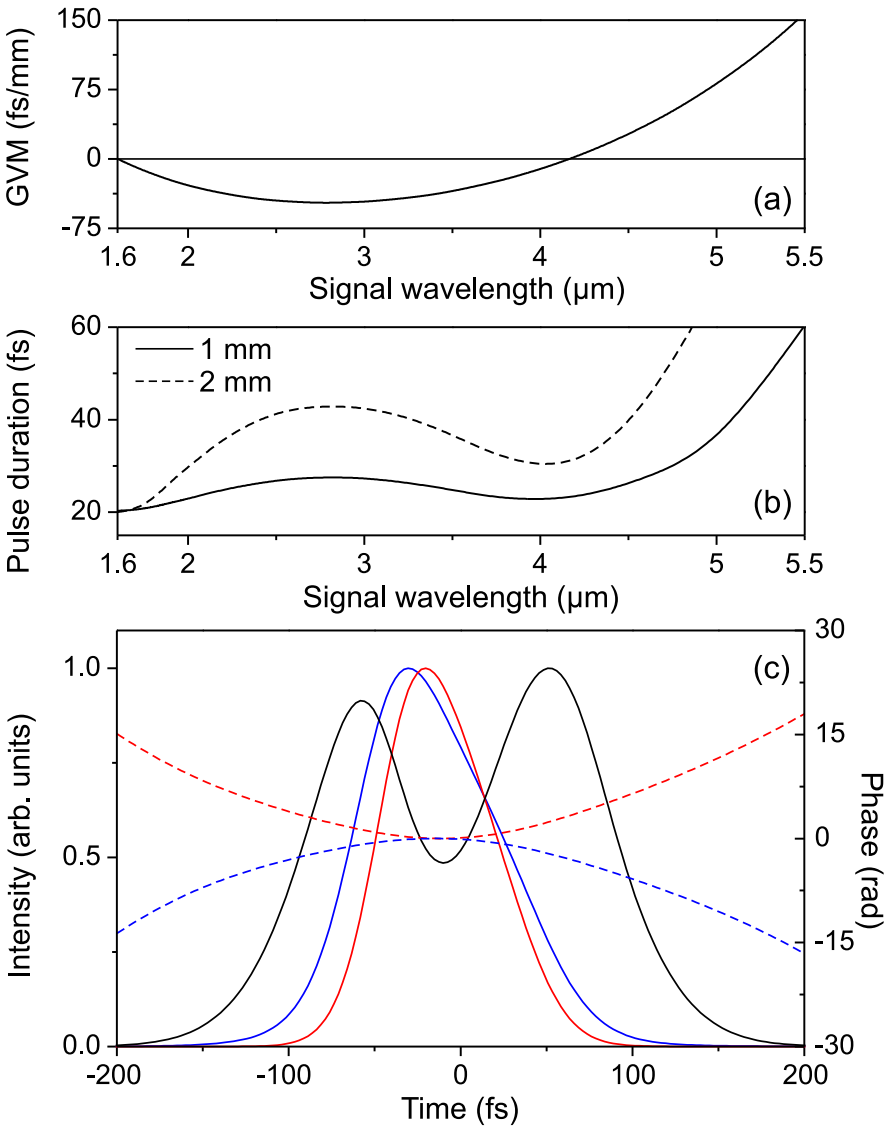

Figure 3.25: Performance characteristics of $LiIO_3$ crystal-based OPA. (a) GVM between the signal and idler pulses. (b) computed FWHM pulse width versus wavelength in 1 mm (solid curve) and 2 mm (dashed curve) thick crystals. (c) temporal pulse profiles of the depleted pump (black), amplified signal at 4 μm (blue) and idler at 1 μm (red). The dashed curves show phases of the signal and idler pulses, respectively.

mismatch rapidly increases, thereby limiting the effective tuning range to wavelengths shorter than 5.5 μm due to reduced amplification bandwidth. Figure 3.25(b) depicts the computed achievable transform-limited FWHM pulse width (after compensation of residual pulse chirp) of the MIR signal pulses at the output of the OPA, which uses $LiIO_3$ crystals of 1 mm and 2 mm thickness. Here optical parametric amplification was simulated using pump pulse intensity of 100 GW/cm^2, that produced gain factors of 5 and 50 in shorter and longer crystals, respectively. Figure 3.25(c) shows an

example of numerically simulated intensity profiles and phases of the interacting pulses in 2-mm-thick $LiIO_3$ crystal at the group-velocity matching point at 4.2 µm.

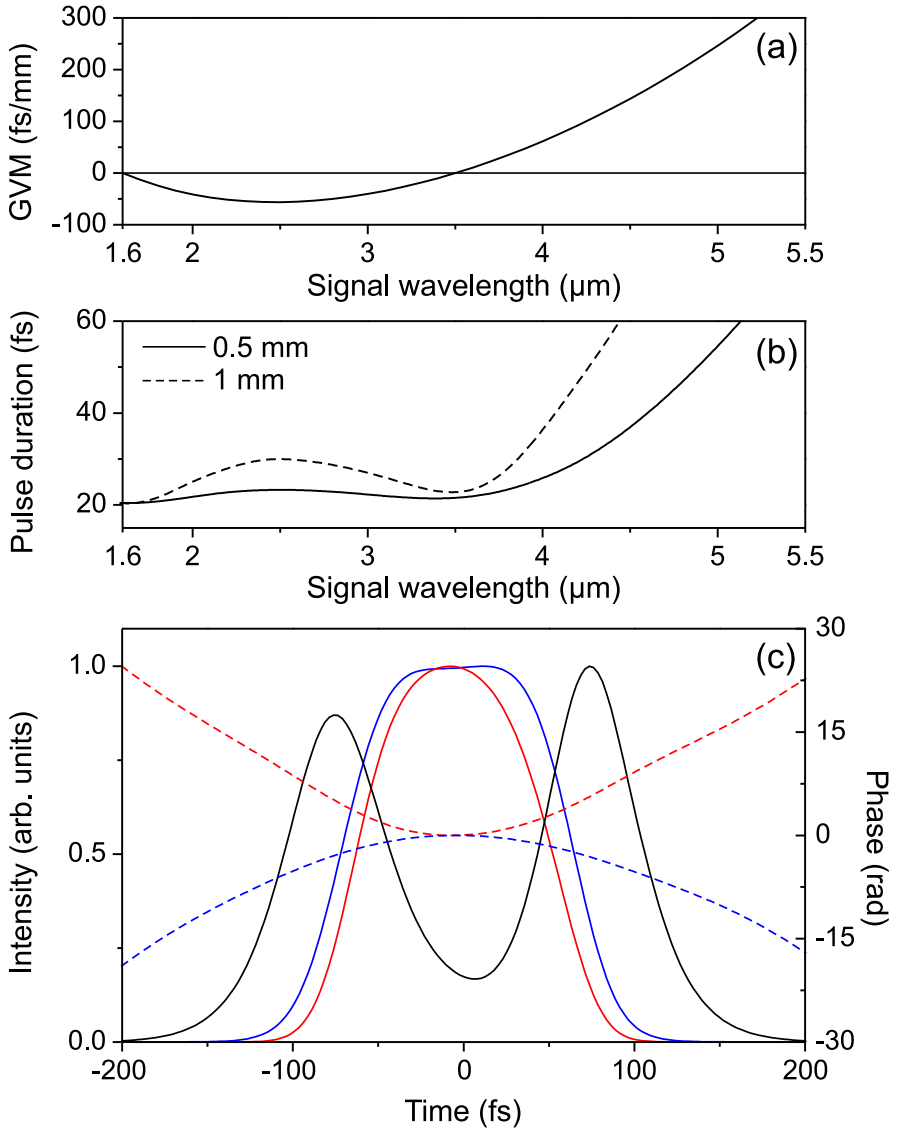

Figure 3.26: Performance characteristics of $LiNbO_3$ crystal-based OPA. (a) GVM between the signal and idler pulses. (b) computed FWHM pulse width versus wavelength in 0.5 mm (solid curve) and 1 mm (dashed curve) thick crystals. (c) temporal pulse profiles of the depleted pump (black), amplified signal at 3.5 µm (blue) and idler at 1.04 µm (red). The dashed curves show phases of the signal and idler pulses, respectively.

Figure 3.26 shows the GVM between the signal and idler pulses in $LiNbO_3$ crystal and basic performance characteristics of $LiNbO_3$ crystal based OPA. Figures 3.26 (a) and (b) show the group velocity mismatch and achievable pulse width, respectively. Here collinear group velocity matching between the signal and idler pulses occurs at 3.5 µm. Thanks to larger

nonlinear coefficient of $LiNbO_3$, 1-mm-long crystal yields as much a twice gain (~ 100) than that achieved in twice longer $LiIO_3$ crystal at the same pumping intensity of $I_p = 100$ GW/cm^2. The intensity profiles of the pump, signal and idler pulses at the output of 1-mm-long $LiNbO_3$ crystal-based OPA are shown in Fig. 3.26 (c).

To summarize the results of numerical simulations, the performance characteristics of $LiIO_3$ and $LiNbO_3$ OPAs are quite similar. However, in choosing a particular value of the pump intensity ($I_p = 100$ GW/cm^2) we did not accounted for a possible optical damage of the $LiIO_3$ crystal, which is expected to occur at lower intensities than in $LiNbO_3$, since exact optical damage thresholds for these crystals in the femtosecond regime are not precisely known. In both investigated cases, shown in Fig. 3.25 (c) and in Fig. 3.26 (c), the amplified pulses feature some phase modulation, which occurs as a result of group velocity dispersion. Larger group velocity dispersion in $LiNbO_3$ crystal results in somewhat longer pulses with larger chirp at the OPA output. On the other hand, the character of phase modulation in both cases is very regular (quadratic), so it could be readily compensated using an external pulse compressor. Our findings suggest that at particular wavelengths (4.2 µm in $LiIO_3$ and 3.5 µm in $LiNbO_3$) after compensation of residual chirp, pulses with duration shorter than 2 optical-cycles could be obtained.

Chapter 4

Supercontinuum generation with few optical cycle CEP-stable pulses

Material related to this chapter was published in [A12]

4.1 Motivation

Supercontinuum generation is a well-established method for obtaining coherent broadband radiation, spanning across ultraviolet, visible and infrared spectral range [110]. In bulk dielectric media, SC generation is tightly linked to femtosecond filamentation [25]; the broadband radiation emerges from a complex interplay between self-focusing, self-phase modulation, four-wave mixing, pulse-front steepening, pulse splitting, generation of optical shocks, multiphoton absorption and generation of free electron plasma. To date, SC generation was extensively studied in wide bandgap dielectrics with ultraviolet, visible and near infrared femtosecond laser pulses, under conditions of normal group velocity dispersion [111–113]. On the other hand, it is well known that the material dispersion plays an important role in self-focusing dynamics of the ultrashort laser pulses [25]. Thanks to recent progress in the development of ultrafast optical parametric amplifiers, ultrashort pulses at near and mid-infrared wavelengths became routinely available, see e.g. [86], thus providing an access to SC generation in the regime of anomalous GVD. Indeed, experimental and numerical studies revealed that the interplay between the anomalous GVD and self-action effects results in extended filamentation length [114], pulse compression rather than pulse splitting [115–118], different angular pattern of conical emission [119–121] and ultrabroadband spectra [113, 122–126], hence giving rise to a new filamentation

regime in general [118].

Another effect associated with filamentation is the generation of TH, whose occurrence is mediated by the same source of the nonlinear polarization [127, 128]. Indeed, TH generation is a well-known phenomenon, which accompanies filamentation and spectral broadening in gases and air in particular, see e.g. [129–131], however it is seldom observed [61] and often neglected effect regarding filamentation and SC generation in condensed media.

In this Chapter we experimentally investigate SC generation in the regime of anomalous GVD with 20 fs, CEP-stable pulses at 2 µm. We find that TH generation occurs prior to spectral broadening, and the TH pulse has a specific double-peaked structure, which coexists with the SC also in the regime of spectral superbroadening. We also demonstrate that spectral beating between TH and ultrabroadband SC produces the f-3f interference pattern, which could be readily applied for CEP stability measurements.

4.2 Supercontinuum generation in the regime of anomalous GVD

The experiment was performed using 20-fs, CEP-stable pulses with central wavelength of 2 µm from a optical parametric amplifier described in Sect. 3.3.4. The output from the OPA was suitably attenuated and focused by an $f = +100$ mm lens into a 70 µm FWHM spot size located at the input face of the nonlinear medium. We tested four different nonlinear wide

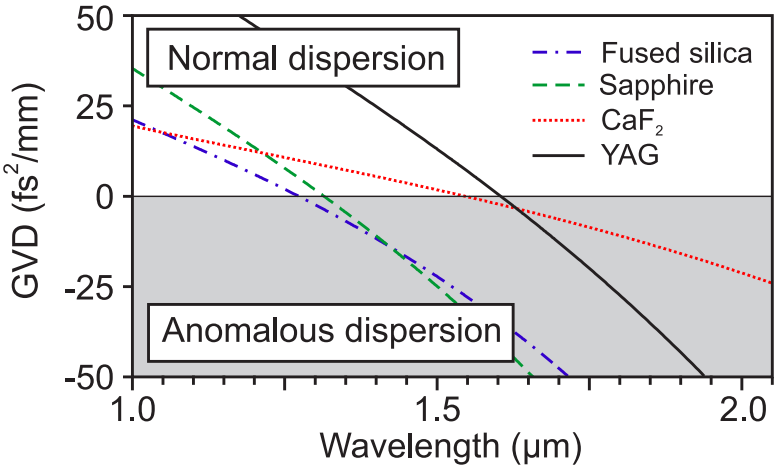

Figure 4.1: Group velocity dispersion curves for fused silica, sapphire, CaF_2 and YAG, as calculated using Sellmeier equations provided in [109].

bandgap materials, which are commonly used for SC generation in the visible and near-infrared: sapphire (6 mm length), fused silica (5 mm), CaF_2 (6 mm), and YAG (6 mm), whose GVD curves are illustrated in Fig. 4.1. The output SC radiation was re-collimated and then collected into a fiber tip of the spectrometer. The measurements were performed using two calibrated fiber spectrometers AvaSpec-2048 and AvaSpec-NIR256-2.5 (Avantes), that covered effective wavelength ranges of $400-1100$ nm and $1-2.5$ µm, respectively. Figure 4.2 shows the angle-integrated SC spectra, as recorded using

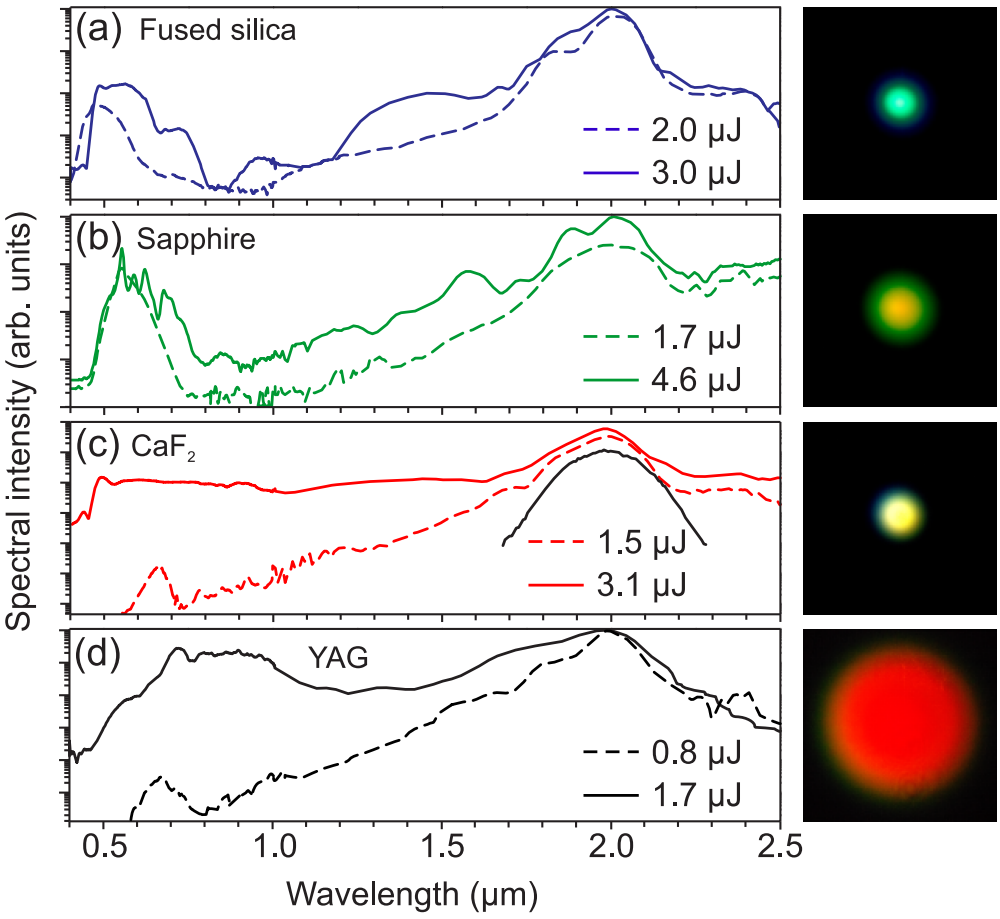

Figure 4.2: Supercontinuum spectra generated in (a) fused silica, (b) sapphire, (c) CaF_2, (d) YAG. The dashed and solid curves represent SC spectra in the transient and saturation regimes of the spectral broadening, respectively. The solid black curve in (c) illustrates the input-pulse spectrum. Curve labels stand for the input-pulse energy. Images on the right side show the corresponding far-field patterns of the SC emission in the visible range.

two different input-pulse energies, which roughly represent transient (lower energy) and saturated (higher energy) regimes of the spectral broadening. The highest values of the input-pulse energy in the latter case were chosen to be slightly below those produce periodic spectral modulation [132]

and/or apparent deterioration of the output beam profile. Note the distinct differences in SC spectral shapes, which demonstrate the importance of digression of the pump wavelength from the the zero GVD wavelength, as seen from Fig. 4.1. Also note the differences in visual appearance of characteristic coloring and angular divergence of the SC radiation, as illustrated by the screen shots of the far field patterns taken at 15 cm distance from the output face of the nonlinear media. The SC spectrum generated in fused silica [Fig. 4.2(a)] is very similar to those reported in a number of previous studies [122–125] and has a deep extended minimum around 1 µm and distinct intense peak in the visible (so-called blue peak), which then shows apparent red-shifted broadening with increase of the input-pulse energy. The SC spectrum with very similar spectral features is generated in sapphire [Fig. 4.2(b)], which exhibits essentially similar dispersive characteristics and nonlinearity as fused silica. In CaF_2, owing to its generally low dispersion, a broad and flat SC spectrum that spans from 450 nm to > 2.5 µm was generated [Fig. 4.2(c)], with the longest wavelength being limited by our detection apparatus. And finally, in YAG, a smooth SC spectrum with elevated spectral intensity in the 600-1000 nm range [Fig. 4.2(d)] was generated using quite low input-pulse energy owing to high nonlinearity of YAG as compared to other materials tested.

In all examined cases, prior to SC generation and in the transient regime of spectral broadening a characteristic TH peak centered at 660 nm was observed. In the transient regime of spectral broadening, the TH peak is best visible in CaF_2 and YAG [see. Fig. 4.2(c) and (d)], whereas in fused silica and sapphire it becomes rapidly masked by the occurrence of a strong and broad blue-shifted peak, which coincides with the X-wave phase matching [133] and which is not associated with TH generation.

4.3 Intrinsic third harmonic generation

The TH generation occurs at lower input pulse energy and is clearly observed before the onset of spectral broadening and SC generation. For example, the TH radiation is detected with 1.0 µJ input-pulse in fused silica and with 0.40 µJ input-pulse in YAG, and measured TH efficiency varies from 10^{-6} to 10^{-4}, depending on the input-pulse energy. A closer inspection of stand-alone TH spectra revealed a remarkable fast periodic modulation, whose frequency changes with the nonlinear material and its

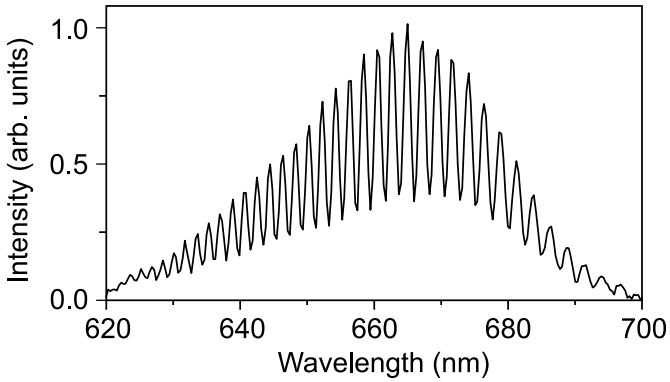

Figure 4.3: Spectrum of the third harmonic radiation.

length, as verified by testing shorter samples of the nonlinear media. An example of TH spectrum generated at 0.75 µJ input energy in YAG is shown in Fig. 4.3 [note linear intensity scale, in contrast to logarithmic scale in Fig. 4.2(d)]; also see Fig. 4.6(a), which shows the TH spectrum in fused silica. Interestingly, very similar modulation of the TH spectrum was observed in semiconductor materials using intense 3.5 µm pulses and was attributed to pulse splitting effect, however without providing more details [134].

In what follows, we show that distinct spectral modulation is a signature of a double-peaked TH pulse, which occurs naturally, without the splitting of the input pulse. We interpret our results in the framework of phase

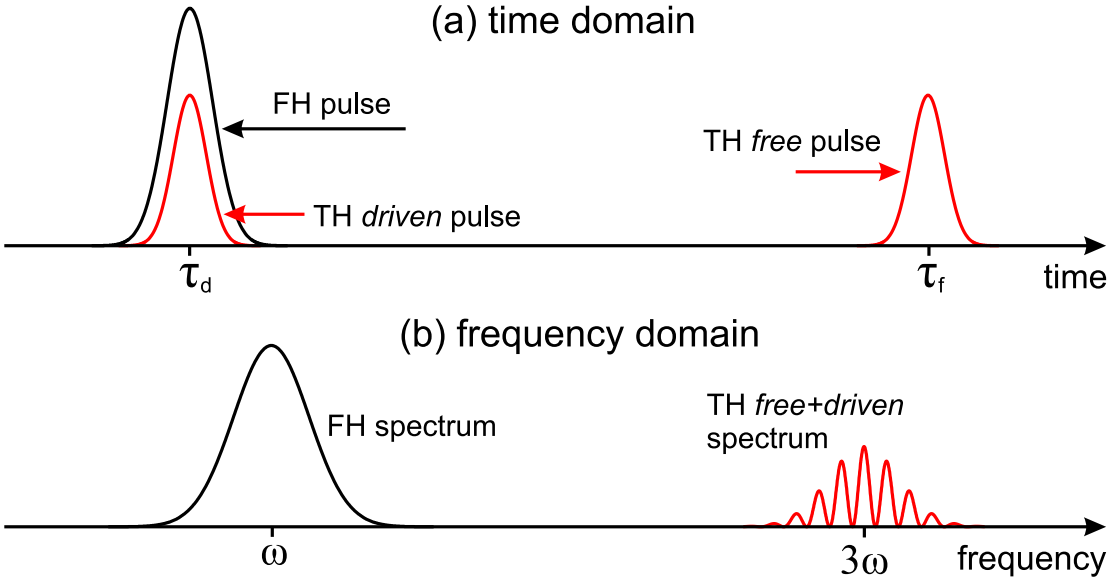

Figure 4.4: Schematic representation of third harmonic generation in the regime of large phase and group-velocity mismatch. (a) shows fundamental and third harmonics pulses in the time domain and (b) in the frequency domain.

and group-velocity mismatched second harmonic generation in media with

quadratic nonlinearity [135]. Such an operating condition imposes that TH radiation consists of two pulses, representing so-called *free* and *driven* waves, which produce spectral beating at the output [136] as schematically shown in Fig. 4.4. The first pulse, i.e. the *free* wave travels with the group velocity u_f, as set by the material dispersion, and walks-off from the pump pulse, i.e. the input-pulse at fundamental frequency. The second pulse, the *driven* wave, travels with the group velocity u_d of the nonlinear polarization, i.e. with the group velocity of the fundamental frequency pulse. Consequently, TH radiation at the output of the nonlinear medium consists of two pulses separated in time by the amount $\tau = |\nu_{\text{fd}}|z$, where $\nu_{\text{fd}} = 1/u_f - 1/u_d$ is the group velocity mismatch and z is the medium length. Inserting the relevant values of YAG: $z = 6$ mm and $\nu_{\text{fd}} = 115$ fs/mm, the estimated temporal separation between the *free* and *driven* TH pulses thus is 690 fs, which is very close to that of 670 fs, as retrieved by taking a Fourier transform of the fringe pattern shown in Fig. 4.3. In the spectral domain, the TH interference pattern can be expressed as:

$$S_f(\omega) + S_d(\omega) + 2\sqrt{S_f(\omega)S_d(\omega)}\cos(\phi_f - \phi_d + \omega(\tau_f - \tau_d)),$$

where $S_f(\omega)$ and $S_d(\omega)$ are the spectra of *free* and *driven* pulses and $\Delta\phi = \phi_f - \phi_d$ denotes the instant phase difference between the *free* and *driven* TH pulses. The fringe pattern shown in Fig. 4.5(a) is thus regarded as 3f-3f

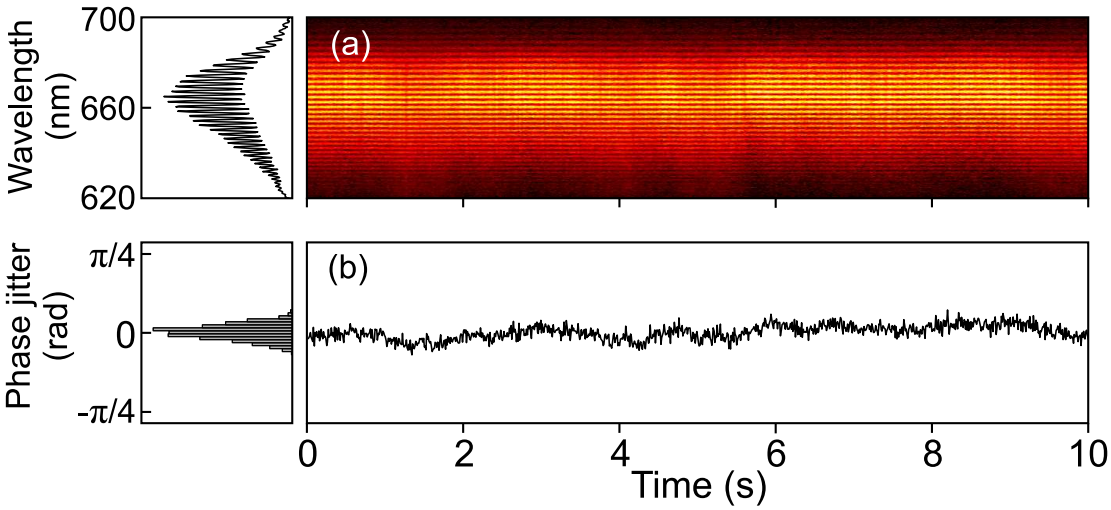

Figure 4.5: (a) 3f-3f interference pattern and its average, (b) variation of the phase $\Delta\phi$ over time and its statistics.

interferogram. Figure 4.5(a) shows a series of 1000 3f-3f interferograms, whose fringes are remarkably stable in time. The extracted phase $\Delta\phi$ jitter is plotted in Fig. 4.5(b) indicating a rms fluctuations of 48 mrad, which is

attributed to intensity fluctuations of the pump.

4.4 Measurements of CEP fluctuations from the beating between supercontinuum and third harmonic spectra

Finally, we experimentally demonstrate the practical use of intrinsic TH generation, as the observed spectral beating between SC and TH directly produces the f-3f interferogram, whose time series readily provide the statistics of CEP fluctuations. Although the TH component due to its low intensity ceases to be directly visible in the angle-integrated SC spectra in the saturation regime of spectral broadening (see the SC spectra measured at higher input-pulse energy in Fig. 4.2), filtering out the conical components of the SC reveals the presence of TH that propagates on the beam axis. We have verified experimentally that the spectral beating is more or less well-detectable in all investigated media, see examples of spectra in fused silica and YAG shown in Fig. 4.6.

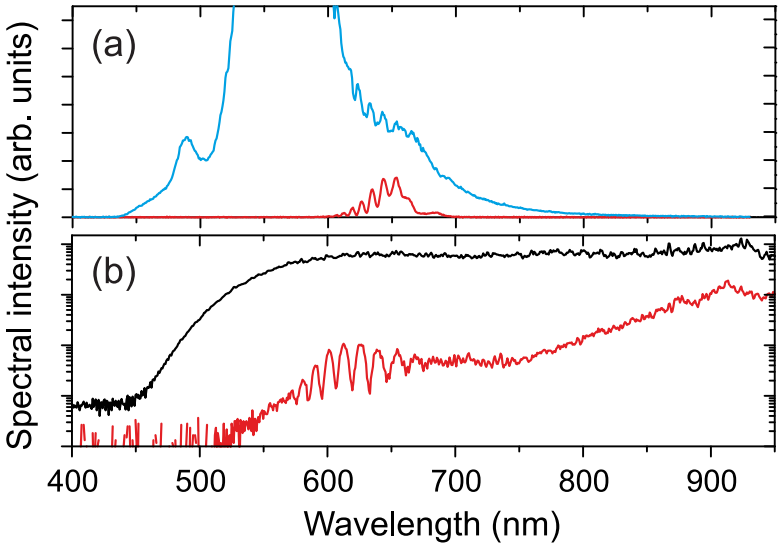

Figure 4.6: Visible and near-infrared part of the supercontinuum generated in (a) fused silica and (b) YAG. In (a) red and blue curves show the stand-alone TH and filtered part of the SC blue peak, respectively. In (b) black and red curves denote angle-integrated and filtered SC spectra, respectively. Note linear and logarithmic scales used for data in fused silica and YAG, respectively, and emerging modulation in the filtered SC spectra as due to spectral beating between SC and TH in the regime of spectral superbroadening.

Taking the SC generation in YAG as an example, we devised a setup, which simultaneously measures f-3f and, for a comparison, a more conven-

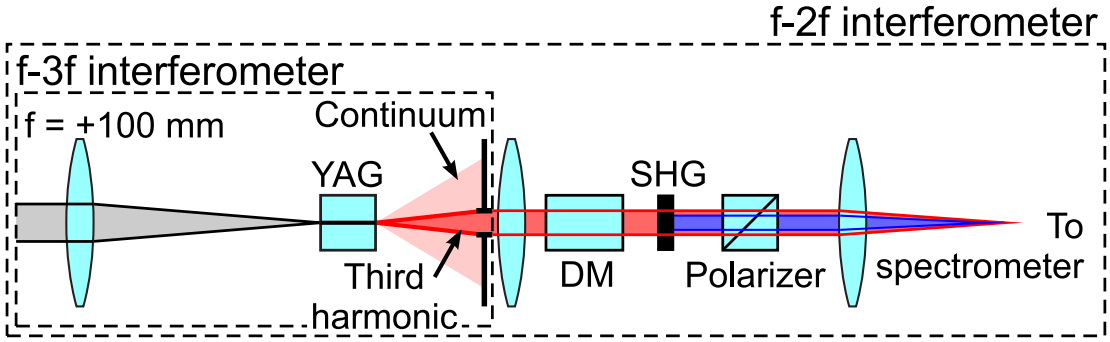

Figure 4.7: A setup for simultaneous measurement of f-3f and f-2f interferograms. DM is the dispersive medium, SHG is the second harmonic generator.

tional f-2f interferogram (Fig. 4.7). Specifically, the f-3f interferogram was recorded after careful filtering out the conical part of the SC by placing 1-mm iris aperture at 5 cm distance from the output face of YAG crystal. A conventional f-2f interferometer consisted of a collimating lens, bulk dispersive medium (DM, 25-mm-long YAG slab), which introduces the necessary delay between the spectral components of the SC (namely, between those located at 2 µm and 1 µm), the SH generator (SHG, 0.5-mm-thick BBO crystal cut for type I phase matching) and a polarizer. The resulting interference pattern is shown in Fig. 4.8(a), where shaded areas mark the interference fringes around 1 µm and 660 nm, generated by sampling the SC pulse with the SH and TH pulses, respectively. Fig. 4.8(b) shows

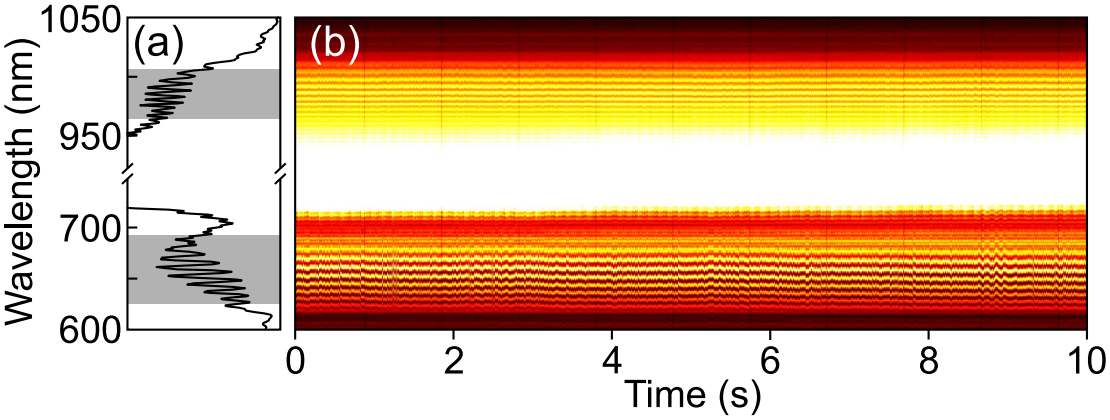

Figure 4.8: Measurement of CEP fluctuations of the pump pulse: (a) spectrogram averaged from 1000 single-shot spectra, (b) variation of f-2f and f-3f interference patterns in time.

variation of the interference pattern over 10 s period after recording 1000 single-shot spectrograms. The f-2f interference pattern yields SC pulse CEP rms fluctuations of 300 mrad.

The f-3f interference pattern is more complex and is the superposition of

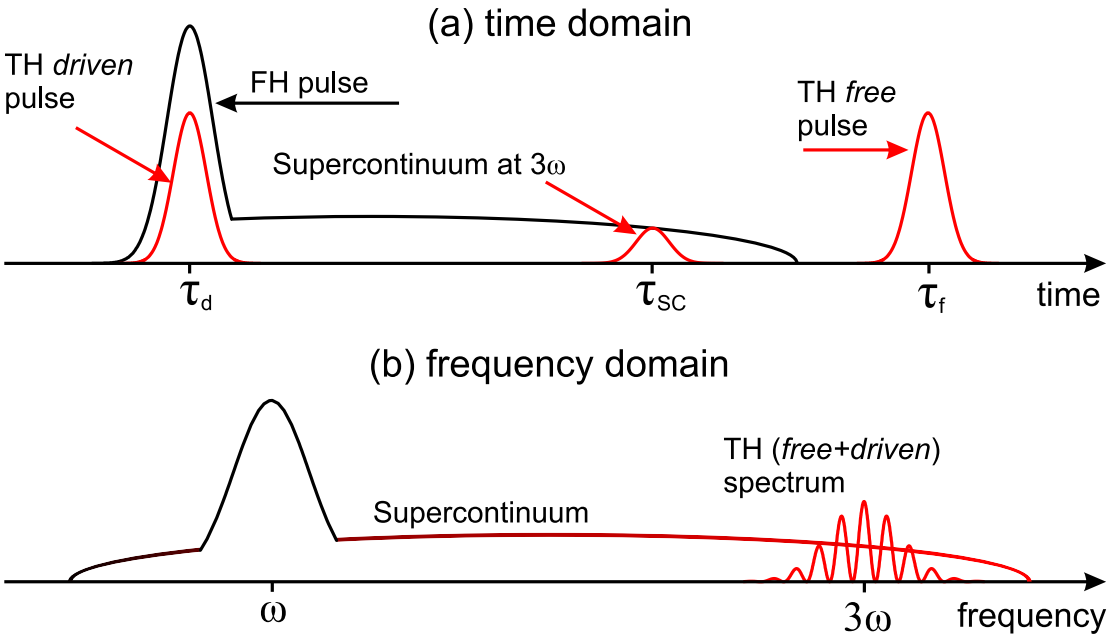

Figure 4.9: Schematic representation of simultaneous third harmonic and supercontinuum generation in the regime of large phase and group-velocity mismatch. (a) shows spercontinuum, fundamental and third harmonics pulses in the time domain and (b) in the frequency domain.

supercontinuum, *free* and *driven* pulses electric fields represented in spectral domain as depicted in Fig. 4.9. The spectrum around frequency 3ω therefore can be expressed as:

$$\begin{aligned} S(\omega) &= S_f(\omega) + S_d(\omega) + S_{SC}(\omega) + \\ &2\sqrt{S_f(\omega)S_d(\omega)}\cos(\phi_f - \phi_d + \omega(\tau_f - \tau_d)) + \\ &2\sqrt{S_f(\omega)S_{SC}(\omega)}\cos(\phi_f - \phi_{SC} + \omega(\tau_f - \tau_{SC})) + \\ &2\sqrt{S_d(\omega)S_{SC}(\omega)}\cos(\phi_d - \phi_{SC} + \omega(\tau_d - \tau_{SC})). \end{aligned} \tag{4.1}$$

In this case, the Fourier transform $D(t)$ of the measured spectrum $S(\omega)$ is composed of seven peaks, as schematically illustrated in Fig. 4.10(a). Application of arbitrary amplitude filters on the particular peaks (shown as shaded areas) delivers information on phase fluctuations. The farthest peaks at ±640 fs (labelled as 3f-3f) yield phase jitter of 55 mrad, which is attributed to the phase fluctuations between *free* and *driven* TH pulses. The remaining peaks at ±170 fs and ±470 fs (labelled as f-3f) provide CEP fluctuations of 315 mrad and 275 mrad, which are attributed to phase jitters between the SC pulse and *free* and *driven* TH pulses, respectively. Figure 4.10(b) shows the extracted CEP jitter between *free* TH pulse and SC (red solid curve), *driven* pulse and SC (blue dashed curve), second harmonic

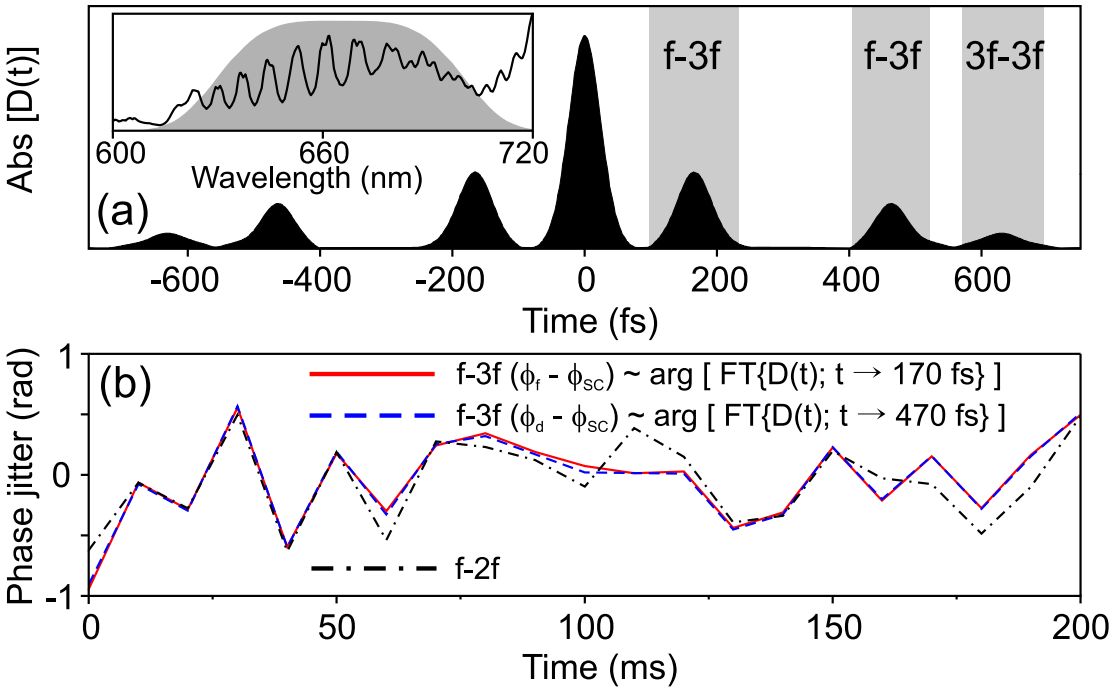

Figure 4.10: (a) An inverse Fourier transform (absolute value) of the of the spectrogram around 660 nm, which is shown enlarged in the inset. (b) show statistics of the retrieved phase jitter between *free* pulse and SC (red solid curve), *driven* pulse and SC (blue dashed curve), second harmonic and SC (black dash-dot curve).

and SC (black dash-dot curve), as measured over the period of 200 ms. A correlation between f-3f and conventional f-2f interferometry is clearly visible and indicates, that both f-3f and f-2f interferometers are measuring the same physical quantity, i.e. CEP fluctuations of the pump pulse.

In conclusion, we demonstrated ultrabroadband SC generation by filamentation of 20 fs, CEP-stable pulses at 2 µm in wide-bandgap solids: sapphire, fused silica, CaF_2, and YAG, in the regime of anomalous GVD. The measured SC spectra span from 450 nm to more than 2.5 µm and their particular shapes crucially depend on digression of the pump wavelength from the the zero GVD wavelength. In that regard, CaF_2 and YAG provide the SC radiation with the smoothest spectral coverage across the entire detected spectral range. We also detect TH generation, which occurs prior to spectral superbroadening. Periodic modulation of the TH spectrum reveals a double-peaked temporal structure of the TH pulse, consisting of *free* and *driven* components, which are generated in the regime of large phase and group-velocity mismatch. We find, that double-peaked TH structure persists also in the regime of spectral superbroadening and coexists with strong

SC emission. We also devised an experimental setup, which simultaneously measures the CEP stability of the SC pulses by means of f-2f and f-3f interferometry. Given a good agreement between the results obtained by f-2f and f-3f methods, the f-3f interferometry based on intrinsic TH generation, suggests a simple and straightforward method to measure CEP fluctuations, despite rather complex temporal structure of the TH pulse.

Main results and conclusions

1. We have demonstrated efficient frequency conversion of ultrashort laser pulses in the ultraviolet by means of phase-matched four-wave mixing in transparent bulk solids with Kerr nonlinearity. The key point in realizing efficient four-wave interactions in isotropic media relies on fulfillment of the noncollinear phase matching condition using cylindrical beam focusing geometry. Under these settings, parametric amplification can be performed with high energy (milijoule) pump pulses, at the same time keeping the laser beam intensity reasonably below the optical damage threshold of the nonlinear medium.

2. The efficient generation of UV harmonics of the Nd:glass laser by means of four-wave difference frequency mixing was demonstrated. Specifically, third-harmonic at 351 nm in fused silica (with 15% energy conversion efficiency), fifth-harmonic at 211 nm in MgF_2 crystals (with 10% energy conversion efficiency) and sixth harmonic at 176 nm in MgF_2 (>1% energy conversion efficiency) were obtained.

3. We have demonstrated a broadband four-wave optical parametric amplifier, which might support 7.5 fs ultraviolet pulses at 330 nm. The developed analytical model reveals, that parametric gain bandwidth broadening during four-wave optical parametric amplification is resulted by self- and cross-phase modulation effects imposed by the intense pump wave.

4. Visible-to-ultraviolet frequency conversion method based on chirped-pulse four-wave optical parametric amplification in fused silica was demonstrated. The proposed setup produces ∼30 fs, 10 µJ energy pulses at 310 nm.

5. Noncollinear four-wave optical parametric amplifier based on fused silica, which provides sub-30 fs pulses tunable in the near-infrared ($1.1 - 1.5$ µm) spectral range was demonstrated.

6. It is demonstrated, that efficient DFG and OPA processes can occur at the same time in a single type I BBO crystal if simultaneously pumped at 800 nm and visible (570–630 nm) spectral range. The proposed setup delivers up to 26 µJ energy, ∼30 fs pulses tunable in 1.1–2.8 µm wavelength range.

7. 800 nm pumped noncolliner optical parametric amplifier based on type I BBO crystal provides broad phase matching bandwidth if seeded by pulses in the 1.6–2.8 µm spectral range. As an experimental proof, 15 fs, 15 µJ energy pulses at 2 µm central wavelength, with CEP stability of 330 mrad were generated.

8. We demonstrated the generation of ultrabroadband supercontinuum in fused silica, sapphire, CaF_2 and YAG, using 20 fs pulses at 2 µm. The SC spectra extend from 450 nm to more than 2500 nm, and their particular shapes depend on dispersive properties of the materials, specifically on the GVD zero wavelength. In that regard, CaF_2 and YAG provide the SC radiation with the smoothest spectrum across the entire detected spectral range.

9. Prior to supercontinuum spectral super-broadening, we observe intrinsic third harmonic generation, which occurs in the condition of large phase and group velocity mismatch and consists of *free* and *driven* components. The observed spectral beating between SC and TH directly produces the f-3f interferogram, whose time series readily provide the statistics of CEP fluctuations, as simultaneously measured by f-2f and f-3f interferometers.

Appendix I: Optical layout of Topas-White

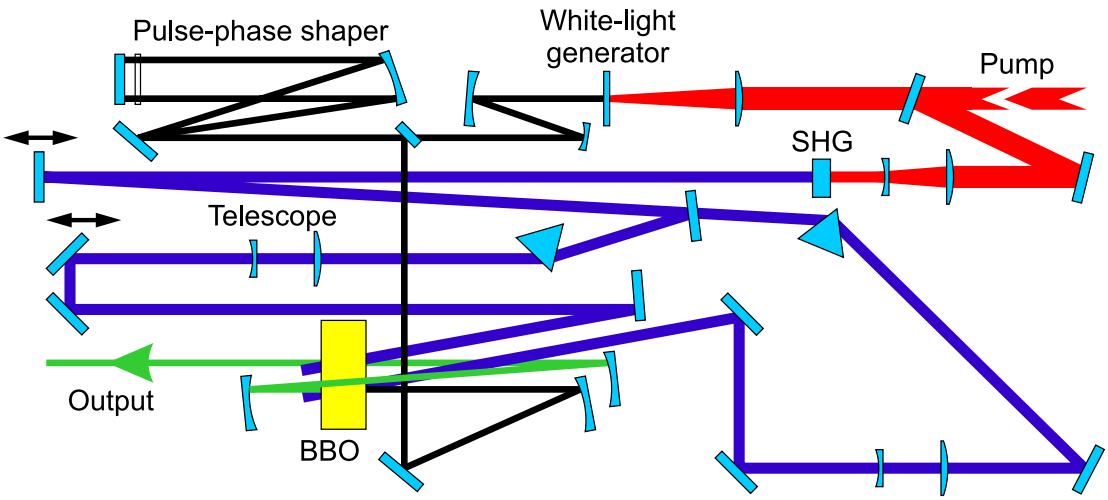

Figure 4.11: Optical layout of NOPA Topas-White

The Topas-White (Light Conversion Ltd.) is a two-stage noncollinear optical parametric amplifier of white light continuum [79]. The way of operation is as follows (see Fig. 4.11). A small fraction of the incoming 800 nm pulse is used to produce white light continuum in a sapphire plate. The white light beam is collimated using chromatic aberration free, low astigmatism collimator. Then the pulse is sent into a double pass negative dispersion pulse phase shaper consisting of a diffraction grating, a spherical mirror, a folding mirror and a phase mask. Dispersion of this pulse shaper is calculated in order to achieve an adapted chirp of the seed pulse such that: first, the desired bandwidth fits under the pump pulse; secondly, the amplified signal pulse is compressed to the transform limit using material dispersion of fused silica or other material. In addition, the pulse shaper allows controlling the pulse spectrum: by placing a mask in front of the folding mirror one can clip off unwanted spectral components such as residual 800 nm, or narrow the bandwidth. After passing the stretcher, the seed pulse is fed into the preamplifier stage. The maximum bandwidth that can be amplified is from 530 nm to 720 nm. In the power-amplifier stage, the signal beam is overlapped within the same nonlinear crystal with the main pump beam. After the power-amplifier stage, the beam is collimated using a mirror telescope. The relevant output characteristics of the particular amplifier used in the experiments: tuning range 530-720 nm; pulse duration $\geq$10 fs at FWHM; pulse energy – up to 10 µJ.

Bibliography

[1] O. Isaienko and E. Bourget, Ultra-broadband sum-frequency vibrational spectrometer of aqueous interfaces based on a non-collinear optical parametric amplifier, Opt. Express, **20**, 547–561 (2012).

[2] D. Brida, C. Manzoni, G. Cirmi, D. Polli, and G. Cerullo, Tracking ultrafast energy flow in molecules using broadly tunable few-optical-cycle pulses, IEEE J. Select. Topics Quantum Electron, **18**, 329–339 (2012).

[3] C. Manzoni, D. Polli, and G. Cerullo, Two-color pump-probe system broadly tunable over the visible and the near infrared with sub-30 fs temporal resolution, Rev. Sci. Instr., **77**, 023103 (2006).

[4] R. Danielius, A. Piskarskas, A. Stabinis, G.P. Banfi, P.Di Trapani, R. Righini, Traveling-wave parametric generation of widely tunable, highly coherent femtosecond light pulses, J. Opt. Soc. Am. B, **10**, 2222–2232 (1993).

[5] M.H. Dunn, M. Ebrahimzadeh, Parametric generation of tunable light from continuous-wave to femtosecond pulses, Science, **286**, 1513–1517 (1999).

[6] G. Cerullo and S. De Silvestri, Ultrafast optical parametric amplifiers, Rev. Sci. Instr., **74**, 1–18 (2003).

[7] P. Tzankov, T. Fiebig, and I. Buchvarov, Tunable femtosecond pulses in the near-ultraviolet from ultrabroadband parametric amplification, Appl. Phys. Lett., **82**, 517–519 (2003).

[8] G. Kurdi, K. Osvay, M. Csatari, I.N. Ross, J. Klebnitzki, Optical parametric amplification of femtosecond ultraviolet laser pulses, IEEE J. Select. Topics Quantum Electron, **10**, 1259–1267 (2004).

[9] T. Fiebig, K. Stock, S. Lochbrunner, and E. Riedle, Femtosecond charge transfer dynamics in artificial donor/acceptor systems: switching from adiabatic to nonadiabatic regimes by small structural changes, Chem. Phys. Lett., **345**, 81–88 (2001).

[10] P. Baum, S. Lochbrunner, and E. Riedle, Tunable sub-10-fs ultraviolet pulses generated by achromatic frequency doubling, Opt. Lett., **29**, 1686–1688 (2004).

[11] S. Backus, J. Peatross, Z. Zeek, A. Rundquist, G. Taft, M.M. Murnane, and H.C. Kapteyn, 16-fs, 1-µJ ultraviolet pulses generated by third-harmonic conversion in air, Opt. Lett., **21**, 665–667 (1996).

[12] C.G. Durfee III, S. Backus, M.M. Murnane, and H.C. Kapteyn, Ultrabroadband phase-matched optical parametric generation in the ultraviolet by use of guided waves, Opt. Lett., **22**, 1565–1567 (1997).

[13] F. Théberge, N. Aközbek, W. Liu, A. Becker, and S.L. Chin, Tunable ultrashort laser pulses generated through filamentation in gases, Phys. Rev. Lett., **97**, 023904 (2006).

[14] A.E. Jailaubekov, and S.E. Bradforth, Tunable 30-femtosecond pulses across the deep ultraviolet, Appl. Phys. Lett., **87**, 021107 (2005).

[15] C.G. Durfee III, S. Backus, H.C. Kapteyn, and M.M. Murnane, Intense 8-fs pulse generation in the deep ultraviolet, Opt. Lett., **24**, 697–699 (1999).

[16] T. Fuji, T. Horyo, and T. Suzuki, Generation of 12 fs deep-ultraviolet pulses by four-wave mixing through filamentation in neon gas, Opt. Lett., **32**, 2481–2483 (2007).

[17] K. Kosma, S.A. Trushin, W.E. Schmid, and W. Fuss, Vacuum ultraviolet pulses of 11 fs from fifth-harmonic generation of a Ti:sapphire laser, Opt. Lett., **33**, 723–725 (2008).

[18] A. Penzkofer and H.J. Lehmeier, Theoretical investigation of noncollinear phase-matched parametric four-photon amplification of ultrashort light pulses in isotropic media, Opt. Quantum Electron., **25**, 815–844 (1993).

[19] H. Crespo, J.T. Mendonça, and A. Dos Santos, Cascaded highly nondegenerate four-wave-mixing phenomenon in transparent isotropic condensed media, Opt. Lett., **25**, 829–831 (2000).

[20] H.K. Nienhuys, P.C.M. Planken, R.A. van Santen, and H.J. Bakker, Generation of mid-infrared pulses by $\chi^{(3)}$ difference frequency generation in CaF_2 and BaF_2, Opt. Lett., **26**, 1350–1352 (2001).

[21] S. Woutersen, U. Emmerichs, and H. Bakker, Femtosecond mid-IR pump-probe spectroscopy of liquid water: Evidence for a two-component structure, Science, **278**, 658–660 (1997).

[22] A. Baltuška, Th. Udem, M. Uiberacker, M. Hentschel, E. Goulielmakis, Ch. Gohle, R. Holzwarth, V.S. Yakovlev, A. Scrinzi, T.W. Hünsch, and F. Krausz, Attosecond control of electronic processes by intense light fields, Nature, **421**, 611–615 (2003).

[23] G. Sansone, E. Benedetti, F. Calegari, C. Vozzi, L. Avaldi, R. Flammini, L. Poletto, P. Villoresi, C. Altucci, R. Velotta, S. Stagira, S. De Silvestri, and M. Nisoli, Isolated single-cycle attosecond pulses, Science, **20**, 443–446 (2006).

[24] G.G. Paulus, F.Grasbon, H. Walther, P. Villoresi, M. Nisoli, S. Stagira, E. Priori, and S. De Silvestri, Absolute-phase phenomena in photoionization with few-cycle laser pulses, Nature, **414**, 182–184 (2001).

[25] A. Couairon and A. Mysyrowicz, Femtoseconmd filamentation in transparent media, Phys. Rep., **441**, 47–189 (2007).

[26] D. Brida, C. Manzoni, G. Cirmi, M. Marangoni, S. De Silvestri, and G. Cerullo, Generation of broadband mid-infrared pulses from an optical parametric amplifier, Opt. Express, **15**, 15035–15040 (2007).

[27] O. Chalus, A. Thai, P. K. Bates, and J. Biegert, Six-cycle mid-infrared source with 3.8 µJ at 100 khz, Opt. Lett., **35**, 3204–3206 (2010).

[28] Y. Deng, A. Schwarz, H. Fattahi, M. Ueffing, X. Gu, M. Ossiander, T. Metzger, V. Pervak, H. Ishizuki, T. Taira, T. Kobayashi, G. Marcus, F. Krausz, R. Kienberger, and N. Karpowicz, Carrier-envelope-phase-stable, 1.2 mJ, 1.5 cycle laser pulses at 2.1 µm, Opt. Lett., **37**, 4973–4975 (2012).

[29] T. Fuji and T. Suzuki, Generation of sub-two-cycle mid-infrared pulses by four-wave mixing through filamentation in air, Opt. Lett., **32**, 3330–3332 (2007).

[30] D. Faccio, A. Grün, P. K. Bates, O. Chalus, and J. Biegert, Optical amplification in the near-infrared in gas-filled hollow-core fibers, Opt. Lett., **34**, 2918–2920 (2009).

[31] L. Bergé, Self-compression of 2 µm laser filaments, Opt. Express, **16**, 21529–21543 (2008).

[32] H. Okamoto and M. Tatsumi, Generation of ultrashort light pulses in the mid-infrared (3000-800 cm^{-1}) by four-wave mixing, Opt. Commun., **121**, 63–68 (1995).

[33] E. Riedle, M. Beutter, S. Lochbrunner, J. Piel, S. Schenkl, S. Spörlein, W. Zinth, Generation of 10 to 50 fs pulses tunable through all of the visible and the NIR, Appl. Phys. B, **71**, 457–465 (2000).

[34] R.W. Boyd, Nonlinear Optics, Academic Press, San Diego, 3rd edition (2008).

[35] J.A. Giordmaine, Mixing of light beams in crystals, Phys. Rev. Lett., **8**, 19–20 (1962).

[36] M.V. Hobden and J. Warner, The temperature dependence of the refractive indices of pure lithium niobate, Phys. Lett., **22**, 243–244 (1966).

[37] M.M. Fejer, G.A. Magel, D.H. Jundt, R.L. Byer, Quasi-phase-matched second harmonic generation: tuning and tolerances, IEEE J. Quantum Electron., **28**, 2631–2654 (1992).

[38] S.A. Akhmanov, V.A. Vysloukh, and A.S. Chirkin, Optics of Femtosecond Laser Pulses, American Institute of Physics, New York (1992).

[39] G.M. Gale, M. Cavallari, T.J. Driscoll, and F. Hache, Sub-20-fs tunable pulses in the visible from an 82-MHz optical parametric oscillator, Opt. Lett., **20**, 1562–1564 (1995).

[40] P.B. Corkum, Plasma perspective on strong field multiphoton ionization, Phys. Rev. Lett., **71**, 1994–1997 (1993).

[41] D.J. Jones, S.A. Diddams, J.K. Ranka, A. Stentz, R.S. Windeler, J.L. Hall, and S.T. Cundiff, Carrier-envelope phase control of femtosecond mode-locked lasers and direct optical frequency synthesis, Science, **28**, 635–639 (2000).

[42] A. Baltuška, T. Fuji, and T. Kobayashi, Controlling the carrier-envelope phase of ultrashort light pulses with optical parametric amplifiers, Phys. Rev. Lett., **88**, 133901 (2002).

[43] T. Fuji, A. Apolonski, and F. Krausz, Self-stabilization of carrier-envelope offset phase by use of difference-frequency generation, Opt. Lett., **29**, 632–634 (2004).

[44] C. Manzoni, G. Cerullo, and S. De Silvestri, Ultrabroadband self-phase-stabilized pulses by difference-frequency generation, Opt. Lett., **29**, 2668–2670 (2004).

[45] M. Kakehata, H. Takada, Y. Kobayashi, K. Torizuka, Y. Fujihira, T. Homma, and H. Takahashi, Single-shot measurement of carrier-envelope phase changes by spectral interferometry, Opt. Lett., **26**, 1436–1438 (2001).

[46] M. Takeda, H. Ina, and S. Kobayashi, Fourier-transform method of fringe-pattern analysis for computer-based topography and interferometry, J. Opt. Soc. Am., **72**, 156–160 (1982).

[47] I.V. Hertel and V. Radloff, Ultrafast dynamics in isolated molecules and molecular clusters, Rep. Prog. Phys., **69**, 1897–2003 (2006).

[48] J.H. Klein-Wiele, J. Bekesi, and P. Simon, Sub-micron patterning of solid materials with ultraviolet femtosecond pulses, Appl. Phys. A, **79**, 775–778 (2004).

[49] I. Zergioti, A. Karaiskou, D.G. Papazoglou, C. Fotakis, M. Kaspetaki, and D. Kefetzopoulos, Femtosecond laser microprinting of biomaterials, Appl. Phys. Lett., **86**, 163902 (2005).

[50] A.I. Kalachev, D.N. Nikogosyan, and G. Brambilla, Long-period fiber grating fabrication by high-intensity femtosecond pulses at 211 nm, J. Lightwave Technol., **23**, 2568–2578 (2005).

[51] I. Zergioti, K.D. Kyrkis, D.G. Papazoglou, and S. Tzortzakis, Structural modifications in fused silica induced by ultraviolet fs laser filaments, Appl. Surf. Sci., **253**, 7865–7868 (2007).

[52] V. Zorba, N. Boukos, I. Zergioti, and C. Fotakis, Ultraviolet femtosecond, picosecond and nanosecond laser microstructuring of silicon: structural and optical properties, Appl. Opt., **47**, 1846–1850 (2008).

[53] L. Misoguti, S. Backus, C.G. Durfee, R. Bartels, M.M. Murnane, and H.C. Kapteyn, Generation of broadband VUV light using third-order cascaded processes, Phys. Rev. Lett., **87**, 013601 (2001).

[54] L. Bergé and S. Skupin, Sub-2 fs pulses generated by self-channeling in the deep ultraviolet, Opt. Lett., **33**, 750–752 (2008).

[55] U. Graf, M. Fiess, M. Schultze, R. Kienberger, F. Krausz, and E. Goulielmakis, Intense few-cycle light pulses in the deep ultraviolet, Opt. Express, **16**, 18956–18963 (2008).

[56] R.V. Volkov, D.V. Khakhulin, and A.B. Savel'ev, Fourwave parametric conversion of femtosecond laser pulse in a filament induced in a solid target, Opt. Lett., **33**, 666–668 (2008).

[57] J. Liu and T. Kobayashi, Cascaded four-wave mixing and multicolored arrays generation in a sapphire plate by using two crossing beams of femtosecond laser, Opt. Express, **16**, 22119–22125 (2008).

[58] P.S. Banks, M.D. Feit, and M.D. Perry, High-intensity third-harmonic generation in beta barium borate through second-order and third-order susceptibilities, Opt. Lett., **24**, 4–6 (1999).

[59] J.P. Fève, B. Boulanger, and Y. Guillien, Efficient energy conversion for cubic third-harmonic generation that is phase matched in $KTiOPO_4$, Opt. Lett., **25**, 1373–1375 (2000).

[60] A. Penzkofer, J. Kraus, and J. Sperka, Noncollinear phase matched four photon frequency mixing in water, Opt. Commun., **37**, 437–441 (1981).

[61] G. Mao, Y. Wu, and K.D. Singer, Third harmonic generation in self-focused filaments in liquids, Opt. Express, **15**, 4857–4862 (2007).

[62] A. Dubietis, G. Tamošauskas, P. Polesana, G. Valiulis, H. Valtna, D. Faccio, P. Di Trapani, and A. Piskarskas, Highly efficient four-wave parametric amplification in transparent bulk Kerr medium, Opt. Express, **15**, 11126–11132 (2007).

[63] H. Valtna, A. Dubietis, G. Tamošauskas, P. Polesana, J. Galinis, D. Majus, G. Valiulis, D. Faccio, P. Di Trapani, and A. Piskarskas, Efficient four-wave parametric amplification and spatial soliton generation in transparent isotropic medium with Kerr nonlinearity, Lithuanian J. Phys., **47**, 403–410 (2007).

[64] S.E. Harris and R.B. Miles, Proposed third-harmonic generation in phase-matched metal vapors, Appl. Phys. Lett., **19**, 385 (1971).

[65] G.C. Bjorklund, Effects of focusing on third-order nonlinear processes in isotropic media, IEEE J. Quantum Electron., **11**, 287–296 (1975).

[66] D.N. Nikogosyan, Properties of Optical and Laser-Related Materials, John Wiley & Sons, Chichester (1997).

[67] M. Bass, E.W. Van Stryland, D.R. Williams, and W.L. Wolfe, Handbook of Optics, McGraw-Hill Professional, New York, 2nd edition (1994).

[68] B.C. Stuart, M.D. Feit, S. Herman, A.M. Rubenchik, B.W. Shore, and M.D. Perry, Nanosecond-to-femtosecond laser-induced breakdown in dielectrics, Phys. Rev. B, **53**, 1749–1761 (1996).

[69] A. Dubietis, G. Tamošauskas, A. Varanavičius, and G. Valiulis, Two-photon absorbing properties of ultraviolet phase-matchable crystals at 264 and 211 nm, Appl. Opt., **39**, 2437–2440 (2000).

[70] F. Seifert, J. Ringling, F. Noack, V. Petrov, and O. Kittelmann, Generation of tunable femtosecond pulses to as low as 172.7 nm by sum-frequency mixing in lithium triborate, Opt. Lett., **19**, 1538–1540 (1994).

[71] V. Petrov, F. Noack, F. Rotermund, M. Tanaka, and Y. Okada, Sum-frequency generation of femtosecond pulses in $CsLiB_6O_{10}$ down to 175 nm, Appl. Opt., **39**, 5076–5079 (2000).

[72] V. Petrov, F. Rotermund, and F. Noack, Generation of femtosecond pulses down to 166 nm by sum-frequency mixing in $KB_5O_8{\cdot}4H_2O$, Electron. Lett., **34**, 1748–1750 (1998).

[73] L.D. Ziegler, J. Morais, Y. Zhou, S. Constantine, M.K. Reed, M.K. Steiner-Shepard, and D. Lommel, Tunable 50-fs pulse generation in the 250-310-nm ultraviolet range, IEEE J. Quantum Electron., **34**, 1758–1764 (1998).

[74] A. Kummrow, M. Wittmann, F. Tschirschwitz, G. Korn, and E.T.J. Nibbering, Femtosecond ultraviolet pulses generated using noncollinear optical parametric amplification and sum frequency mixing, Appl. Phys. B, **71**, 885–887 (2000).

[75] I.Z. Kozma, P. Baum, S. Lochbrunner, and E. Riedle, Widely tunable sub-30 fs ultraviolet pulses by chirped sum frequency mixing, Opt. Express, **11**, 3110–3115 (2003).

[76] Y. Nabekawa and K. Midorikawa, Group-delay-dispersion-matched sum-frequency mixing for the indirect phase control of deep ultraviolet pulses in the sub-20-fs regime, Appl. Phys. B, **78**, 569–581 (2004).

[77] B. Zhao, Y. Jiang, K. Sueda, N. Miyanaga, and T. Kobayashi, Sub-15 fs ultraviolet pulses generated by achromatic phase-matching sum-frequency mixing, Opt. Express, **17**, 17711–17714 (2009).

[78] M. Beutler, M. Ghotbi, F. Noack, D. Brida, C. Manzoni, and G. Cerullo, Generation of high-energy sub-20 fs pulses tunable in the 250-310 nm region by frequency doubling of a high-power noncollinear optical parametric amplifier, Opt. Lett., **34**, 710–712 (2009).

[79] TOPAS-white data sheet, Light Conversion Ltd., www.lightcon.com.

[80] M. Beutler, M. Ghotbi, F. Noack, and I.V. Hertel, Generation of sub-50-fs vacuum ultraviolet pulses by four-wave mixing in argon, Opt. Lett., **35**, 1491–1493 (2010).

[81] A. Dubietis, G. Jonušauskas, and A. Piskarskas, Powerful femtosecond pulse generation by chirped and stretched pulse parametric amplification in BBO crystal, Opt. Commun., **88**, 437–440 (1992).

[82] T.Q. Jia, H.X. Chen, M. Huang, F.L. Zhao, X.X. Li, S.Z. Xu, H.Y. Sun, D.H. Feng, C.B. Li, X.F. Wang, R.X. Li, Z.Z. Xu, X.K. He, and H. Kuroda, Ultraviolet-infrared femtosecond laser-induced damage in fused silica and CaF_2 crystals, Phys. Rev. B, **73**, 054105 (2006).

[83] P.B. Corkum and F. Krausz, Attosecond science, Nature Phys., **3**, 381–387 (2007).

[84] M. Nisoli, S. Stagira, S. De Silvestri, O. Svelto, G. Valiulis, A. Varanavičius, Parametric generation of high-energy 14.5-fs light pulses at 1.5 µm, Opt. Lett., **23**, 630–632 (1998).

[85] D.Brida, G. Cirmi, C. Manzoni, S. Bonora, P. Villoresi, S. De Silvestri, and G. Cerullo, Sub-two-cycle light pulses at 1.6 µm from an optical parametric amplifier, Opt. Lett., **33**, 741–743 (2008).

[86] D. Brida, C. Manzoni, G. Cirmi, M. Marangoni, S. Bonora, P. Villoresi, S. De Silvestri, and G. Cerullo, Few-optical-cycle pulses tunable from the visible to the mid-infrared by optical parametric amplifiers, J. Opt. A, **12**, 013001 (2010).

[87] E. Rubino, J. Darginavičius, D. Faccio, P. Di Trapani, A. Piskarskas, A. Dubietis, Generation of broadly tunable sub-30-fs infrared pulses by four-wave optical parametric amplification, Opt. Lett., **36**, 382–384 (2011).

[88] C. Vozzi, F. Calegari, E. Benedetti, S. Gasilov, G. Sansone, G. Cerullo, M. Nisoli, S. De Silvestri, and S. Stagira, Millijoule-level phase-stabilized few-optical-cycle infrared parametric source, Opt. Lett., **32**, 2957–2959 (2007).

[89] X. Gu, G. Marcus, Y. Deng, T. Metzger, C. Teisset, N. Ishii, T. Fuji, A. Baltuška, R. Butkus, V. Perval, H. Ishizuki, T. Taira, T. Kobayashi, R. Kienberger, and F. Krausz, Generation of carrier-envelope-phase-stable 2-cycle 740-µJ pulses at 2.1-µm carrier wavelength, Opt. Express, **17**, 62–69 (2008).

[90] G. Andriukaitis, T. Balčiūnas, S. Ališauskas, A. Pugžlys, A. Baltuška, T. Popmintchev, M.C. Chen, M.M. Murnane, and H.C. Kapteyn, 90 GW peak power few-cycle mid-infrared pulses from an optical parametric amplifier, Opt. Lett., **36**, 2755–2757 (2011).

[91] F. Silva, P.K. Bates, A. Esteban-Martin, M. Ebrahim-Zadeh, and J. Biegert, High-average-power, carrier-envelope phase-stable, few-cycle pulses at 2.1 µm from a collinear BiB_3O_6 optical parametric amplifier, Opt. Lett., **37**, 933–935 (2012).

[92] J. Liu, Y. Kida, T. Teramoto, and T. Kobayashi, Simultaneous compression and amplification of a laser pulse in a glass plate, Opt. Express, **18**, 2495–2502 (2010).

[93] O.D. Mücke, S. Ališauskas, A.J. Verhoef, A. Pugžlys, A.Baltuška, V. Smilgevičius, J. Pocius, L. Giniūnas, R. Danielius, and N. Forget, Self-compression of millijoule 1.5 µm pulses, Opt. Lett., **34**, 2498–2500 (2009).

[94] G. Cirmi, D. Brida, C. Manzoni, M. Marangoni, S. De Silvestri, and G. Cerullo, Few-optical-cycle pulses in the near-infrared from a noncollinear optical parametric amplifier, Opt. Lett., **32**, 2396–2398 (2007).

[95] O. Isaienko and E. Borguet, Genereation of ultrabroadband pulses in the near-IR by noncollinear optical parametric amlification in potassium titanyl phosphate, Opt. Express, **16**, 3949–3954 (2008).

[96] D. Brida, S. Bonora, C. Manzoni, M. Marangoni, P. Villoresi, S. De Silvestri, and G. Cerullo, Generation of 8.5-fs pulses at 1.3 µm for ultrabroadband pump-probe spectroscopy, Opt. Express, **17**, 12510–12515 (2009).

[97] O. Isaienko, E. Borguet, and P. Vöhringer, High-repetition-rate near-infrared noncollinear ultrabroadband optical parametric amplification in $KTiOPO_4$, Opt. Lett., **35**, 3832–3834 (2010).

[98] C. Vozzi, G. Cirmi, C. Manzoni, E. Benedetti, F. Calegari, G. Sansone, S. Stagira, O. Svelto, S.De Silvestri, M. Nisoli, and G. Cerullo, High-energy, few-optical-cycle pulses at 1.5 µm with passive carrier-envelope phase stabilization, Opt. Express, **14**, 10109–10116 (2006).

[99] N. Ishii,K. Kaneshima, K. Kitano,T. Kanai,S. Watanabe, J. Itatani, Sub-two-cycle, carrier-envelope phase-stable, intense optical pulses at 1.6 µm from a BiB_3O_6 optical parametric chirped-pulse amplifier, Opt. Lett., **37**, 4182–4184 (2012).

[100] M. Ghotbi, V. Petrov, and F. Noack, Broadly tunable, sub-30 fs near-infrared pulses from an optical paramtric amplifier based on BiB_3O_6, Opt. Lett., **35**, 2139–2141 (2010).

[101] C. Zhang, P. Wei, Y. Huang, Y. Leng, Y. Zheng, Z. Zeng, R. Li, and Z. Xu, Tunable phase-stabilized infrared optical parametric amplifier for high-order harmonic generation, Opt. Lett., **34**, 2730–2732 (2009).

[102] D.N. Nikogosyan, Nonlinear Optical Crystals, Springer, New York (2005).

[103] T. Fuji, N. Ishii, C.Y. Teisset, X. Gu, T. Metzger, A. Baltuška, N. Forget, D. Kaplan, A. Galvanauskas, and F. Krausz, Parametric amplification of few-cycle carrier-envelope phase-stable pulses at 2.1 µm, Opt. Lett., **31**, 1103–1105 (2006).

[104] C. Erny, L. Gallmann, and U. Keller, High-repetition-rate femtosecond optical parametric chirped-pulse amplifier in the mid-infrared, Appl. Phys. B, **96**, 257–269 (2009).

[105] K.Y. Hong, S.W. Huang, J. Moses, X. Fu, C.J. Lai, G. Cirmi, A. Sell, E. Granados, P. Keathley, and F.X. Kärtner, High-energy, phase-stable, ultrabroadband kHz OPCPA at 2.1 µm pumped by a picosecond cryogenic Yb:YAG laser, Opt. Express, **19**, 15538–15548 (2011).

[106] C. Homann, M. Bradler, M. Förster, P. Hommelhoff, and E. Riedle, Carrier-envelope phase stable sub-two-cycle pulses tunable around 1.8 µm at 100 kHz, Opt. Lett., **37**, 1673–1675 (2012).

[107] S.W. Huang, J. Moses, and F.X. Kärtner, Broadband noncollinear optical parametric amplification without angularly dispersed idler, Opt. Lett., **37**, 2796–2798 (2012).

[108] A. Renault, D.Z. Kandula, S. Witte, A.L. Wolf, R.Th. Zinkstok, W. Hogerworst, and K.S.E. Eikema, Phase stability of terawatt-class ultrabroadband parametric amplification, Opt. Lett., **32**, 2263–2265 (2007).

[109] M.J. Weber, Handbook of Optical Materials, CRC Press, Washington (2003).

[110] R.R. Alfano, The Supercontinuum Laser Source, Springer, New York, 2nd edition (2006).

[111] A. Brodeur and S. L. Chin, Ultrafast white-light continuum generation and self-focusing in transparent condensed media, J. Opt. Soc. Am. B, **16**, 637–650 (1999).

[112] C. Nagura, A. Suda, H. Kawano, M. Obara, and K. Midorikawa, Generation and characterization of ultrafst white-light continuum in condensed media, Appl. Opt., **41**, 3735–3742 (2002).

[113] M. Bradler, P. Baum, and E. Riedle, Femtosecond continuum generation in bulk laser host materials with sub-µJ pump pulses, Appl. Phys. B, **97**, 561–574 (2009).

[114] K.D. Moll and A. Gaeta, Role of dispersion in multiple collapse dynamics, Opt. Lett., **29**, 995–997 (2004).

[115] L. Bergé and S. Skupin, Self-channeling of ultrashort laser pulses in materials with anomalous dispersion, Phys. Rev. E, **71**, 065601R (2005).

[116] J. Liu, R. Li, and Z. Xu, Few-cycle spatiotemporal soliton wave excited by filamentation of a femtosecond laser pulse in materials with anomalous dispersion, Phys. Rev. A, **74**, 043801 (2006).

[117] S.E. Schrauth, B. Shim, A.D. Slepkov, L.T. Vuong, A.L. Gaeta, N. Gavish, and G. Fibich, Pulse splitting in the anomalous group-velocity-dispersion regime, Opt. Express, **19**, 9309–9314 (2011).

[118] M. Durand, A. Jarnac, A. Houard, Y. Liu, S. Grabielle, N. Forget, A. Durécu, A. Couairon, and A. Mysyrowicz, Self-guided propagation of ultrashort laser pulses in the anomalous dispersion region of transparent solids: a new regime of filamentation, Phys. Rev. Lett., **110**, 115003 (2013).

[119] M.A. Porras, A. Dubietis, E. Kučinskas, F. Bragheri, V. Degiorgio, A. Couairon, D. Faccio, and P. Di Trapani, From x- to o-shaped spatiotemporal spectra of light filaments in water, Opt. Lett., **30**, 3398–3400 (2005).

[120] M.A. Porras, A. Dubietis, A. Matijosius, R. Piskarskas, F. Bragheri, A. Averchi, and P. Di Trapani, Characterization of conical emission of light filaments in media with anomalous dispersion, J. Opt. Soc. Am. B, **24**, 581–584 (2007).

[121] M. Kolesik, E.M. Wright, and J.V. Moloney, Interpretation of the spectrally resolved far field of femtosecond pulses propagating in bulk nonlinear dispersive media, Opt. Express, **13**, 10729–10741 (2005).

[122] A. Saliminia, S.L. Chin, and R. Vallée, Ultra-broad and coherent white light generation in silica glass by focused femtosecond pulses at 1.5 µm, Opt. Express, **13**, 5731–5738 (2005).

[123] M.L. Naudeau, R.J. Law, T.S. Luk, T.R. Nelson, and S.M. Cameron, Observation of nonlinear optical phenomena in air and fused silica using a 100 GW, 1.54 µm source, Opt. Express, **14**, 6194–6200 (2006).

[124] E.O. Smetanina, V.O. Kompanets, S.V. Chekalin, A.E. Dormidonov, and V.P. Kandidov, Anti-stokes wing of femtosecond laser filament supercontinuum in fused silica, Opt. Lett., **38**, 16–18 (2013).

[125] M. Durand, K. Lim, V. Jukna, E. McKee, M. Baudelet, A. Houard, M. Richardson, A. Mysyrowicz, and A. Couairon, Blueshifted continuum peaks from filamentation in the anomalous dispersion regime, Phys. Rev. A, **87**, 043820 (2013).

[126] F. Silva, D.R. Austin, A. Thai, M. Baudisch, M. Hemmer, D. Faccio, A. Couairon, and J. Biegert, Multi-octave supercontinuum generation from mid-infrared filamentation in a bulk crystal, Nature Commun., **3**, 807 (2012).

[127] M. Kolesik, E.M. Wright, A. Becker, and J.V. Moloney, Simulation of third harmonic and supercontinuum generation for femtosecond pulses in air, Appl. Phys. B, **85**, 531–538 (2006).

[128] M. Kolesik, E.M. Wright, and J.V. Moloney, Supercontinuum and third-harmonic generation accompanying optical filamentation as first order scattering processes, Opt. Lett., **32**, 2816–2818 (2007).

[129] N. Aközbek, A. Iwasaki, A. Becker, M. Scalora, S.L. Chin, and C.M. Bowden, Third-harmonic generation and self-channeling in air using high-power femtosecond laser pulses, Phys. Rev. Lett., **89**, 143901 (2002).

[130] N. Aközbek, A. Becker, M. Scalora, S.L. Chin, and C.M. Bowden, Continuum generation of the third-harmonic pulse generated by an intense femtosecond ir laser pulse in air, Appl. Phys. B, **77**, 177–183 (2003).

[131] F. Théberge, W. Liu, Q. Luo, and S.L. Chin, Ultrabroadband continuum generated in air (down to 230 nm) using ultrashort and intense laser pulses, Appl. Phys. B, **80**, 221–225 (2005).

[132] D. Majus and A. Dubietis, Statistical properties of ultrafast supercontinuum generated by femtosecond gaussian and bessel beams: a comparative study, J. Opt. Soc. Am. B, **30**, 994–999 (2013).

[133] D. Faccio, A. Averchi, A. Couairon, A. Dubietis, R. Piskarskas, A. Matijosius, F. Bragheri, M.A. Porras, A. Piskarskas, and P. Di Trapani, Competition between phase-matching and stationarity in Kerr-driven optical pulse filamentation, Phys. Rev. E, **74**, 047603 (2006).

[134] A.H. Chin, O.G. Calderón, and J. Kono, Extreme midinfrared nonlinear optics in semiconductors, Phys. Rev. Lett., **86**, 3292–3295 (2001).

[135] V. Roppo, M. Centini, C. Sibilia, M. Bertolotti, M. Scalora, N. Akozbek, M. J. Bloemer, C. M. Bowden, J. W. Haus, O. G. Kosareva, and V. P. Kandidov, Role of phase matching in pulsed second-harmonic generation: Walk-off and phase-locked twin pulses in negative-index media, Phys. Rev. A, **76**, 033829 (2007).

[136] G. Valiulis, V. Jukna, O. Jedrkiewicz, M. Clerici, E. Rubino, and P. Di Trapani, Propagation dynamics and x-pulse formation in phase-mismatched second-harmonic generation, Phys. Rev. A, **83**, 043834 (2011).